

CUSTOM LOW-COST FORCE MEASUREMENT METHODS
IN FRICTION STIR WELDING

By

Brian Travis Gibson

Thesis

Submitted to the Faculty of the
Graduate School of Vanderbilt University
in partial fulfillment of the requirements
for the degree of

MASTER OF SCIENCE

in

Mechanical Engineering

May, 2011

Nashville, Tennessee

Approved:

Professor George E. Cook

Professor David R. DeLapp

Professor Alvin M. Strauss

For my parents and my sister.

ACKNOWLEDGEMENTS

I would like to thank Dr. George Cook, Dr. Alvin Strauss, and Dr. David DeLapp for guiding this research and serving on my thesis committee. I would also like to thank the Tennessee Space Grant Consortium for providing funding, without which this research would not have been possible.

I would like to thank my colleagues at the Vanderbilt University Welding Automation Laboratory, especially Chase Cox and Jason Aguilar who worked extensively with me on developing the low-cost, wireless force sensor for Friction Stir Welding. I appreciate the help of Dr. William Longhurst and Jason Mitchell, who provided guidance on the selection and use of sensing and data acquisition equipment. Also, thank you to Dr. Robert Galloway for providing always straightforward and practical advice regarding instrumentation, and thank you to Bob Patchin and John Fellenstein of the Vanderbilt University Physics Machine Shop for quality workmanship and assistance on several design issues.

Finally, I would like to thank my family, especially my parents, Bob and Debbie, and my sister, Robin. You have always provided me with the love and support necessary for success.

TABLE OF CONTENTS

	Page
DEDICATION.....	ii
ACKNOWLEDGEMENTS.....	iii
LIST OF TABLES.....	vi
LIST OF FIGURES.....	vii
Chapter	
I. INTRODUCTION.....	1
Tool Geometry.....	3
Joint Configurations.....	9
Weld Zone Characteristics.....	11
Material Flow.....	12
Process Forces.....	15
Force Measurement Methods.....	20
Force Control.....	25
Weld Seam Tracking.....	27
Automatic Welding Machinery.....	28
II. AXIAL FORCE MEASUREMENT.....	32
Introduction.....	32
Proof of Concept.....	32
Finite Element Analysis.....	36
Implementation and Calibration.....	46
Auto-Zero Process.....	51
Demonstration of Measurement.....	53
III. CUSTOM FORCE TRANSDUCER.....	56
Introduction.....	56
Electronics Design.....	58
Mechanical Design.....	66
Implementation and Calibration.....	75
Demonstration of Measurement.....	87

IV. FUTURE WORK.....	89
Measurement of Traversing and Side Forces.....	89
Temperature Measurement.....	91
V. CONCLUSIONS.....	92
REFERENCES.....	95
APPENDIX.....	99
A. FEA Simulation Images.....	99
B. Raw Data from Axial Force Calibration.....	108
C. XBee Data Sheet.....	109
D. XBee Pin Diagram.....	110
E. XBee Communication Code.....	111
F. Elastic Member Strength Calculations.....	113
G. Force Transducer Design Drawings.....	115
H. Torque Calibration Data.....	120

LIST OF TABLES

	Page
Table 1, Force Measurement Methods.....	21
Table 2, Commercially Available Load Cell Options for FSW.....	22
Table 3, Motors, Controllers, and Sensors on the VUWAL FSW Robot.....	29
Table 4, Axial Proof-of-Concept Data.....	34
Table 5, Loading Scenarios for FEA	42
Table 6, Cost of Axial Force Measurement System	48
Table 7, Results of Auto-Zero Test.....	53
Table 8, Elastic Member Design Loads	67
Table 9, Cost of Custom Force Transducer	86

LIST OF FIGURES

	Page
Figure 1, FSW Process (Mishra et al., 2005).....	2
Figure 2, Diagram of Threadgill (2007) FSW Tool Terms	5
Figure 3, FSW Tool Geometry (Mishra et al., 2005).....	6
Figure 4, Flared-Triflute™ Tool Options. A) Neutral Flutes, b) Left-Hand Flutes, c) Right-Hand Flutes, d) Neutral, Right-Handed, or Left-Handed Threads (Thomas et al., 2003)	7
Figure 5, Skew-Stir™ Tool Design by TWI (Thomas et al., 2003)	8
Figure 6, Probe Designs Tested by Elangovan and Balasubramanian (2008).....	9
Figure 7, A Variety of FSW Joint Configurations. (a) Butt Weld, (b) Corner Weld, (c) Double T-Joint, (d) Lap Weld, (e) Multiple Plate Lap Weld, (f) T-Joint, (g) Fillet Weld (Mishra et al., 2005).....	10
Figure 8, Weld Zone Characteristics. A) Parent Material. B) Heat Affected Zone. C) Thermo-Mechanically Affected Zone. D) Nugget. The left side of the weld is the advancing side. (Nandan et al., 2008).....	11
Figure 9, Plot of Velocity Magnitudes Created by a Shoulderless, Conical Tool (Lammlein et al., 2009).....	13
Figure 10, Visualization of Material Flow Around a Tool (Zhao et al., 2006)	14
Figure 11, Force Trends Documented by Cook et al. (2002)	16
Figure 12, Total Loads on a FSW Tool (Hosein et al., 2009)	18
Figure 13, Rotating Plug Model Flows (Nunes et al., 2000)	19

Figure 14, Custom Experimental Force Data Acquisition Setup (Mitchell, 2002)	23
Figure 15, Custom Multi-Axial Transducer for FSW (Blignault et al., 2008)	24
Figure 16, Force and Tool Position Data for a Force Controlled Weld (Longhurst et al., 2010)	26
Figure 17, Demonstration of Tracking a Blind T-Joint (Fleming et al., 2009).....	27
Figure 18, VUWAL FSW Robot	28
Figure 19, Automatic Welding GUI	30
Figure 20, Axial Proof-of-Concept Experimental Setup	33
Figure 21, Strain Gage Response in Proof-of-Concept Experiment.....	35
Figure 22, Screenshot of Milling Machine Head CADD Model	37
Figure 23, Screenshot of CADD Model with Visible Inner Structure.....	38
Figure 24, Mesh for Finite Element Analysis	39
Figure 25, Results of Proof-of-Concept Confirmation Simulation.....	40
Figure 26, Directions of Force Loading for FEA	42
Figure 27, FEA Results for Simulation 1.....	43
Figure 28, FEA Results for Simulation 6.....	43
Figure 29, FEA Results for Simulation 2.....	44
Figure 30, FEA Results for Simulation 10.....	45
Figure 31, Axial Force Data Acquisition Circuit.....	46
Figure 32, Axial Load Calibration	49
Figure 33, Axial Force Measurement Test Results.....	54
Figure 34, Force Transducer Concept.....	57
Figure 35, Universal Wireless RS232 to USB Transceiver (Universal, 2010).....	59

Figure 36, MicroStrain SG-Link Wireless Strain Node (SG-Link, 2010).....	59
Figure 37, XBee Modules (Xbee, 2008).....	60
Figure 38, XBee Adapter Board (Tweet, 2010).....	62
Figure 39, XBee Receiver with USB Connector	62
Figure 40, ProLite V2 Battery and Thunder Power Charger	64
Figure 41, Wireless Force Transducer Circuit Diagram.....	65
Figure 42, Elastic Element Cross Sections	68
Figure 43, Screenshot of Force Transducer Model.....	70
Figure 44, Screenshot of Force Transducer Model.....	71
Figure 45, Interior View of Electronics Box Model.....	73
Figure 46, Electronics Box Model with Lid	74
Figure 47, Elastic Element and Taper.....	75
Figure 48, Heat Sink and Thermal Barrier.....	76
Figure 49, Electronics Box after Prototyping	77
Figure 50, Temperature Measurement Region	78
Figure 51, Temperature Data for Heat Sink Test.....	78
Figure 52, Installation of Electronics.....	80
Figure 53, Force Transducer Balancing Process.....	81
Figure 54, Force Transducer Balancing Process.....	81
Figure 55, Custom Force Transducer for FSW.....	82
Figure 56, Custom Force Transducer for FSW.....	83
Figure 57, Torque Wrench and Adapter Tool.....	84
Figure 58, Torque Calibration Curve.....	85

Figure 59, Torque Measurement Test Weld	88
Figure 60, Encoder Setup for Resolving X and Y Forces.....	90
Figure 61, Nonlinear Crosstalk Relationships (Blignault et al., 2008).....	91

CHAPTER I

INTRODUCTION

Friction stir welding (FSW) was invented in 1991 at The Welding Institute (TWI) of Cambridge, England (Thomas et al., 1991). FSW is a solid-state joining technique that has grown rapidly in popularity in a wide variety of industries including the aerospace, railway, land transportation, and marine industries (Cook et al., 2004). Most often used on low melting point alloys such as aluminum, FSW has many advantages over fusion welding techniques. Because process temperatures remain below the melting point of the welded material, low distortion and low residual stresses are inherent to the process, and there is no need for either shielding gas or filler material. FSW is also an energy efficient process that produces no fumes, arc flash, or spatter (Cook et al., 2004). Perhaps the most significant advantage of FSW however, is that the technique allows for the joining of dissimilar materials or materials that are difficult or nearly impossible to fusion weld.

The FSW process includes three phenomena: heating, plastic deformation, and forging (Longhurst, 2009). A non-consumable rotating tool, consisting of a probe and shoulder, is plunged into the materials to be joined and then traverses the joint line. Heat is generated through both friction and plastic deformation of the welded material. At elevated temperatures, the material plasticizes and is sheared at the front of the probe and it is rotated to the rear of the probe where it is forged together under significant shoulder pressure. The FSW process is illustrated in Figure 1.

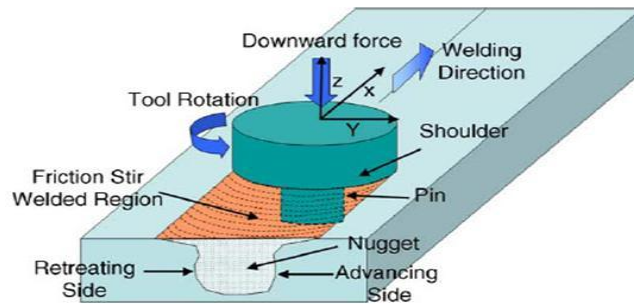


Figure 1, FSW Process (Mishra et al., 2005)

Figure 1 displays the advancing and retreating sides of a FSW weld. The advancing side is the region in which the traverse velocity and the tangential velocity of the rotating tool are in the same direction. The retreating side is the region in which the traverse velocity and the tangential velocity of the rotating tool are in opposite directions. This advancing or retreating phenomenon leads to different mixing characteristics within the weld seam, depending on location. These characteristics will be discussed further in the material flow section of the introduction. FSW can be performed on a variety of joint configurations, including butt joints, lap joints, and T-joints (Mishra et al., 2005).

Because FSW is still a relatively new joining technique, there are numerous research opportunities associated with the process, including improving tool design, optimizing weld parameters for particular materials and joint configurations, testing new joint configurations, reducing tool wear, welding dissimilar materials, developing process force measurement techniques, implementing force and/or torque control, simulating particular welding or weld control scenarios, and modeling material flows using computational fluid dynamics (CFD). The research presented in this thesis focuses on developing a low-cost method of force and torque measurement for FSW. The methods

presented here are viable alternatives to using high cost options, such as a Kistler™ rotating cutting force dynamometer or a LOWSTIR™ friction stir welding system. Developing a custom force measurement system, as was done in this research, also allows for custom control schemes to be implemented with relative ease. This research presents the methods used to develop a custom, low-cost force measurement system for FSW as well as demonstrates the abilities of the system to work in conjunction with custom weld controller software and process planning schemes, such as autozero.

Tool Geometry

The defining terms for FSW tools and tool geometry have been outlined in a paper by Threadgill (2007). The “tool” as defined in this paper is the rotating component that contacts the welded material and generates heat. This is an intentionally broad definition, yet it is specifically meant to exclude cases where the shoulder is stationary, and therefore does not generate heat. The tool is comprised of two main components. The “probe” is defined by Threadgill (2007) as the part of the tool that is totally plunged below the material surface during welding. Term “pin” may also be used in place of probe. The “shoulder” is defined as the part of the tool that remains on the surface or slightly plunged into the surface and is used to create forging pressure. The basic concept that will always characterize tool design is that the probe is of smaller diameter than the shoulder.

Also, the probe is usually slightly shorter than the thickness of the welded material in the case of a butt weld. The distance between the bottom of the probe and the

bottom of the welded material is often referred to as the “weld ligament”. The weld ligament may typically be on the order of 0.003 inches to 0.008 inches. Despite this dimensional difference, material is forced downward against the anvil, and a full-penetration weld is created in most cases.

Threadgill (2007) also defined the front and rear regions of the tool as the “leading face” and the “trailing face” respectively. The common term “edge” was not used because often the shoulder of the tool is slightly plunged into the welded material, meaning there is no clearly defined edge. Often FSW tools are tilted in the direction of traverse in order to enhance the material containment ability of the tool. When a tool is tilted, the characterizing angle is referred to as the “tilt angle”. The angle can also be called the “travel angle”, which is commonly used by the American Welding Society (AWS). A tilted tool results in the trailing face of the shoulder being plunged deeper than the leading face of the shoulder. Threadgill (2007) referred to the region of the shoulder that is plunged the deepest as the “heel”. The “heel plunge depth” is the maximum depth that the shoulder reaches into the welded material. If the tool is tilted sideways, the characterizing angle is referred to as the “sideways tilt angle” or the “work angle”, which is commonly used by AWS. Figure 2 displays a diagram of some of these FSW tool terms.

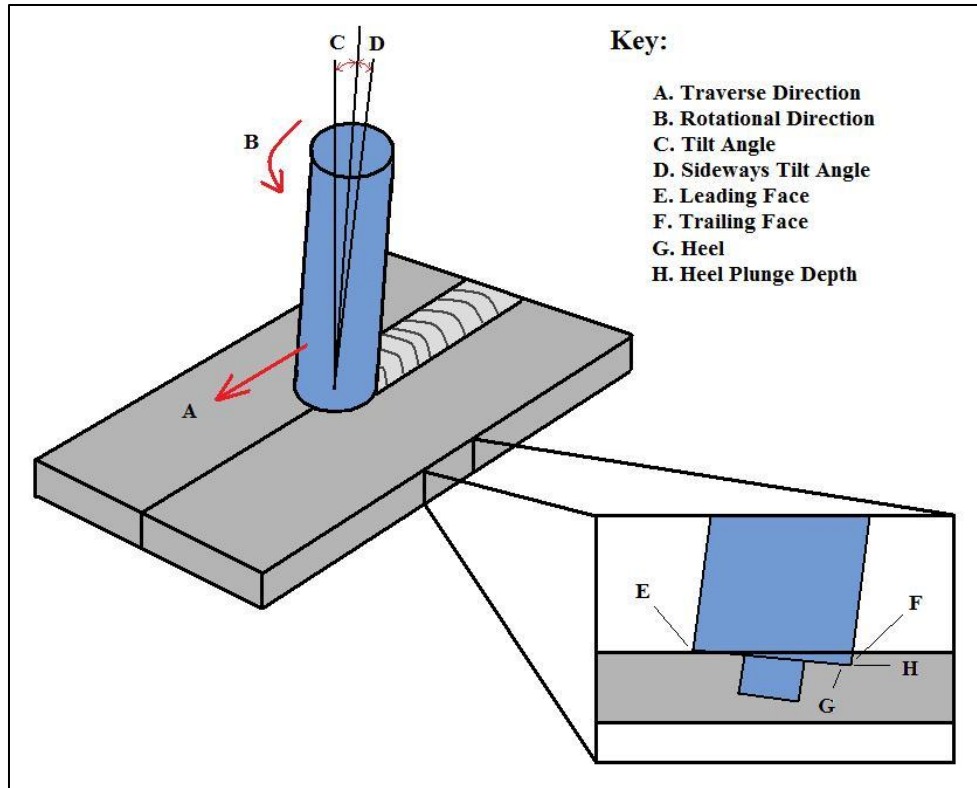


Figure 2, Diagram of Threadgill (2007) FSW Tool Terms

Tools are mostly commonly cylindrical in nature and may exhibit many features, such as threads, scrolls, flutes, and flats (Threadgill 2007). Scrolls are often used on the shoulder of the tool to facilitate material containment. Without scrolls, often material can escape from the high pressures of the shoulder, resulting in weld flash. Flash represents lost material that could have contributed to weld strength. It would be common for voids or other weld defects to accompany welds that have excessive flash. Threads and flutes are used on the tool probe to increase mixing within the weld seam. Threads create vertical flows that can help to eliminate oxide layers that exist on the outside of welded materials. Often tool designs are optimized to maximize material flow and maximize the

interruption of oxide layers at the material interface (Thomas et al., 2003). Figure 3 shows a diagram of the threads, flutes, and scrolls that may be used on a FSW tool.

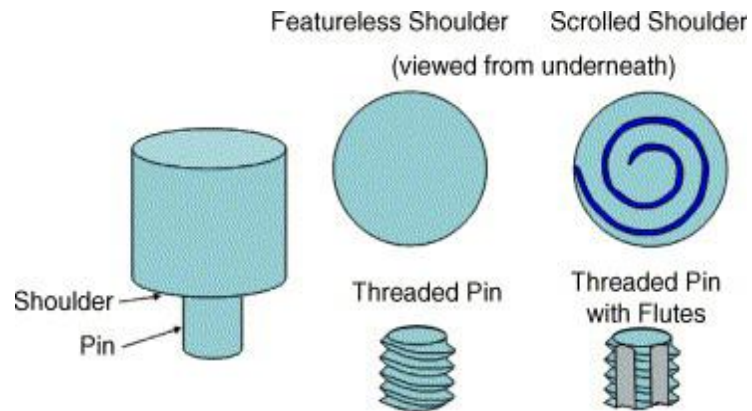


Figure 3, FSW Tool Geometry (Mishra et al., 2005)

Although simple cylindrical tools are most common, modifications to both the shoulder and the probe have been extensively studied to determine the effects on weld quality. Many of the most innovative tool designs have been developed by TWI. Several new tool designs were presented in a paper by Thomas et al. (2003). Two of the designs that were central to this paper were the Flared-Triflute™ design and the Skew-Stir™ design (Thomas et al., 2003). These tools were developed specifically for lap welds. Thomas et al. (2003) found that one of the most common problems in lab welds was differential pressure between the top and bottom sheets. Differential pressure can lead to a thinning of the top sheet and a thickening of the bottom sheet, which leads to a weaker weld that may simply peel apart under certain loading conditions. These new tool designs facilitate even mixing between layers. Figure 4 displays the options of the Flared-Triflute™ design.

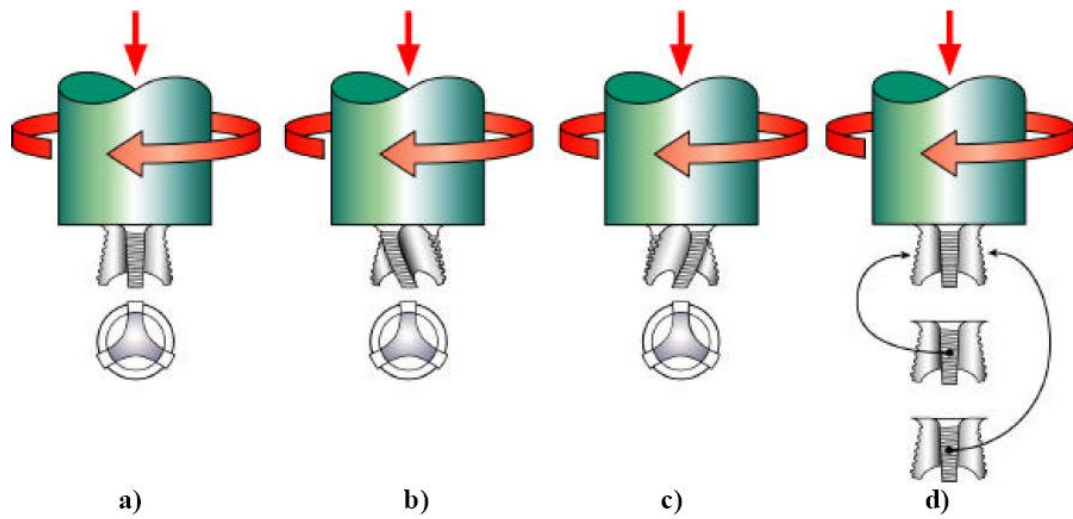


Figure 4, Flared-Triflute™ Tool Options. A) Neutral Flutes, b) Left-Hand Flutes, c) Right-Hand Flutes, d) Neutral, Right-Handed, or Left-Handed Threads (Thomas et al., 2003)

As displayed in Figure 4, the flutes and threads of the Flared-Triflute™ tool can be treated as independent tool features, and can therefore be customized to match the needs of a specific application perfectly (Thomas et al., 2003). Thomas et al. (2003) demonstrated that lap welds performed with the Flared-Triflute™ tool exhibited very little thinning of the top sheet and had a much greater weld width than welds performed with a conventional cylindrical probe. Perhaps one of the most innovative FSW tools designs ever proposed is the Skew-Stir™ tool by TWI. The concept for this tool may be seen in Figure 5.

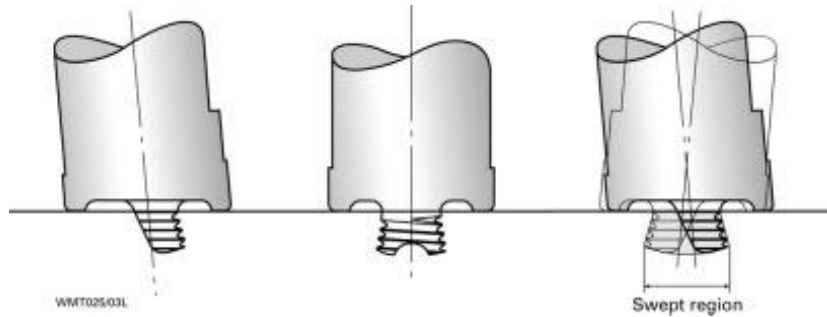


Figure 5, Skew-Stir™ Tool Design by TWI (Thomas et al., 2003)

The purpose of the Skew-Stir™ tool is to generate a swept volume that is much larger than the volume of the probe itself. The name “skew” comes from the fact that the axis of the tool and the axis of rotation are askew. Sometimes the ratio of the swept volume of the probe to the actual volume of the probe is referred to as “dynamic volume”. Figure 5 displays the swept region created when the tool is rotated. Thomas et al. (2003) demonstrated that welds performed with the Skew-Stir™ tool exhibited less pronounced edge notch defects at the outer reaches of the weld zone. These types of defects will be discussed further in following sections.

Studies have also been conducted that compare the characteristics of welds performed with different variations of relatively simple tool geometry. Elangovan and Balasubramanian (2008) studied the effects of different probe geometry on the formation of the friction stir processing (FSP) zone in AA2219 aluminum alloy welds. They tested tools with a straight cylindrical probe, a tapered cylindrical probe, a threaded cylindrical probe, a triangular probe, and a square probe. Figure 6 displays these tools.

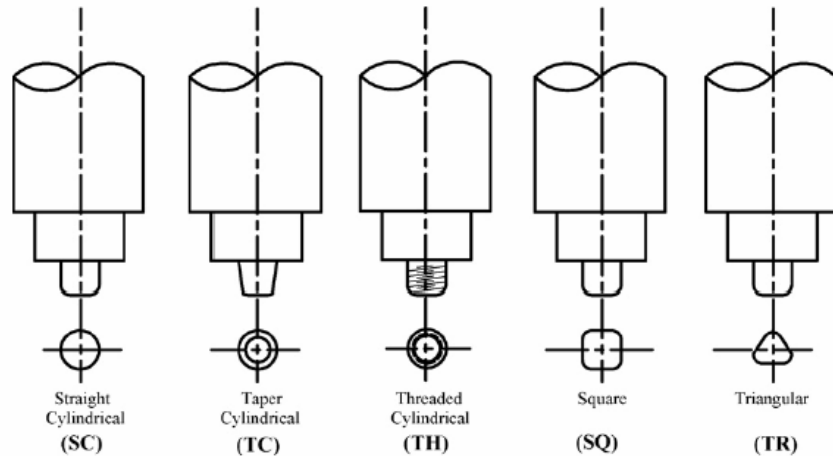


Figure 6, Probe Designs Tested by Elangovan and Balasubramanian (2008)

Elangovan and Balasubramanian (2008) tested each tool design at three different traverse speeds and then analyzed the welds for quality and strength. They found that the square probe tool produced defect free FSP regions at all traverse speeds. They also found that the weld with the highest tensile strength was produced by the square probe tool at a traverse rate of 0.76 mm/s. This study shows that unconventional tool designs may in fact hold promise for creating higher quality welds than those produced with conventional threaded cylindrical probe tools. The dynamic volume of the square probe likely facilitated extra mixing which led to increased weld quality.

Joint Configurations

FSW can be performed in a variety of joint configurations, the most common of which are butt welds, lap welds, T-joints, and pipe welds. With each joint configuration, there are many choices the FS welder must make regarding tool geometry and fixturing.

Often the most challenging aspect of performing a friction stir weld in a particular joint configuration is designing and building the proper clamps to hold the workpiece rigidly throughout the process. In most cases, a flat, rigid anvil must be located beneath the welded material to bear the load of the large axial force. Figure 7 displays a variety of joints that can be friction stir welded.

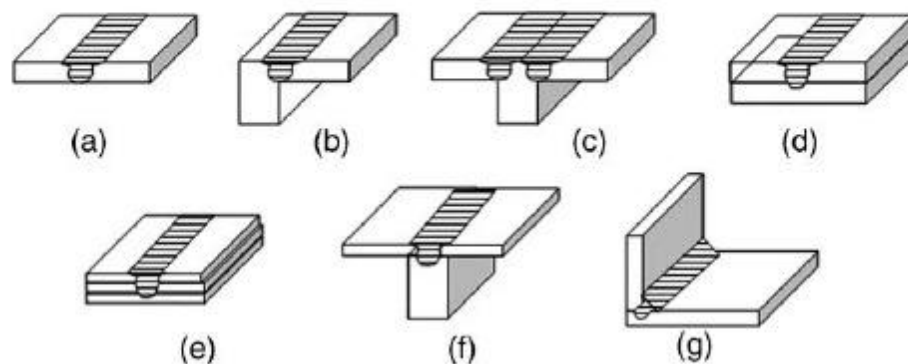


Figure 7, A Variety of FSW Joint Configurations. (a) Butt Weld, (b) Corner Weld, (c) Double T-Joint, (d) Lap Weld, (e) Multiple Plate Lap Weld, (f) T-Joint, (g) Fillet Weld (Mishra et al., 2005)

Not displayed in Figure 7 are pipe welds and hemispherical welds. These types of welds have many industrial applications, but also require custom machinery in most cases. In all cases, however, friction stir welds are performed by industrial robots or automated machines specifically designed and built for FSW. Work pieces are clamped to rigid anvils and the machinery operates under welding parameters that are set by the user before the start of the weld in order to follow the joint line. More information about FSW machines and their load requirements will be presented in following sections.

Weld Zone Characteristics

In order to study FSW, it is extremely important for researchers to have standards for characterizing the weld zone. In his terminology paper, Threadgill (2007) defined the advancing and retreating sides of the weld, which have already been covered to some extent, but he also defined the micro-structural classification for the cross-section of a friction stir welded joint. Figure 8 displays the basic regions used to classify the weld zone.

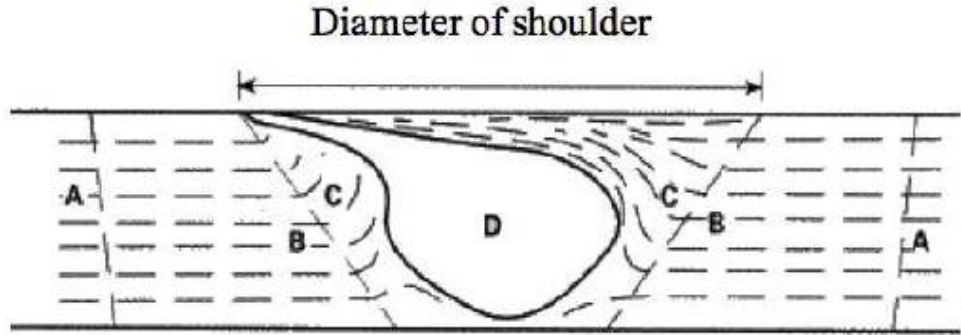


Figure 8, Weld Zone Characteristics. A) Parent Material. B) Heat Affected Zone. C) Thermo-Mechanically Affected Zone. D) Nugget. The left side of the weld is the advancing side. (Nandan et al., 2008)

The geometry in Figure 8 corresponds to either a butt weld or a bead-on-plate weld. The parent material region is far enough from the joint line that it is not affected by heat. The heat affected zone (HAZ) lies just outside the joint line and is not affected by plastic deformation on the macro scale, although Threadgill (2007) asserts that there may very well be deformation on a micro scale that would not be visible upon basic inspection. The thermo-mechanically affected zone (TMAZ) is affected by both heat and plastic deformation caused by stirring. The shape of the TMAZ can vary depending on the

welded material, tool design, and the welding parameters, but usually at a minimum encompasses the trapezoidal area defined by the tool shoulder diameter and the diameter of the bottom of the probe. Material within the TMAZ may or may not be recrystallized. Material that is recrystallized is contained within the weld nugget. The size of the nugget at a minimum corresponds to the area through which the probe passes as it traverses through the material. Threadgill (2007) admits that the term nugget “lacks scientific pedigree” and the dynamics of recrystallization in FSW are hardly agreed upon by researchers in the field, but that does not affect the classification of these different weld zone regions. Other names for the nugget that are sometimes used are the “dynamically recrystallized zone” although this is unnecessarily wordy, or the “stirred zone” which is not completely accurate because the TMAZ also includes stirred material (Threadgill, 2007). Many studies have been performed to study material flow and modes of recrystallization in FSW, and these will be discussed further in the following section.

Material Flow

Material flow in FSW is affected by both the geometry of the probe and the shoulder. Sufficient material flows within the weld seam are necessary to create strong, defect-free welds. Insufficient flows may result in defects known as “volumetric flaws” or “voids” and can range from large surface features that are easily visible to much smaller voids within the joint that can be detected only with the use of microscopic or metallographic techniques (Threadgill, 2007). There are many different methods used to both predict and measure the material flows created by different tool geometries. One of the most

common methods used by researchers to predict the performance of new tool designs in a time efficient and low cost manner is with computational fluid dynamics or CFD. Lammlein et al. (2009) used Ansys FLUENT to model the effectiveness of a new shoulderless, conical tool design. With this analysis, in conjunction with experimental results, it was determined that this new tool design produced acceptable welds when used in an AL butt weld configuration. Figure 9 displays a plot of velocity magnitude around the surface of the conical tool from Lammlein's study.

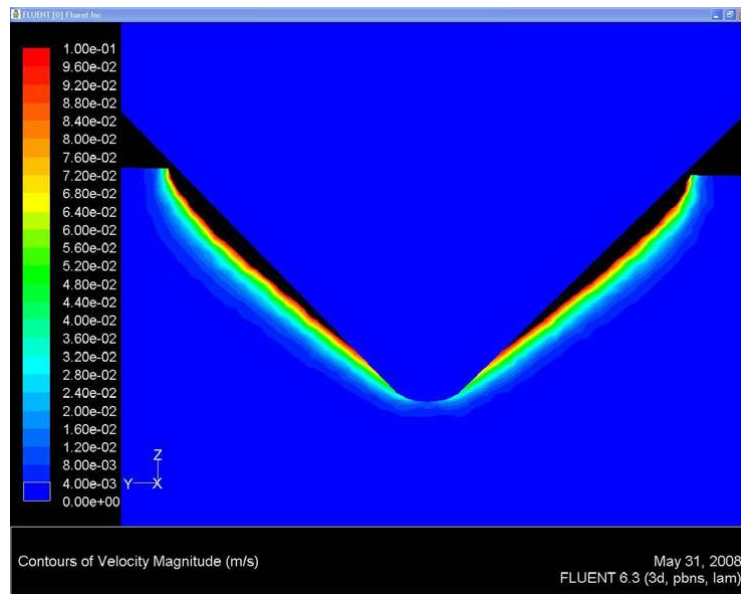


Figure 9, Plot of Velocity Magnitudes Created by a Shoulderless, Conical Tool (Lammlein et al., 2009)

Lammlein also used CFD analysis in other studies to determine material flow velocities and temperatures in the welds of small diameter pipes and hemispheres (Lammlein, 2010).

A variety of experimental methods are used to analyze the effectiveness of tools when it comes to creating adequate material flows. Zhao et al. (2006) used a LF5 Al

alloy marker in Al 2014 alloy welds to visualize material flows with three different FSW tool geometries: a cylindrical probe, a tapered probe, and a tapered probe with threads. Welds were imaged digitally and the pixel positions of individual markers were compiled to create three-dimensional plots of material flow around the tool. Figure 10 displays one of these plots.

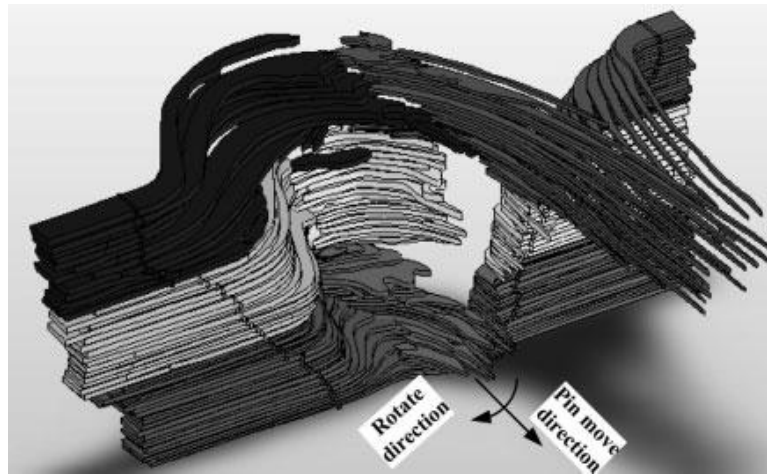


Figure 10, Visualization of Material Flow Around a Tool (Zhao et al., 2006)

The results helped to quantify the difference in material flows between threaded and non-threaded probe geometry, and it was confirmed that there are asymmetrical flows deriving from the advancing/retreating phenomenon inherent in FSW.

Scialpi et al. (2007) also studied the effects of tool geometry on material flow, but with a focus specifically on shoulder geometry and the resulting microstructure and mechanical properties of friction stir welded thin-sheet Al 6082. Tensile tests, hardness tests, and metallographic analysis showed that a shoulder with rounded edges and a

cavity in its surface produced better overall results than a shoulder with just a rounded edge or a shoulder with a rounded edge and a scroll.

Some studies of material flow have shown that there exists a strong relationship between material flow and process forces. Schneider et al. (2006) used lead tracer wires to study how the FSW tool relocated material in 2195-T81 Al-Li-Cu butt welds. X-ray radiography was used to image the welds, and distributions of material at periods consistent with tool rotation speed were seen. However, a distribution with an irregular period much longer was also seen. It was proposed that the irregular period resulted from a slip-stick mechanism between the tool shoulder and welded material that could arise from insufficient plunge force.

Nunes et al. (2000) has also proposed a material flow model that lends itself in an even more direct manner for explaining and predicting process forces. The Nunes model will be discussed in detail in the follow section.

Process Forces

Modeling, measuring, and controlling FSW process forces is important for a wide variety of reasons. Force signals give researchers additional process data from which to derive information about weld quality, resulting mechanical properties, and even tool wear. Force control allows for a wide range of possibilities, from controlling weld characteristics to allowing FSW to be performed on industrial robots which may have limited load capacities. There are four main forces that are of interest in FSW. These are the axial force (F_z), the traversing force (F_x), the side force (F_y), and the torque (M_z or T).

Refer to Figure 1 to see the directions of the axes relative to the welding direction. The magnitude of these forces depends greatly on many factors including the material to be welded, the joint configuration, the tool design, and the welding parameters.

A significant amount of basic research has gone into determining the relationships between welding parameters and process forces and determining trends in this data that could be exploited for control purposes. Cook et al. (2002) conducted experiments consisting of a matrix of bead-on-plate 6060-T651, ¼” thick welds at a range of rotation rates and traverse rates while measuring process forces with a Kistler Model 9124B rotating cutting force dynamometer. It was determined that lower traverse rates and higher tool rotation rates induce decreased axial forces. In some cases, axial force was decreased by nearly 50% by varying the tool rotation rate or the traverse rate. See Figure 11 below for the trends detected in this study.

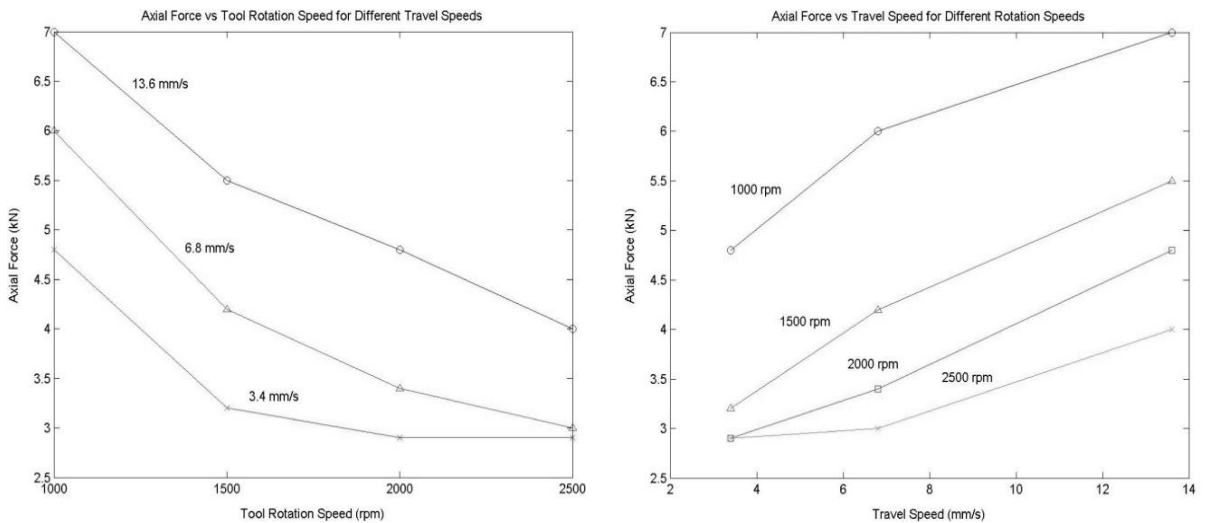


Figure 11, Force Trends Documented by Cook et al. (2002)

This was key information for allowing FSW to be performed with standard industrial robots. Also note the magnitude of the axial force in Figure 11, which would be typical for most ¼” thick aluminum butt welds.

Crawford et al. (2006a) took the work of Cook et al. (2002) and extended it to determine the range for which the parameter/force trends existed. They did so with the assumption that as the weld pitch continued to increase, forces would continue to drop. Weld pitch is the tool rotation rate divided by the traverse rate, meaning a high weld pitch would involve combinations of relatively high rotation rates and relatively low traverse rates. Crawford et al. found that the trends observed by Cook et al. (2002) existed for tool rotation rates from 1500 to 4500 rpm and for traverse rates from 11 ipm to 63 ipm. These were the parametric bounds for the experiment. Therefore, the upper bound of these trends may not have been reached. This was confirmed with a theoretical modeling exercise in which Crawford et al. conducted simulations of the welding process in order to compare model predictions to experimental results. Both Couette and viscoplastic models were implemented in a three dimensional CFD FLUENT simulation to confirm the experimental findings.

Computer modeling is, in fact, often used to provide a baseline or point of comparison for the experimental measurement of forces in FSW. Crawford et al. (2006b) once again found strong correlation between forces measured in welding to those predicted by two different models that were implemented in FLUENT. Ulysse (2002) used a numerical visco-plastic model to predict force trends as well as temperatures related to process parameters, with a focus on aluminum welds in a butt joint configuration. Hosein et al. (2009) conducted a comprehensive modeling study of the

forces that a threaded FSW tool experiences while welding ¼” AA6061-T6. They accounted for temperature depended material properties as well as the slip-stick mechanism that was previously discussed. Figure 12 displays selected 3D plots of the numerical simulation results.

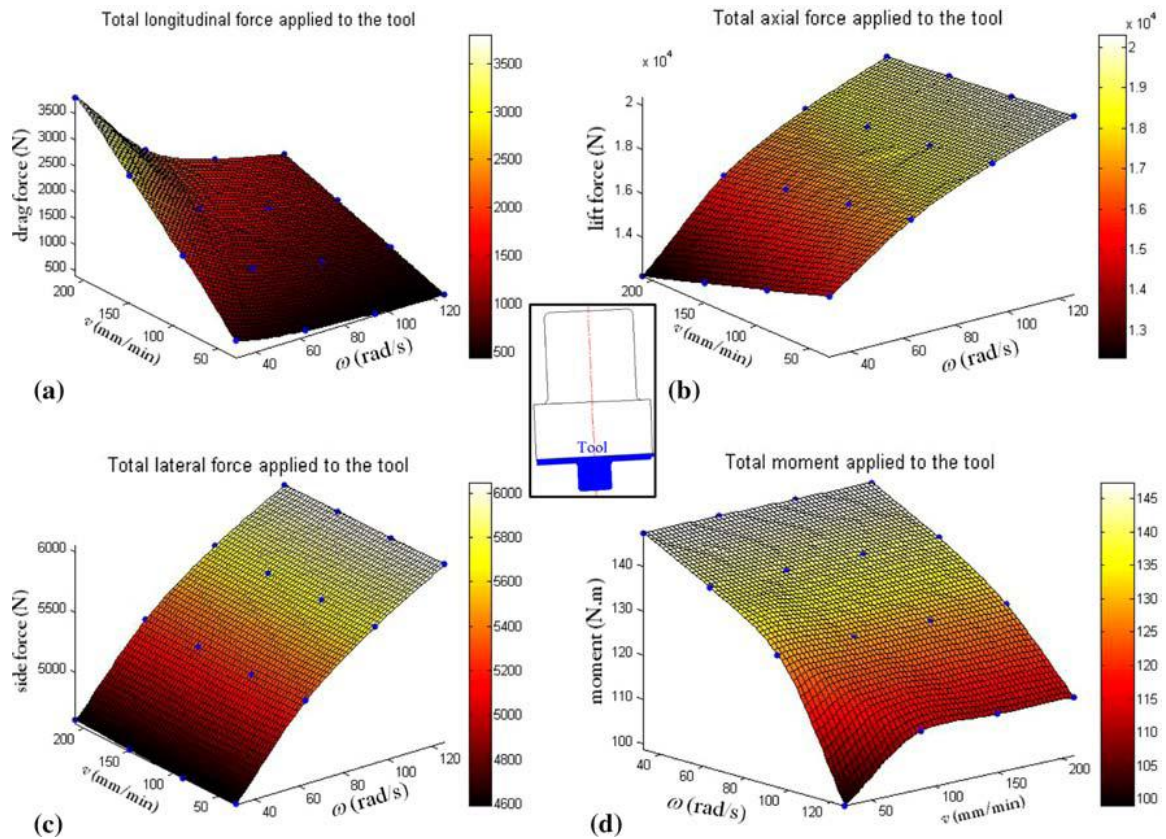


Figure 12, Total Loads on a FSW Tool (Hosein et al., 2009)

It is also noteworthy that Hosein et al. (2009) attributed the side or lateral force (F_y) to the Magnus effect, which arises from the rotating probe traversing through the plasticized metal.

While computer simulations can be useful and can be customized to specifically match experimental procedures, there are other models that are broader and generally

simpler in nature that can lend quite a bit of insight into the FSW process. As previously mentioned Nunes et al. (2000) proposed a material flow model for FSW and developed relatively straightforward mathematical models for the forces experienced by a FSW tool. This “Rotating Plug Model” hypothesizes that a thin layer of welded material sticks to and rotates with the tool probe. Outside of this layer, there is a shear zone that separates the plug from stationary material. There can also be secondary vertical flows created by threads on the probe. As the tool translates along the weld joint, the plug transfers material in a periodic shearing action from the front to the back of the probe. Figure 13 displays the material flows that are associated with this model.

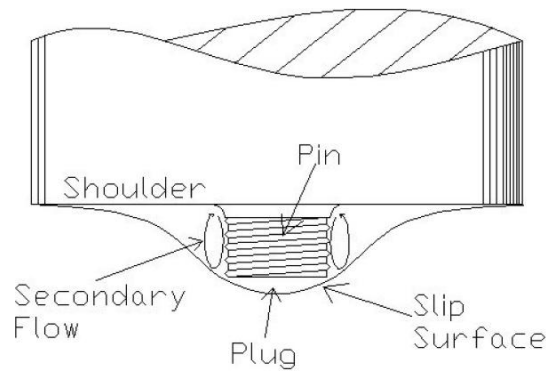


Figure 13, Rotating Plug Model Flows (Nunes et al., 2000)

With this model, Nunes et al. (2000) assert that forces in FSW arise from the interactions between the rotating plug and the surrounding material. If the secondary flows are ignored, the torque on the FSW tool is given by:

$$T_{total} = T_{pin\ bottom} + T_{pin\ sides} + T_{shoulder}$$

$$T_{total} = \int_0^r 2\pi r^2 \sigma dr + 2\pi r^2 t \sigma + \int_r^R 2\pi r^2 \sigma dr$$

$$T_{total} = \frac{2\pi R^3}{3} \left(1 + 3 \frac{r^2 t}{R^3}\right) \sigma$$

In this equation, R represents the shoulder radius, r represents the probe radius, t is the probe length, and σ is the shear flow stress. Nunes et al. (2000) also developed approximate expressions for the shear flow stress and the temperature at the shear zone and altered constants within them to match experimental results. Additionally, the interaction of the shoulder and the workpiece was examined by comparing the axial force during welding to the force required to push an indenter into a metal surface. The indentation force is given by:

$$F_I = 6\pi R^2 \tau$$

The slip-stick condition can be determined with this comparison which is important when it comes to predicting torque using the Rotating Plug Model which assumes total shoulder contact (Nunes et al., 2000). This model has a simple form which makes it very convenient for back-of-the-envelope type of calculations; however, the simplicity also may lend itself to error and underscores the importance of measuring the actual forces that are present in the FSW process.

Force Measurement Methods

Force measurement is an issue that is not only important in FSW but can be encountered across nearly all engineering disciplines, from civil engineering to biomedical engineering to manufacturing. Deyuan et al. (1995) used force feedback signals to determine not only when a tool breakage had occurred in a milling operation,

but were also able to determine the severity of the breakage as well. In the industrial applications of FSW, force measurement gives engineers and operators additional data that relates to weld quality and resulting mechanical properties. Having a feedback force signal also allows certain control schemes to be implemented that may greatly improve the FSW process.

In general, there are a few proven and common methods engineers use to measure force. Table 1 summarizes these methods and lists some of the advantages and disadvantages associated with them.

Table 1, Force Measurement Methods

Force Sensor	Principle	Advantages	Disadvantages
Spring	Hooke's Law	Simple Rugged Good for static loads	Slow Must also measure position
Piezoelectric Crystals	Piezoelectric effect	Fast Unpowered	Bad for static loads Fragile
Strain Gages	Resistance change	Cheap Available Easy to work with	Highly temperature sensitive

Spring based force measurements are simple, but also require a measurement of position or capacitance to determine the amount of deflection. These types of sensors are usually not appropriate for real-time measurements in industrial manufacturing applications; however, there are some capacitive loads cells that are gaining popularity. Most industrial load cells use either strain gages or piezoelectric crystals as the sensing

element. When the Vanderbilt University Welding Automation Lab (VUWAL) began searching for a new force measurement method after discontinuing the use of a Kistler 9123CQ01 rotating cutting-force dynamometer, several options were sought. Table 2 below displays all of the load cells that were considered.

Table 2, Commercially Available Load Cell Options for FSW

Transducer	Image	Model	Sensors	Force – Capacity	Cost, \$
FUTEK Button Load Cell		LLB450	Metal foil strain gages	Fz – 13,300 N (3,000 lb)	450.00
SensorData Torque Sensing Pulley		T211	Strain gages	Mz – 225 N-m (165 ft-lb)	5,000.00
FUTEK Multi Axis Load Cell		MTA600	Metal foil strain gages	Fx – 11,120 N (2,500 lb) Fy – 11,120 N (2,500 lb) Fz – 22,240 N (5,000 lb)	6,000.00
ATI Multi Axis Load Cell		Omega 160	Silicon strain gages	Fx – 2,500 N (560 lb) Fy – 2,500 N (560 lb) Fz – 6,250 N (1,400 lb) Mz – 400 N-m (295 ft-lb)	8,172.00
ATI Multi Axis Load Cell		Omega 190	Silicon strain gages	Fx – 7,200 N (1,620 lb) Fy – 7,200 N (1,620 lb) Fz – 18,000 N (4,050 lb) Mz – 1400 N-m (1,030 ft-lb)	11,997.00
LowStir Welding System		LowStir Mk.2	Strain gages	Fxy – 25,000 N (5,620 lb) Fz – 50,000 N (11,240 lb) Mz – 100 N-m (75 ft-lb)	24,000.00
Kistler Table Dynamometer		9257BA	Piezoelectric crystals	Fx – 5,000 N (1,120 lb) Fy – 5,000 N (1,120 lb) Fz – 5,000 N (1,120 lb)	24,573.50
Kistler Table Dynamometer		9255B	Piezoelectric crystals	Fx – 40,000 N (9,000 lb) Fy – 40,000 N (9,000 lb) Fz – 40,000 N (9,000 lb)	39,415.60
*All information was obtained from the manufacturers' websites and/or requested quotations.					

Note that all of the load cell options use either strain gages or piezoelectric crystals as the sensing element. Also note that some of the load cells considered measure force in only one direction. Combinations of these load cells would have to be used in order to obtain all forces. The LowStir system is unique in that it is designed to be utilized specifically in FSW research or industrial applications (Johnson, 2010). It is also marketed as a low-cost force and temperature measurement alternative; however, as can be seen in Table 2, it is closer in cost to some of the ‘higher-end’ Kistler dynamometers. Because of the high costs associated with some of these load cells, often researchers seek to build low-cost, custom alternatives that may be very application specific.

Mitchell (2002) instrumented a FSW tool with strain gages to measure F_x , F_y , and M_z and used a button load cell above the tool to measure F_z during a single experiment. Figure 14 displays Mitchell’s data acquisition setup.

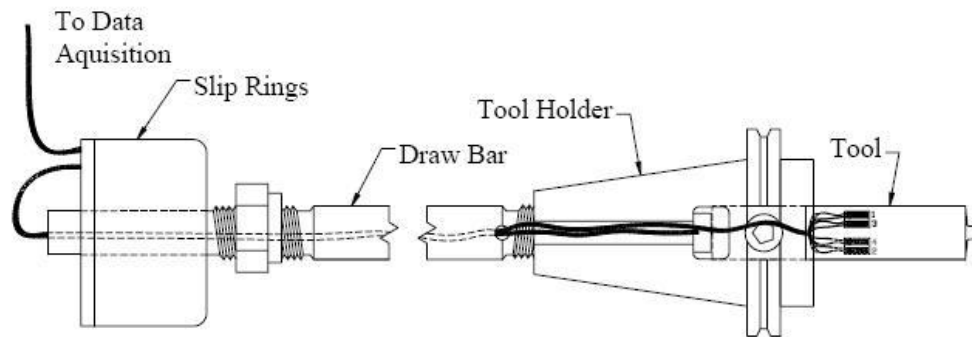


Figure 14, Custom Experimental Force Data Acquisition Setup (Mitchell, 2002)

This is obviously low-cost and effective but would not be practical for continuous use in a research setting or manufacturing operation due to the large number of tools that would have to be instrumented and the extreme heat to which the strain gages are directly subjected.

Taking a different approach to studying forces in FSW, Burton et al. (2009) patented a device that would trace the planned path of a friction stir weld to confirm predicted loads before the weld is performed. A ball rolls along the surface of the material and reacts against a load cell that is mounted on the interior of the device. This would be especially insightful for three-dimensional contour welds.

Perhaps one of the most noteworthy efforts to produce a low-cost custom load cell for friction stir welding was put forth Blignault et al. (2008). Blignault and his colleagues developed a multi-axial transducer capable of measuring all forces of interest in FSW as well as the temperature of the tool and the temperature of the elastic member to which the strain gages were mounted. Figure 15 displays a model of their device.

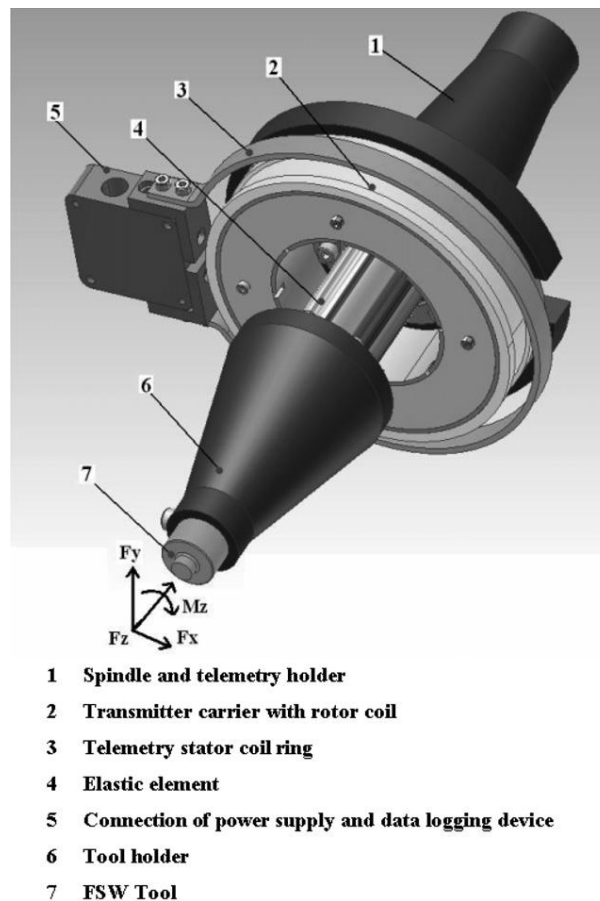


Figure 15, Custom Multi-Axial Transducer for FSW (Blignault et al., 2008)

Power to the strain gages was provided through induction and a custom telemetry system was developed that operated on the principle of capacitive coupling of Frequency Division Multiplexed (FDM) modulated signals (Blignault et al., 2008). More information on this device will be discussed in latter chapters of this thesis, as it served as a prime example of a successful implementation of a low-cost custom alternative.

Once researchers and manufacturers have the capability to measure forces in FSW, they are then able to implement feedback control schemes or through-the-tool tracking techniques that can greatly improve the overall usability of the FSW process.

Force Control

Although the focus of this thesis is force sensing, it is important to briefly cover the capabilities that are unlocked when force measurement is implemented as motivation for the work that will be presented. As already discussed, Cook et al. (2002) documented trends in the relationships between process parameters and process forces that could be exploited for control purposes. Longhurst (2009) examined key enablers for force control of FSW, specifically addressing controller design and tool design in great detail. Additionally, Longhurst et al. (2010a) implemented force control of FSW using a PID controller that was tuned using the Ziegler-Nichols method. Figure 16 displays the axial force data and vertical tool position (plunge) data for a force controlled weld. The results of this work speak volumes about how interrelated process forces, weld quality, and resulting mechanical properties are in FSW. Longhurst et al. (2010a) found that force control via plunge depth (plunge depth is manipulated variable) can compensate for variances in material thickness and robot arm deflection, force control via traverse speed

can control heat distribution along the weld seam, and force control via rotation speed can lead to welds with a higher average tensile strength.

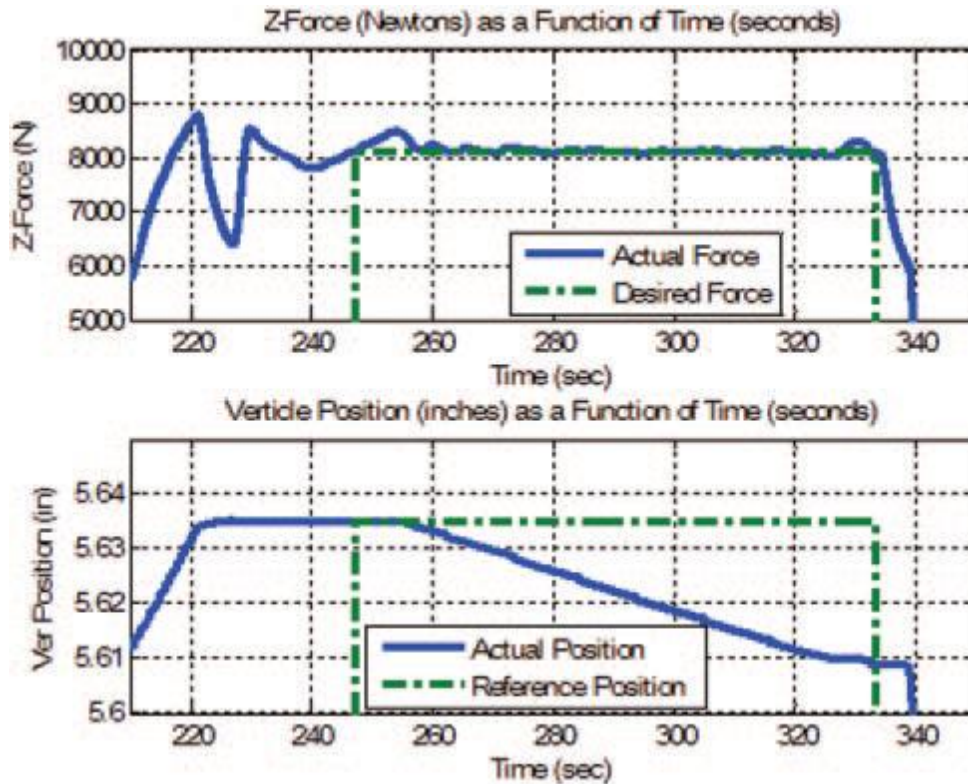


Figure 16, Force and Tool Position Data for a Force Controlled Weld (Longhurst et al., 2010)

Longhurst et al. (2010b) implemented torque control of FSW and found that it was more suitable for maintaining proper tool-workpiece contact, and torque control was also shown to provide a means of controlling weld power.

Many more researchers have documented the use of force control in FSW. Most notably, Smith (2000) demonstrated that utilizing force control allows FSW to be performed successfully using a standard industrial robot. The actuator torques in the ABB IRB 6400 robot were used as a means of measuring the end effector force, and this force was controlled despite the higher requirements in computation time. Outside of

force and torque control, one of the more impressive capabilities that force measurement unlocks is through-the-tool tracking.

Weld Seam Tracking

A through-the-tool tracking system has been developed for FSW that utilizes a force feedback signal to derive information about a tool's path through the workpiece (Fleming et al., 2008a). Fleming et al. (2008b) demonstrated that the axial force signal could be used to detect joint misalignment in blind T-joints. This research showed that axial force varies as the tool offset from the center line of the T-joint changes, and this was exploited to estimate tool position. Finally, Fleming et al. (2009) demonstrated the use of this tracking system, which utilized a weaving process in which axial force measurements are compared and tool path corrections are made if necessary. Figure 17 below displays the data from this demonstration.

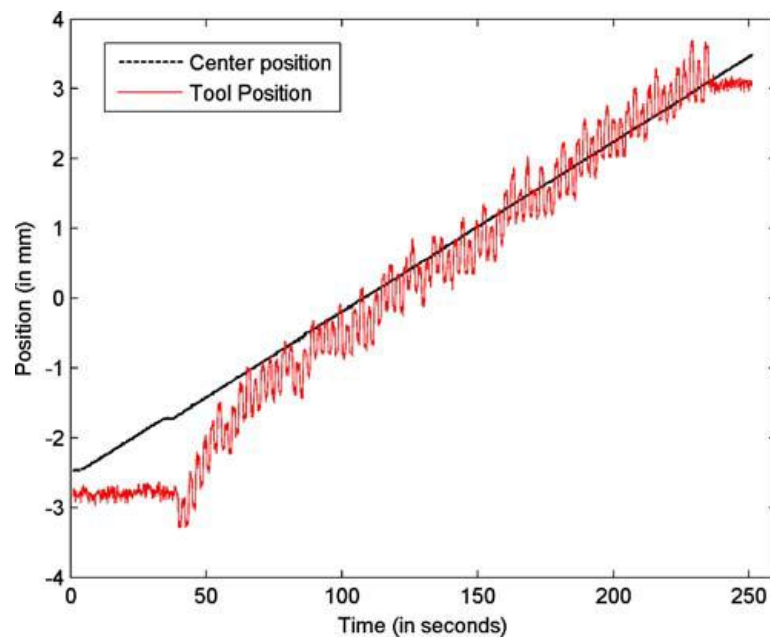


Figure 17, Demonstration of Tracking a Blind T-Joint (Fleming et al., 2009)

Without the measurement of force in FSW, this type of tracking system would not be possible.

Automatic Welding Machinery

The work presented here focuses on implementing custom, low-cost force measurement methods in FSW, to be used specifically at the Vanderbilt University Welding Automation Laboratory (VUWAL). While there are many commercially available FSW articulated robots and gantry style robots, VUWAL has built a custom machine for FSW, based around a Milwaukee #2K Universal Horizontal Milling Machine. This machine is pictured in Figure 18 below.

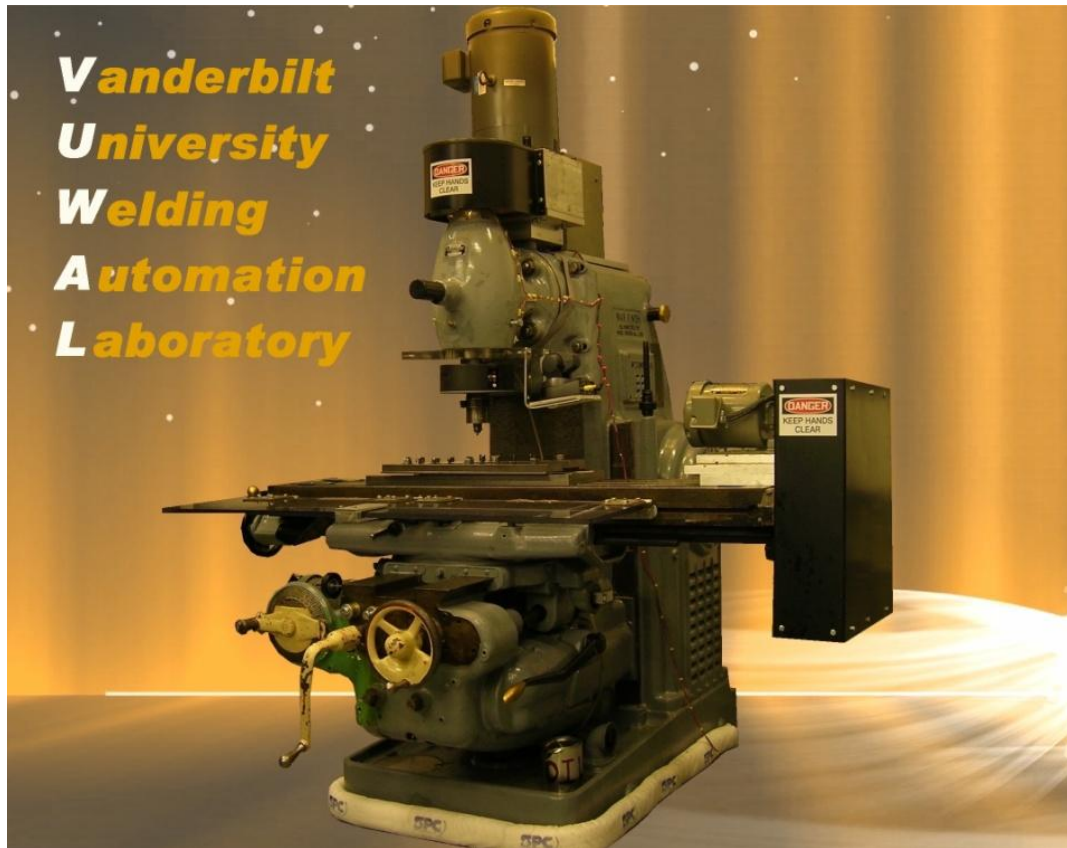


Figure 18, VUWAL FSW Robot

The milling machine has been outfitted with a Kearney and Trecker head attachment that converts it to a vertical orientation. The head attachment and the motion drives on the x, y, and z axes have been outfitted with motors that are appropriate for the speeds, torques, and positioning resolutions needed on each individual axis. Table 3 summarizes the motors, their controllers, and the position sensors that have been retrofitted to the milling machine.

Table 3, Motors, Controllers, and Sensors on the VUWAL FSW Robot

Motion	Motor	Controller	Position Sensor
Traverse (X)	U.S. Electric TF GDY TE Syncrogear, 1 hp	Eaton Cutler-Hammer, MVX9000	UniMeasure LX-PA-50
Lateral (Y)	U.S. Electric TF GDY TE Syncrogear, 1 hp	Eaton Cutler-Hammer, MVX9000	UniMeasure LX-PA-50
Vertical (Z)	Parker Compumotor Servo, Model 730 MTR	Compumotor KHX 750	RENISHAW RGH41T30D05A
Spindle	Baldor Industrial VM 2514, 20 hp	Eaton Cutler-Hammer, SVX9000	N/A

These modifications allow the milling machine to be controlled automatically from a computer that has access to the sensor data and can communicate with the motor drives. All sensor data goes into a central sensor box that is connected to a Dell Precision 340 that runs Microsoft Windows XP. The automatic weld script is written with C# and a Graphical User Interface (GUI) has been developed that allows the user to easily enter

welding parameters and manually run motors to desired positions. A screenshot of the GUI is displayed in Figure 19. Also connected to the computer for data acquisition purposes is a National Instruments DAQ, model USB-6008. More detail on this device and the weld code that makes it operate will be provided in the axial force measurement chapter, as it is used as the input for that particular force data. Additionally, this automatic welding system is continually being updated to support advancements in sensing and GUI user-friendliness. At the present time, the master computer is being updated to a DELL Vostro 230, which features a dual-core processor that will unlock the potential of the parallel, or threaded, programming method that is used in the weld code.

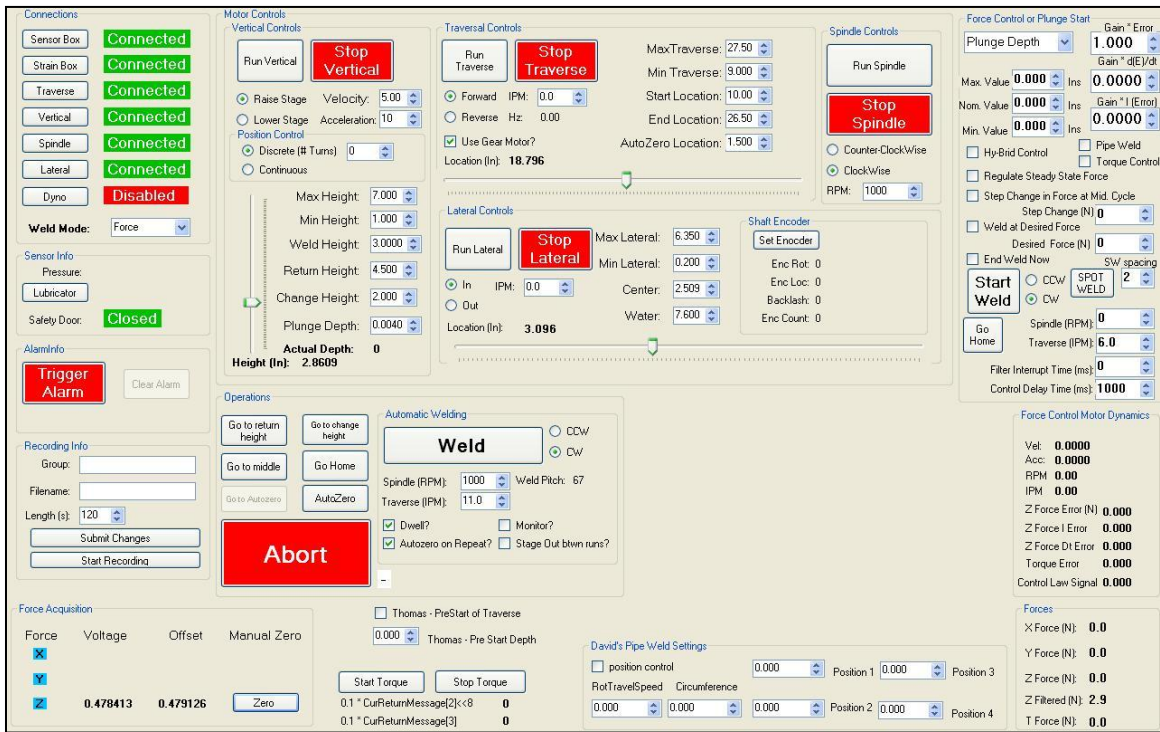


Figure 19, Automatic Welding GUI

The GUI is also being expanded to a touch screen monitor that will be mounted on or near the milling machine. This will allow the operator to easily enter commands and observe the machine motion simultaneously.

Until recently, a Kistler 9123CQ01 rotating cutting-force dynamometer was used to measure force data during welding. It is to be replaced with a custom system that is both lower in cost and more robust to the harsh vibration and temperature environment of FSW. The development of this system is the focus of this thesis.

CHAPTER II

AXIAL FORCE MEASUREMENT

Introduction

The forces of greatest interest in FSW are axial force (F_z) and torque (T). In order to replace a Kistler 9123CQ01 rotating cutting-force dynamometer that had previously been used at VUWAL, it was proposed to begin by measuring axial force by monitoring the axial deflection of the milling machine vertical head. This chapter outlines the development of this system in great detail from proof-of-concept to completion.

Proof-of-Concept

The concept of measuring axial force by monitoring the deflection of the milling machine vertical head is not a complicated one; however, the question was whether or not the deflection could be detected on such a large, massive cast iron structure when, at times, the loads are relatively low, as when the tool auto-zeroing automatic script is running on the machine. A proof-of-concept experiment was designed and conducted in which strain gages mounted both on top and bottom of the head measured compressive and tensile strains, respectively while increasing axial loads were applied to the spindle shaft. Figure 20 displays a concept drawing of this experiment. Single strain gages were mounted on top and bottom. The strain gages selected for use in the experiment were Vishay Micro-Measurements general purpose strain gages, model C2A-06-250LW-350.

The grid resistance for these gages is 350 ohms and they have a gage factor of $2.095 \pm 0.5\%$. These gages also come with pre-attached leads and cables.

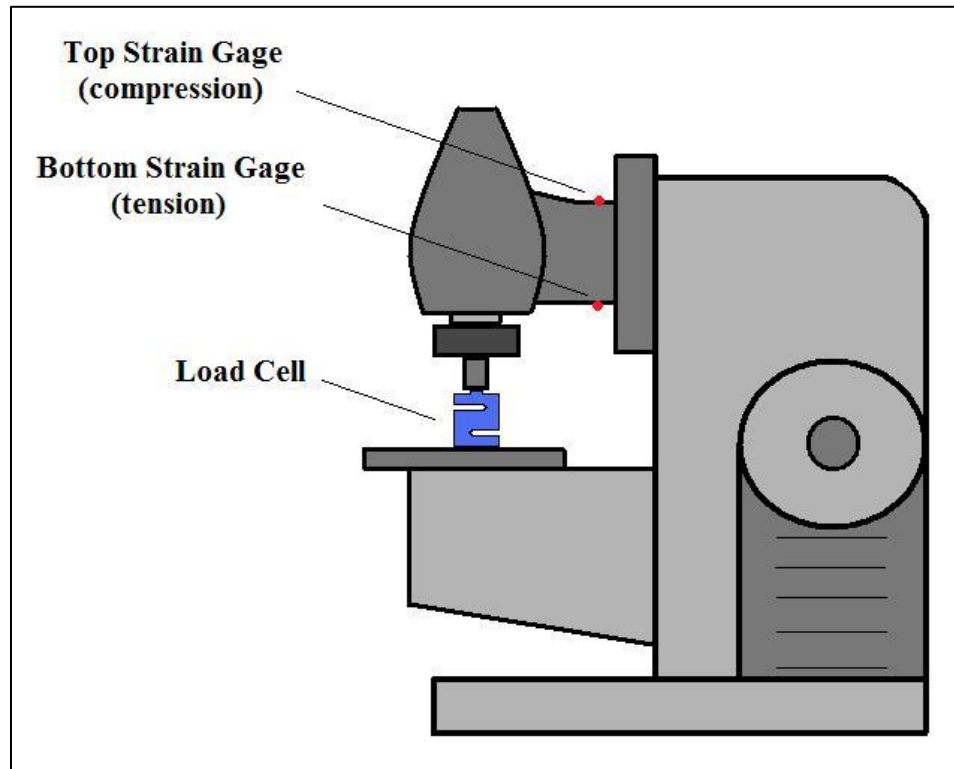


Figure 20, Axial Proof-of-Concept Experimental Setup

Strain was measured using a Vishay Micro-Measurements P-3500 strain indicator, and a switching and balancing unit was used to monitor readings from both strain gages during the experiment. The P-3500 features internal bridge completion circuits for 120, 350, and 1000 ohm quarter bridges, making it a fast and convenient option for this experiment. The load cell selected for use was the Omega Model LCCA-15k, which has a 15,000 lb load capacity. Loads were to be applied by raising the milling machine table in an incremental manner from 50 N to 8,000 N, which could be considered a typical axial force load for an aluminum butt weld. Due to the sensitivity of the load with respect to

vertical position on the machine, it was not possible to hit each desired load exactly, so the actual load applied was recorded. Strain was monitored and recorded for each gage at each load. Table 4 displays the raw data from this experiment.

Table 4, Axial Proof-of-Concept Data

Target, N	Actual, N	Actual, lb	Top Strain	Tare	Stress, psi	Bottom Strain	Tare	Stress, psi
50	39.2	8.8	-3	0	0	-1	0	0
75	78.5	17.6	-3	0	0	-1	0	0
100	117.7	26.5	-4	-1	-13.4	-1	0	0
150	157.0	35.3	-4	-1	-13.4	-1	0	0
200	196.2	44.1	-4	-1	-13.4	-1	0	0
250	235.4	52.9	-4	-1	-13.4	-1	0	0
500	637.7	143.3	-5	-2	-26.8	0	1	13.4
750	765.2	172.0	-5	-2	-26.8	0	1	13.4
1,000	990.8	222.7	-5	-2	-26.8	0	1	13.4
1,500	1,461.7	328.6	-6	-3	-40.2	1	2	26.8
2,000	2,011.1	452.1	-6	-3	-40.2	2	3	40.2
2,500	2,462.3	553.5	-8	-5	-67	3	4	53.6
3,000	2,972.4	668.2	-9	-6	-80.4	4	5	67
3,500	3,423.7	769.6	-10	-7	-93.8	4	5	67
4,000	3,924.0	882.1	-11	-8	-107.2	5	6	80.4
4,500	4,385.1	985.8	-12	-9	-120.6	6	7	93.8
5,000	4,973.7	1,118.1	-13	-10	-134	6	7	93.8
5,500	5,424.9	1,219.5	-15	-12	-160.8	6	7	93.8
6,000	5,886.0	1,323.2	-15	-12	-160.8	7	8	107.2
6,500	6,347.1	1,426.8	-16	-13	-174.2	7	8	107.2
7,000	6,847.4	1,539.3	-18	-15	-201	8	9	120.6
7,500	7,406.6	1,665.0	-19	-16	-214.4	8	9	120.6
8,000	7,789.1	1,751.0	-20	-17	-227.8	9	10	134

The strain data was zeroed in the post-processing, and this data is shown in the ‘Tare’ column of Table 4. In addition, the theoretical stress was calculated using Hooke’s Law as follows for the top strain gage’s final data point:

$$\sigma = E * \epsilon$$

$$\sigma = (13.4 \times 10^6 \text{ psi}) * (-17 \times 10^{-6} \text{ in/in})$$

$$\sigma = -227.8 \text{ psi} = -1.57 \times 10^6 \text{ Pa}$$

Different cast irons can have a range of moduli of elasticity from 12×10^6 psi to 25×10^6 psi (Gere, 2004). For cast iron at room temperature, 13.4×10^6 psi is a value that is commonly used. The calculated stress values will be compared to values determined through Finite Element Analysis (FEA) in the next section.

Finally, the strain values were plotted against axial load to determine the response of the system. This plot can be seen in Figure 21.

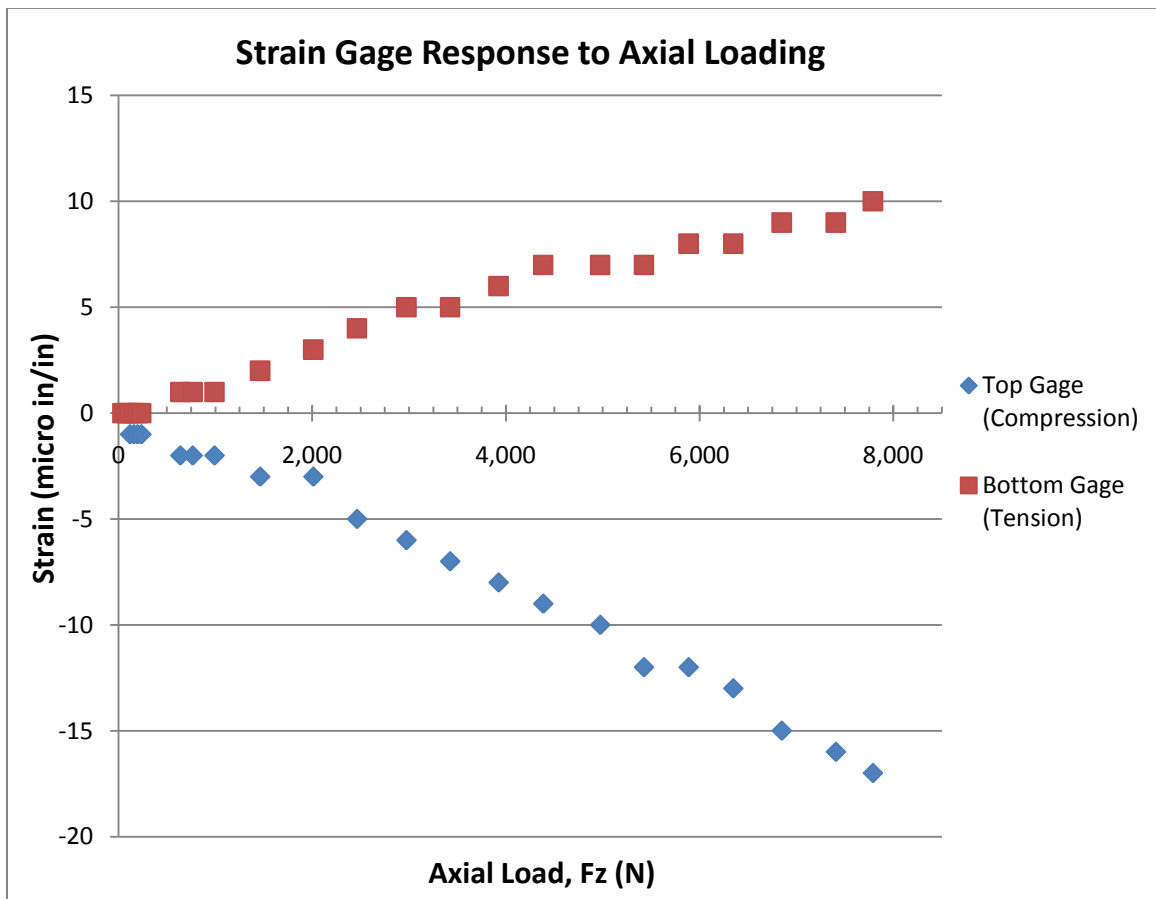


Figure 21, Strain Gage Response in Proof-of-Concept Experiment

As can be seen in Figure 21, the response for each gage is relatively linear. It can also be determined from this graph that the measurement point on top of the head is more sensitive to axial loading than the measurement point on the bottom of the head, due to the slope (strain/load) of the response lines. At either point however, the response is measurable. Therefore, it was determined that measuring axial load by monitoring the deflection of the milling machine head using strain gages is a viable alternative.

Additional questions remained however. It was also proposed that perhaps the traversing (F_x) and side (F_y) forces could be measured in a similar fashion, mounting strain gages at other locations on the head. There was also the issue of crosstalk between forces, such as a side force contributing to the axial force measurement during welding. In order to answer these questions and to also confirm the data recorded in the proof-of-concept experiment, a Finite Element Analysis (FEA) was conducted on the milling machine head.

Finite Element Analysis

In order to better understand the interaction of process forces and how they react against the milling machine head, a Finite Element Analysis (FEA) was conducted. The goal of this analysis was threefold:

- 1) Determine if traversing (F_x) and side (F_y) forces could be measured by placing strain gages at particular locations on the head*
- 2) Examine cross-talk between forces*
- 3) Confirm the strain measurements taken during the proof-of-concept experiment*

For this type of analysis to be completed, an accurate model of the head needed to be developed in a three-dimensional computer aided design and drafting (CADD) software package. Autodesk Inventor was selected for this task. Using information from the Kearney and Trecker AEC-1D product manual and measurements taken from the machine itself, a CADD model was developed. Figure 22 displays a screenshot of this model within the Inventor drafting environment.

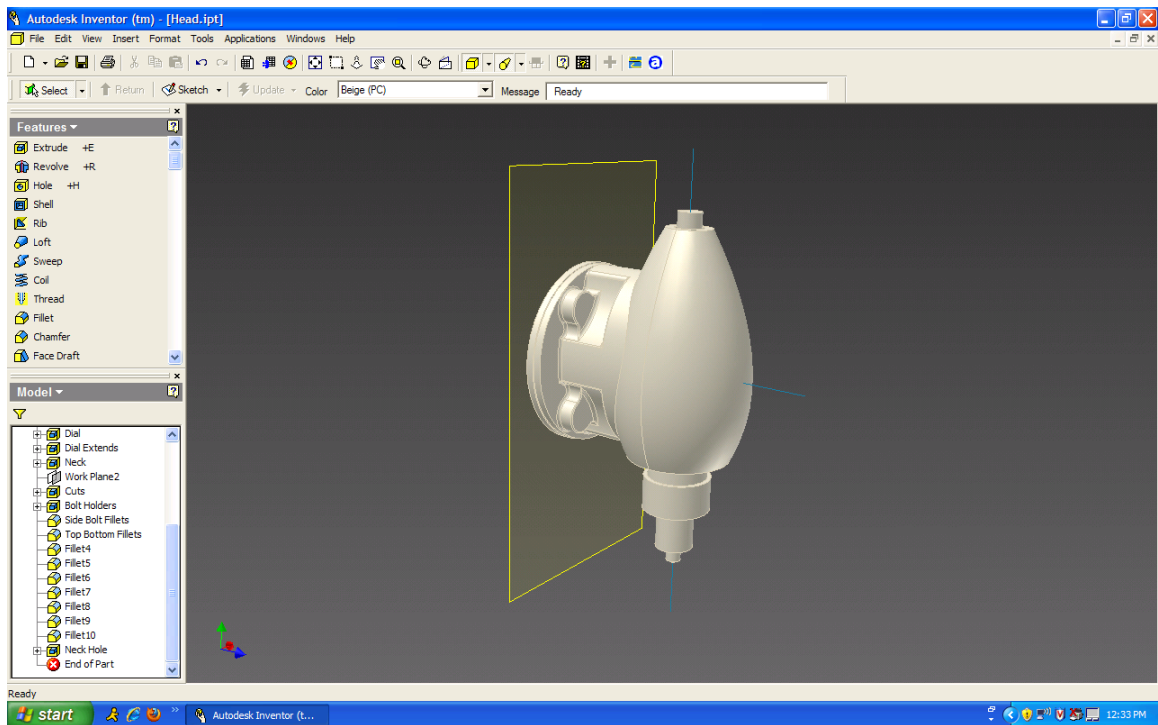


Figure 22, Screenshot of Milling Machine Head CADD Model

The outer surfaces of the model are dimensionally accurate, with the exceptions being the spindle and other components mounted on the spindle. Items such as the since-replaced Kistler dynamometer and the tool chuck were modeled as a solid piece without much detail along with the spindle for the purpose of simplicity. The goal of the analysis was

not to analyze these components or the stresses they experience under loading. For the purposes of this exercise, they merely transmit the forces to the components of interest. Some approximations were made however when the inner components of the head were dimensioned. No information was readily available concerning wall thickness or any other design features of the head. The inner structure was modeled as a spindle with bearings at both top and bottom, which is accurate. Figure 23 displays a screenshot of the CADD model with the inner structure visible.

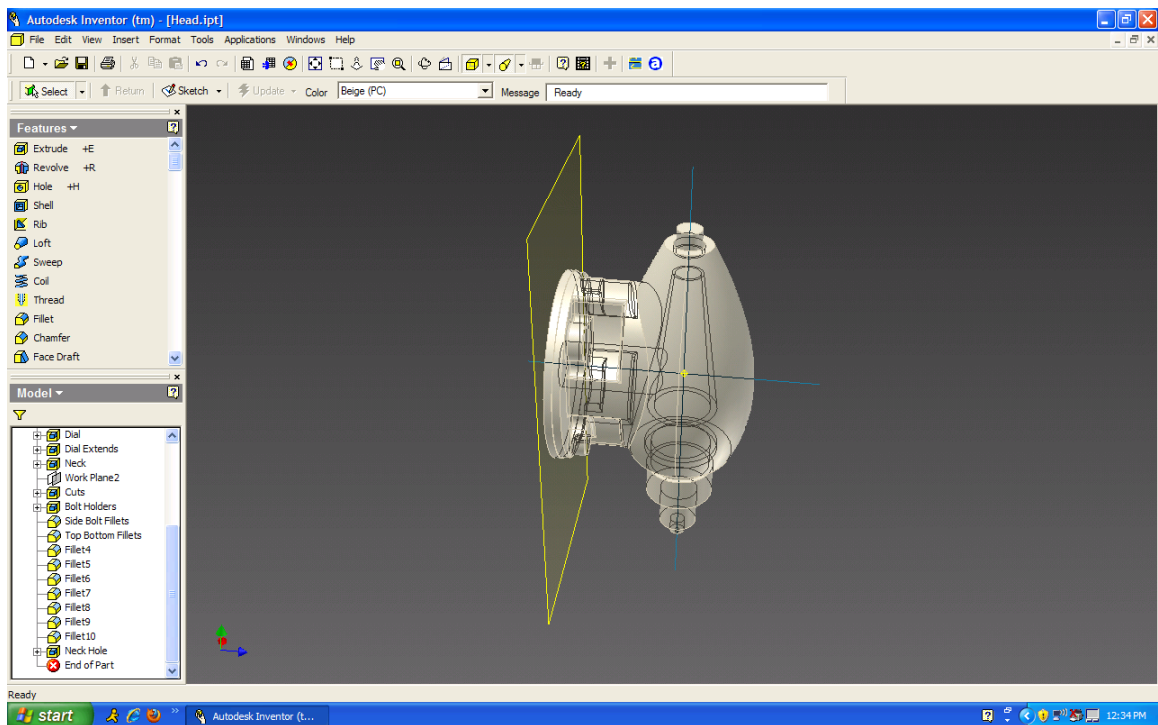


Figure 23, Screenshot of CADD Model with Visible Inner Structure

The FEA analysis was conducted using Comsol Multiphysics, which is a module-based simulation platform that supports analysis within many traditional areas such as heat transfer and structural mechanics, but also supports analysis of coupled systems such

as fluid-structure interaction, electro resistive heating, and thermal stress. Comsol transforms coupled partial differential equations into forms that are appropriate for numerical analysis and solves them using the finite element method. What was particularly attractive about Comsol for this project was that it allows the user to link a CADD file from another program such as Inventor to the multiphysics model.

The Inventor CADD file of the milling machine head was imported into a Comsol stress-strain analysis file, and a mesh was generated automatically. This resulted in a mesh consisting of 95,925 elements. Figure 24 displays the mesh that was generated along with an exploded view.

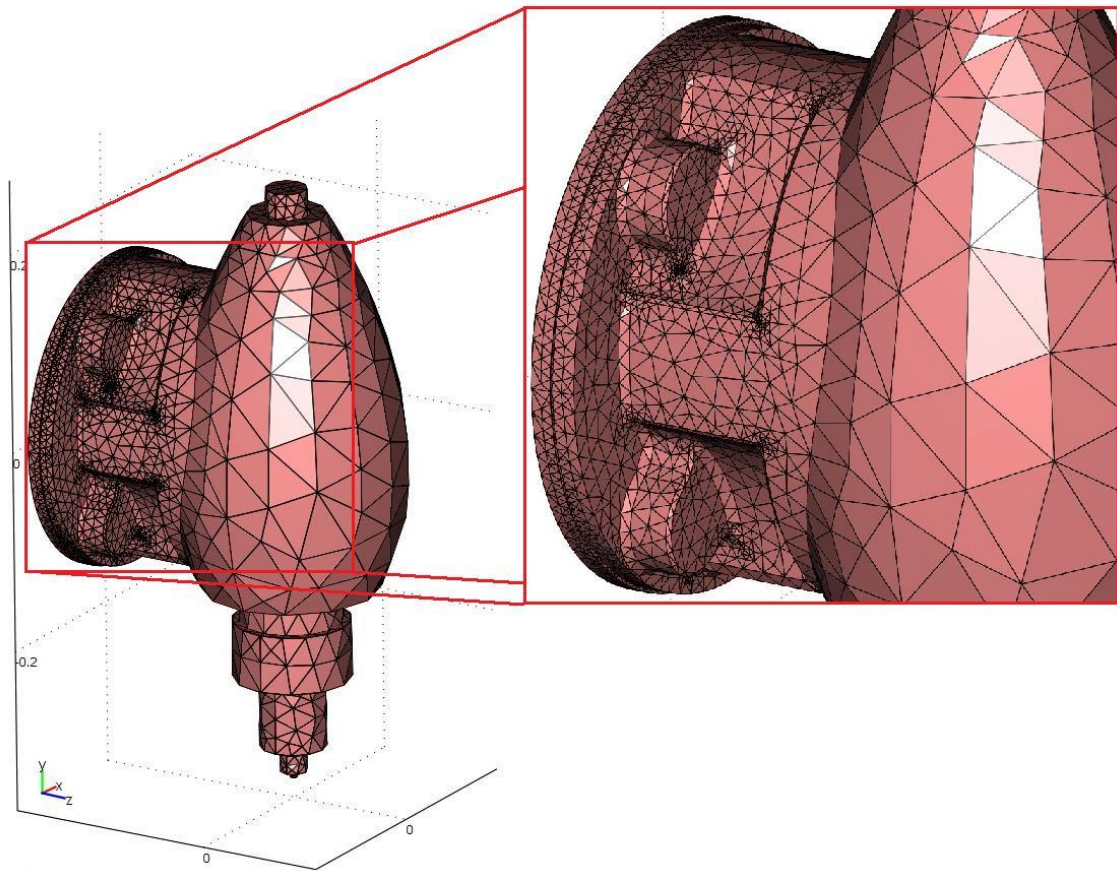


Figure 24, Mesh for Finite Element Analysis

The first simulation was conducted in a manner that would allow for the confirmation of the strains measured in the proof-of-concept experiment. The highest load applied during this experiment, which was 7,789.1 N, was applied uniformly to the tool probe and shoulder in the axial direction. Figure 25 displays the simulation results in the form of von Mises stresses for this loading scenario.

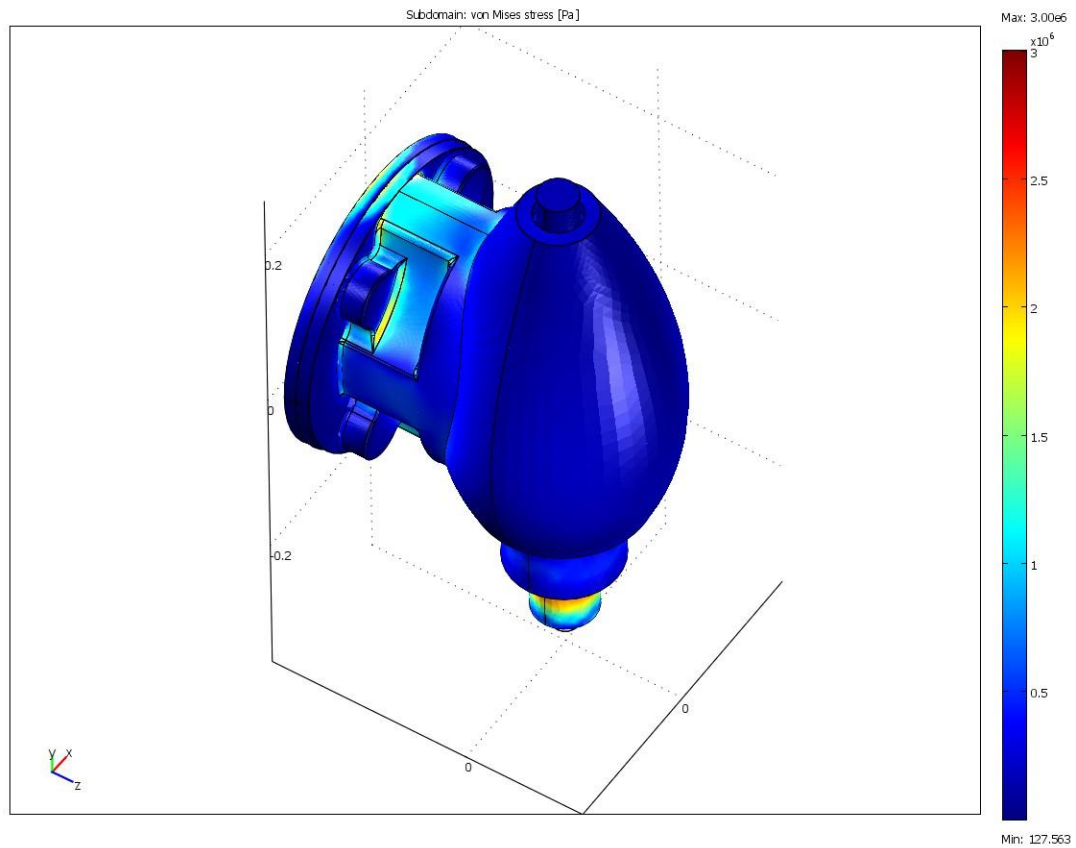


Figure 25, Results of Proof-of-Concept Confirmation Simulation

The stress experienced at the point of strain gage application on the top side of the head in the simulation was 1.25×10^6 Pa. This value can be determined via the color scale on the right side of Figure 25. As calculated previously, the experimental value for stress

measured at this point was 1.57×10^6 Pa. The negative sign has been removed since it is understood that compressive stress is experienced at this point. Comparing these two experimental and theoretical values, the percent difference is 22.7%. This difference can likely be attributed to two main factors. Most significantly, the approximations used in modeling the inner structure of the milling machine head led to the head having thicker walls and a more robust structure in general. This would lead to a lower simulation stress at the measurement point. Secondly, the low resolution of the strain measurement from the P-3500 indicator means that a single digit change in the strain reading leads to a 9×10^4 Pa change in the measured stress. So, the experimentally measured value could potentially be closer to the theoretical value, but it could not be detected. Nevertheless, it is encouraging that the experimental and theoretical values of stress are of the same order of magnitude. This analysis confirmed that the FEA model is valid for determining if other forces can be measured from the milling machine head, as this analysis will mainly be a qualitative comparison of the stresses resulting from different loading scenarios.

The next step was to run a series of simulations that consisted of all the possible loading scenarios for the milling machine head. The forces of interest were axial (F_z), traverse (F_x), and side (F_y) in both the positive and negative directions. The direction of the side force is dependent on the direction of spindle rotation due to the nature of the magnus effect. Figure 26 labels the directions of the forces that were applied. Using the label names established in this figure, Table 5 lists all of the loading scenarios that were simulated along with an index that refers to the simulation image that can be found either in this section or Appendix A. There are eleven combinations in all. Standard loads were selected to be used in all of the simulations. To represent what would be considered

typical loads seen at VUWAL for aluminum welds, the axial load selected was 6,000 N and the traverse and side loads were selected as 400 N.

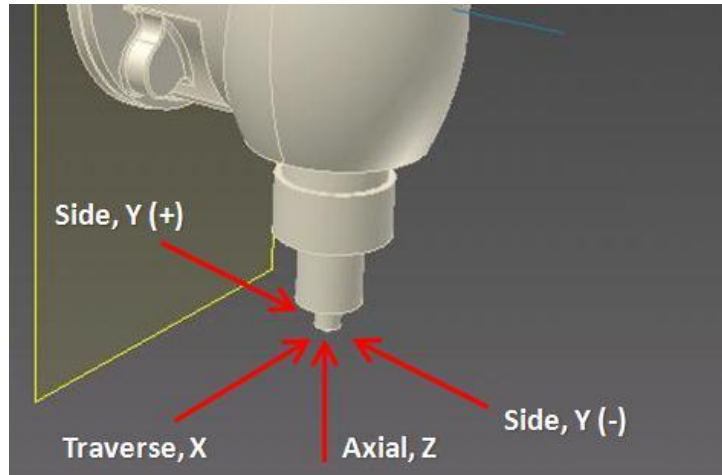


Figure 26, Directions of Force Loading for FEA

Table 5, Loading Scenarios for FEA

Index	Axial, Z	Traverse, X	Side, Y (+)	Side, Y (-)
1	6,000 N			
2		400 N		
3			400 N	
4				400 N
5	6,000 N	400 N		
6	6,000 N		400 N	
7	6,000 N			400 N
8		400 N	400 N	
9		400 N		400 N
10	6,000 N	400 N	400 N	
11	6,000 N	400 N		400 N

Additionally, the stress scale color bar can be adjusted to make the results image more sensitive so that the different loading scenarios can be easily compared. The standard scale for the images is from 127 to 3.00×10^6 Pa, and the sensitive scale is from 127 to

2.5×10^5 Pa. The standard scale is shown for all images, and the sensitive scale is shown for select images of greater interest.

In order to examine the cross talk between the axial force and the side force, which was of concern, simulations 1 and 6 were compared. Figures 27 and 28 display the results from these simulations.

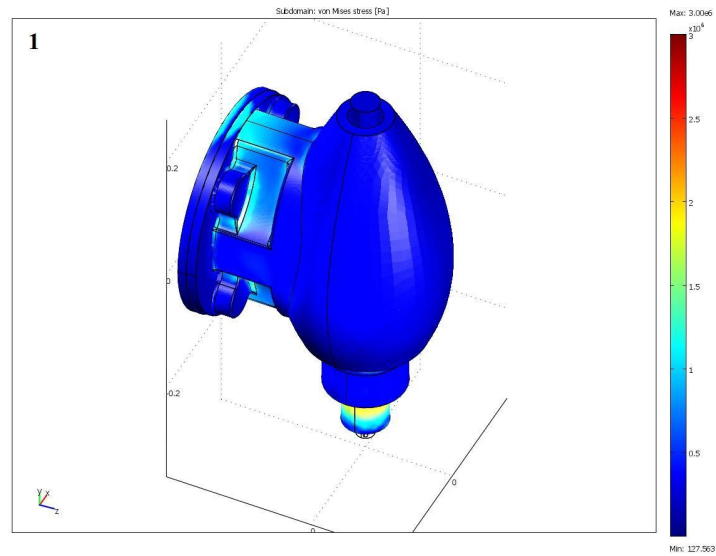


Figure 27, FEA Results for Simulation 1

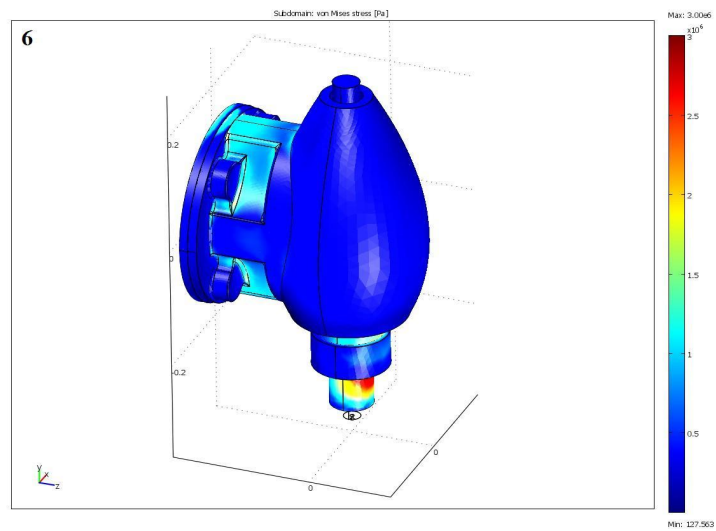


Figure 28, FEA Results for Simulation 6

It can be determined from the simulation results that there may be a slight cross talk issue when the axial force measurement is implemented. There was an increase of approximately 5×10^4 Pa at the strain gage measurement point on the top side of the head from simulation 1 to 6. In order to compensate for this cross talk, which is approximately 4%, the side force will have to be measured however. This will be discussed more in the axial force implementation section.

The question of whether or not additional forces could be measured with strain gages at certain points on the head was answered by comparing all of the FEA simulation results. The answer seems to be that the axial force completely dominates the stresses that are experienced on the head and would make measuring the other forces which are much lower in magnitude very difficult or impossible. This can best be illustrated by comparing simulations 2 and 10. Simulation 2 features only a traverse force and is pictured in Figure 29 at the sensitive scale.

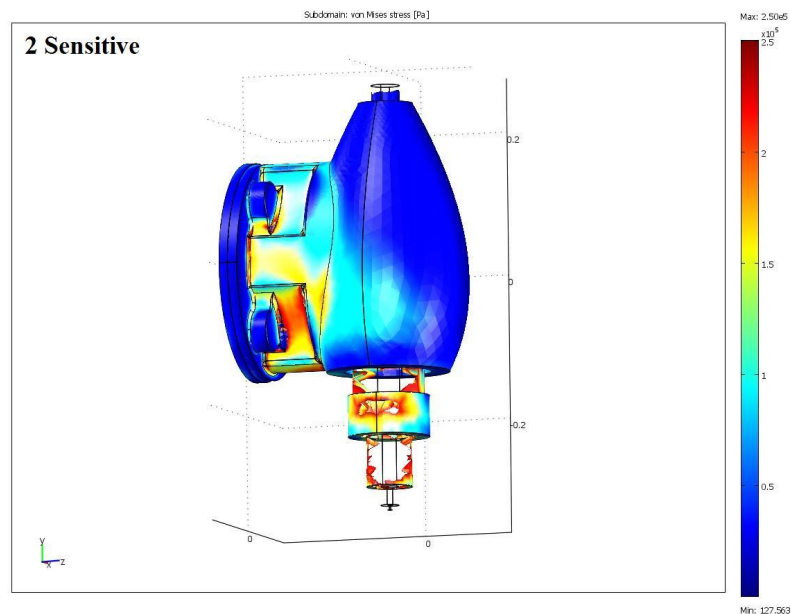


Figure 29, FEA Results for Simulation 2

The results of simulation 2 seem to indicate that there is a point of higher relative stress near the bottom side of the head that could be exploited for measurement purposes. Look however at the results of simulation 10 on the sensitive scale in Figure 30, which features the same traverse force but with an axial force and side force as well.

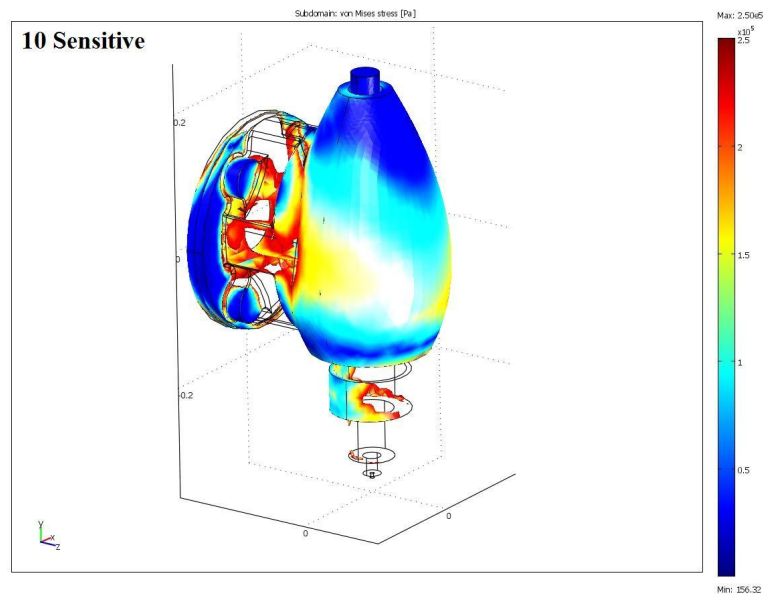


Figure 30, FEA Results for Simulation 10

The measurement point of interest from simulation 2 is now being dominated by the axial force and the stress is above the maximum on the color bar. This suggests that even if the traverse force could be measured alone, the issue of cross talk interference from other forces, particularly axial, would be a major problem. It is for this reason that only the axial force measurement will be implemented using strain gages on the milling machine head. The traversing and side forces will be measured using alternate methods, and then the issue of the axial force measurement being affected by these lesser in magnitude forces will be addressed.

Implementation and Calibration

In order to fully implement axial force measurement for both data recording and control, a custom system had to be designed and constructed. The P-3500 strain indicator that was used in the proof-of-concept experiment is very convenient for single iteration lab-type experiments, but a data acquisition system was needed that could meet all of the following requirements:

- 1) *Simple, Reliable, User-friendly*
- 2) *Allows for real-time data input into weld controller computer*
- 3) *Low cost*

Upon consultation with colleagues in the VU Mechanical Engineering department, the system shown in Figure 31 was designed and implemented.

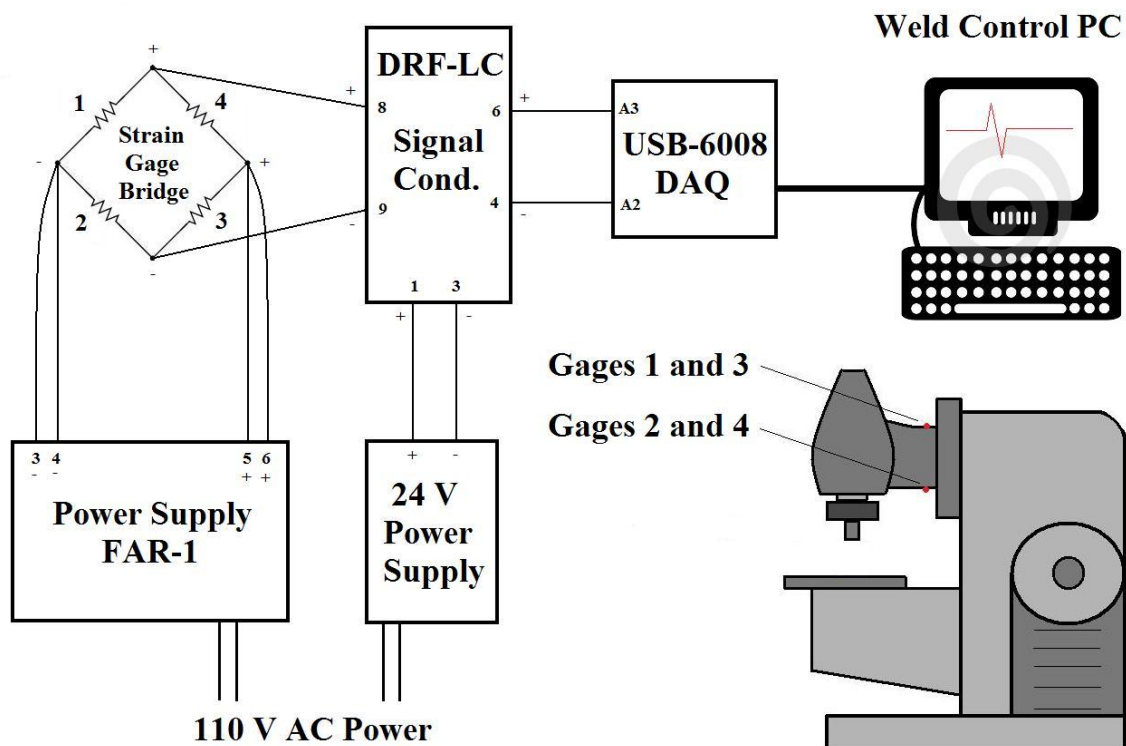


Figure 31, Axial Force Data Acquisition Circuit

The sensing element is a full bridge of Vishay Micro-Measurements C2A-06-250LW-350 strain gages. The gages are mounted in a back-to-back bending configuration which is both highly sensitive and temperature compensated. Essentially, a full bridge acts as a voltage divider, and using the labeling conventions established in Figure 31, the bridge can be analyzed as follows:

$$V_8 = \frac{R_1}{R_4+R_1} * V_{in} \qquad V_9 = \frac{R_2}{R_3+R_2} * V_{in}$$

The resistance values change as the strain gages experience a load, and the signal conditioner measures the difference between V_8 and V_9 . If the gages experience a temperature change, the resulting change in resistance will be the same on both side of the bridge due to the gage layout, giving the system temperature compensation.

An Omega FAR-1 power supply was selected for this application. It is a precision 10V power source that can accommodate up to four 350-ohm bridges operating in parallel. The output of the bridge goes into an Omega DRF-LC signal conditioner that is specifically designed for use with load cells. It features an *offset* potentiometer for zeroing the signal when there is no load on the system, and there is a grid of jumpers to increase the offset if necessary. The signal conditioner also features a variable gain *span* potentiometer which allows the output range of the bridge to be adjusted to fill the output range of the conditioner. It is powered by a standard 24V, 500 milliamp power supply.

The output of the signal conditioner is read by the National Instruments USB-6008 data acquisition device or DAQ that was mentioned previously in the automatic welding machinery section. This device features 8 analog inputs at 12 bits and 8 digital inputs as well. It can be configured for use with NI LabVIEW or custom code written in

a variety of languages. The cost of this system is outlined in Table 6, excluding the USB-6008 device because it did not have to be purchased and was already being used for data input tasks at VUWAL.

Table 6, Cost of Axial Force Measurement System

Item	Description	Qty	Cost
Power Supply	Omega FAR-1 Precision 10V	1	\$123.00
Power Supply	Standard 24 V, 500 mA	1	\$12.42
Signal Conditioner	Omega DRF-LC Signal Conditioner	1	\$180.00
Strain Gages	Vishay Micro-Meas. C2A-06-250LW-350	4	\$28.52
Total Cost:			\$343.94

The cost to develop this system is lower than the cost of even the cheapest commercially available load cell listed in Table 2. Additionally, if the cost of the USB-6008 device were to be included, the total cost would be increased by only \$169.00.

To calibrate this system, a similar technique was used as in the proof-of-concept experiment. Once again, the Omega Model LCCA-15k load cell with a 15,000 lb capacity was used to measure increasing axial loads that were put on the system by raising the milling machine table. The voltage signal was monitored using the USB-6008 device configured for use in NI LabVIEW. Loads were increased at pre-determined intervals from 0 N to approximately 5000 N after the signal conditioner had been zeroed at the no-load state. At each load interval, voltage data was recorded at 10 Hz for 5 seconds. Then, all of the values recorded at each interval were averaged to help remove some noise. Figure 32 displays the calibration chart with a linear trendline fit to the data. All of the raw voltage data from the calibration can be found in Appendix B. The

calibration is highly linear as can be seen from the R^2 value of 0.9991, and the calibrated gain for the system is 17,760 N/V.

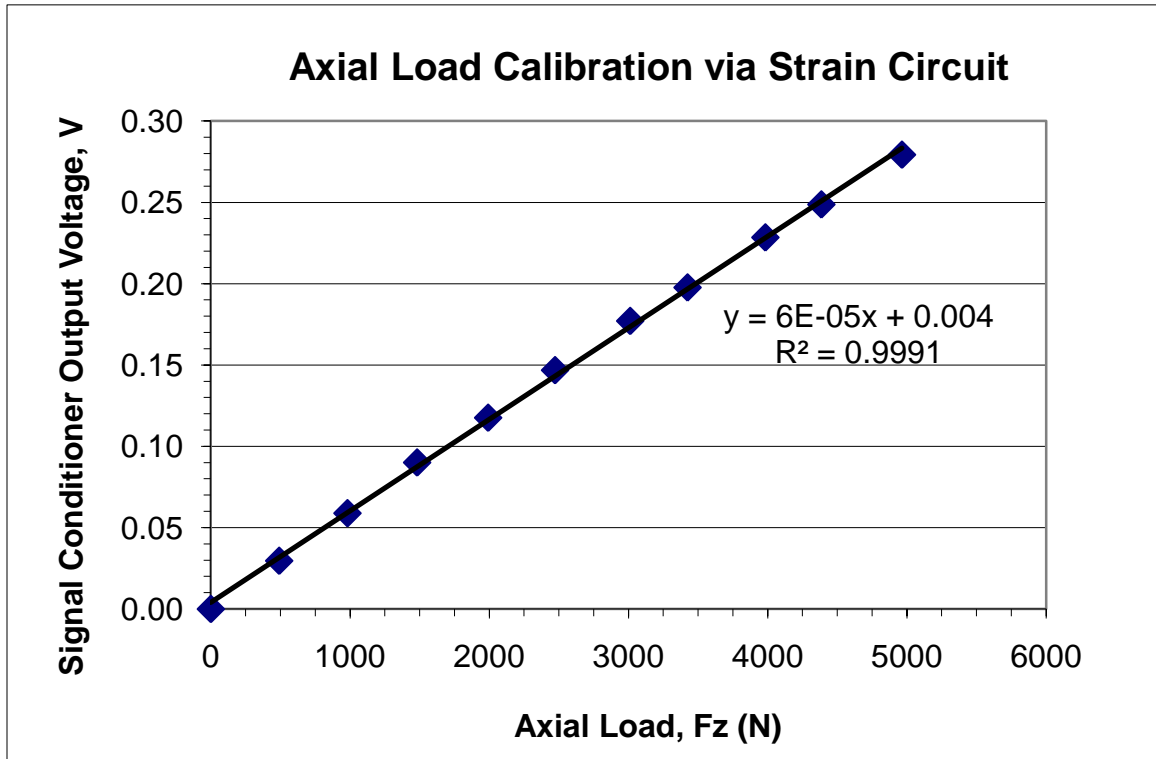


Figure 32, Axial Load Calibration

While recording data in LabVIEW was adequate for calibration purposes, the USB-6008 device had to be configured to operate with the custom C# welding code in order to get the axial force variable inside the weld program for data logging and control. This was not trivial because VUWAL researchers had not used this device for an analog input to the weld program before. The C# code must specify certain aspects of the operation when the device is setup, including the wiring configuration, the maximum and minimum voltage inputs, and the units of measure. The device was set up for differential wiring with an input range of -0.1 V to 1 V. The C# code that specifies this is:

```

strainTask = new Task();
AIChannel strainChannel;
strainChannel = strainTask.AIChannels.CreateVoltageChannel(
    "dev2/ai0", //Physical name of channel
    "strainChannel", //The name to associate with this channel
    AITerminalConfiguration.Differential, //Differential Wiring
    -0.1, //-0.1v minimum
    1, //1v maximum
    AIVoltageUnits.Volts //Use volts
);

```

The device can handle a voltage input up to ± 10 V, but setting the input bounds closer to only what is needed for the application often results in a higher resolution. With the 12 bit device set to a range of -0.1V to 1V, the resolution is 0.0002686 V, which translates into a 4.8 N resolution in the force measurement.

A function called `onStrainMeasure()` was setup in the sensor box loop to call a single reading to be taken from the USB-6008 device. This function looks like:

```

//Function called to take single reading from NI DAQ for ZForce measurement
void onStrainMeasure()
{
    //Old function format example: onStrainMeasure(object sender, EventArgs e)
    //StrainMeasure = new Thread(new ThreadStart(FcnStrainMeasure));
    //StrainMeasure.Start();
    AnalogSingleChannelReader strainReader = new
    AnalogSingleChannelReader(strainTask.Stream);

    Zvolt = strainReader.ReadSingleSample();
    Ztemp = 17760 * (Zvolt - Zoffset); //Subtract offset and multiply gain
}

```

The sensor box calls this function at a rate of approximately 33.33 Hz, which is determined by computer processor speed. The function subtracts any voltage offset that is determined when the input is zeroed for the no-load condition and multiplies the gain that was determined during the calibration. Once the sensor box is connected to the weld computer, the axial force reading is continually available for both data logging and control.

Auto-Zero Process

The auto-zero process is a function in the weld code that allows the tool to be lowered to the workpiece and sense when the shoulder touches in order to set the weld height. This is incredibly important for position controlled welds, which is the type of weld that is most commonly performed at VUWAL. The auto-zero process had previously been implemented with the Kistler dynamometer, and thus the process involved a complicated communication scheme between the dynamometer computer and the weld computer. The steps in the process were:

- 1) Raise the table at a continuous, steady rate until an axial force is sensed*
- 2) Lower the table slightly*
- 3) Raise the table in increments of discrete motor rotations*
- 4) Stop the table when an axial force is sensed and record the vertical position*

The purpose of step 1 is to quickly get a rough estimate of the auto-zero position. Then in step 3, a more accurate position is determined by raising the table in discrete intervals at a slower pace. The process was kept the same for implementation with the new axial force measurement system, but the entire process now takes place on the weld computer.

Before the auto-zero process can even be initiated by the user, the computer confirms that communication with the axial force measurement via the USB-6008 device is established. This is a safety feature that prevents the user from trying to auto-zero when there is no feedback signal for stopping the vertical motor. The auto-zero code also automatically zeroes the axial force reading and later confirms that the force is not

already above the cut-off value when the process actually starts. The axial cut-off force was set relatively low at 100 N, and the code for the first upward motion looks like:

```
if (ZForce > 100) // This is a test for initial force
    MessageBox.Show("Force Already Exceeds Turn-On Force");
else
{
    MessageBox.Show("The AutoZero Process Will Now Begin");
    //Alert GUI of first upward motion
    isAutoisfirstup = true;

    //initiate table raising and wait for alert from other computer
    VerPort.Write("MC H+ A10 V.8 G\r");

    //wait for stop signal
    //while(!DynStream.DataAvailable) //comment out Chase
    //    Thread.Sleep(1); //comment out Chase
    while(ZForce < 100)
        Thread.Sleep(1);
    //Stop the motor
    StopVer();
}
```

Once this first action is completed, the table lowers, and the code for the second upward motion looks like:

```
////Do final upward in a loop
bool LoopRepeat = true;

while (LoopRepeat)
{
    //Wait for turn off signal
    if (ZForce > 100)
        LoopRepeat = false;
    else
        VerPort.Write("MN A1 V1 D100 G\r");
    Thread.Sleep(1500);
}
```

The vertical position is then recorded and the specified plunge depth is added to it in order to set the proper weld height. To test the auto-zero process with the new axial force measurement system, the auto-zero function was tested at four different locations on a

piece of ¼” aluminum that had been clamped to the anvil, with five iterations at each location. The results of this test are displayed in Table 7.

Table 7, Results of Auto-Zero Test

Auto-Zero Height (inches)					
Location	1	2	3	4	5
A	6.0093	6.0097	6.0093	6.0093	6.0097
B	6.0097	6.0097	6.0097	6.0097	6.0097
C	6.0093	6.0026	6.0097	6.0093	6.0093
D	6.0097	6.0101	6.0101	6.0101	6.0097

The system performed well, with a variability of 0.0004 inches at some locations. This is the measurement resolution of the RENISHAW vertical position sensor. The auto-zero process needs only to consistently determine the weld height with a resolution of 0.001 inch, as this is the typical increment used to specify plunge depth. There was one bad reading in the test however, which was iteration 2 at location C. The auto-zero height was roughly 0.007 inches below the correct position, and this was mostly likely caused by some noise in the axial force measurement system that could result in the vertical motor stopping prematurely. Typically the user would notice an inaccuracy as blatant as this and would run the auto-zero process again before welding.

Demonstration of Measurement

Several friction stir welds were conducted to initially test the new axial force measurement system, and the system has now been in use at VUWAL for approximately one year. The results from an early test are displayed in Figure 33. This test was

conducted by welding Al 6061 in a butt joint configuration with a Trivex tool. The welding parameters were 1400 rpm and 6 ipm with a 0.004” plunge depth and a 1 degree lead angle.

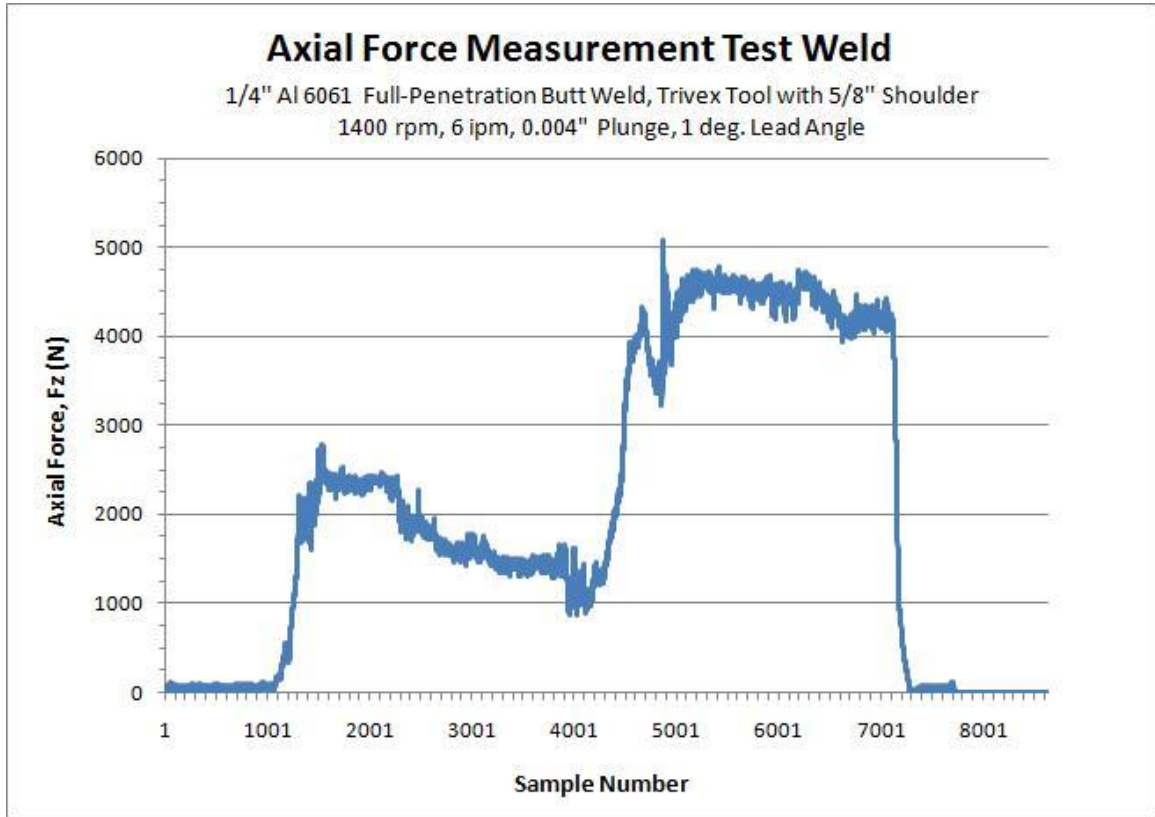


Figure 33, Axial Force Measurement Test Results

The auto-zero system was used to determine the weld height, and then the weld computer automatically recorded axial force data during the weld. The system performed well, as expected.

It is unknown what crosstalk may exist in these axial force measurements for certain without actually measuring the traverse and side forces as well as the torque. The FEA results suggested that it is relatively low, on the order of 4%. In order to

compensate for this crosstalk however, the other forces must be measured in real time. To accomplish this, it was proposed that an instrumented tool holder be designed and constructed that would allow for multiple force measurements and temperature measurements to be taken during the weld. The next chapter of this thesis outlines in great detail the implementation of this system, with a focus on measuring the process torque as the first stage of development.

CHAPTER III

CUSTOM FORCE TRANSDUCER

Introduction

In order to measure additional processes forces beyond just the axial force (F_z), it was proposed that a custom, low-cost force transducer be designed and implemented for use at VUWAL. This system would take the place of the Kistler 9123CQ01 rotating cutting-force dynamometer that had previously been in use. The requirements for such a system would include:

- 1) Simple, Reliable, User-friendly*
- 2) Low Cost*
- 3) Allow for measurement of all FSW process forces as well as tool temperature*
- 4) Adapt to FSW robot with NMTB 50 taper*
- 5) Transmit signals wirelessly from rotating spindle*
- 6) Support real time data rates adequate for force recording and control*

It was decided that the use of slip rings should be avoided in order to eliminate any problems associated with them, such as noise. Therefore, not only must the signals be transmitted wirelessly from the spindle, but the force and temperature sensors must be powered by an on-board source. The method of signal transmission to be selected must support real time data transmission as well as rates that are adequate for measurement and control. This is one of the most critical requirements. A delay in the signal of any

significance would make force control very difficult or impossible. It was also decided that the overall system should be readily adaptable to the FSW machine used at VUWAL, meaning the force transducer would have to feature an NMTB 50 taper. Taking into account these requirements, a concept was developed for this system. This concept is displayed in Figure 34.

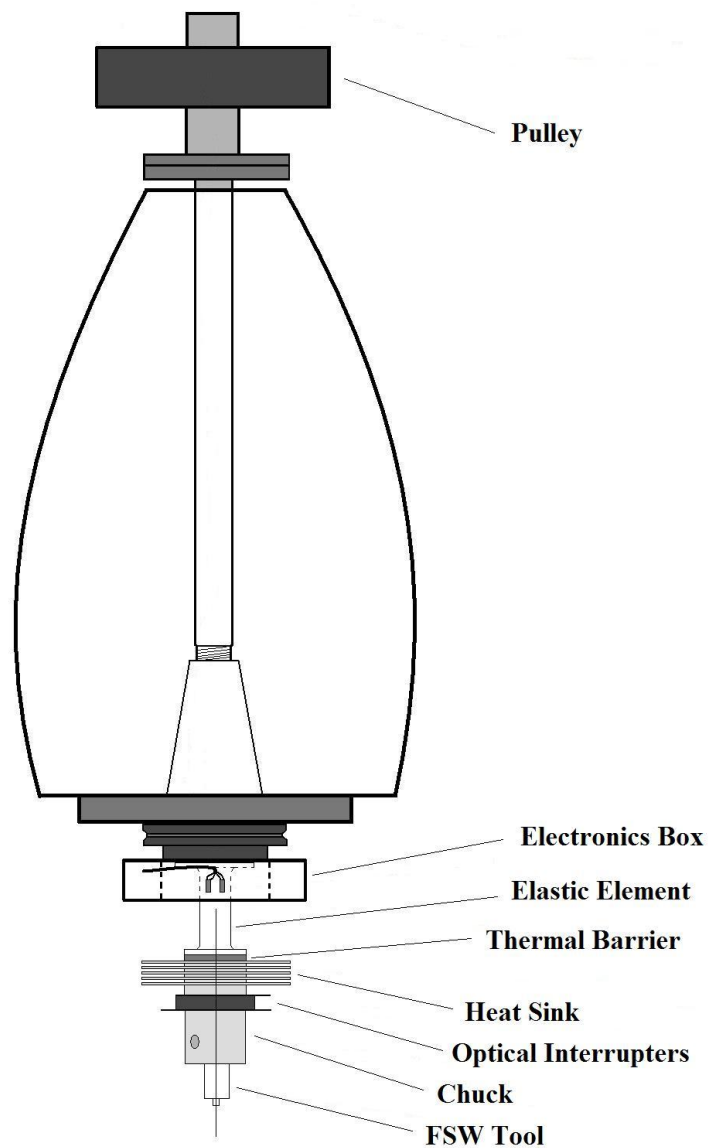


Figure 34, Force Transducer Concept

Borrowing the force measurement technique from Blignault et al. (2008), the main feature of the transducer is an elastic element that is to be instrumented with strain gages. The signal wires from the strain gages would then feed into an electronics box that surrounds, but is not mounted to, the elastic element. The electronics box would hold batteries, amplifiers, and the signal transmission system. A heat sink and a thermal barrier would protect the strain gages from the harsh thermal environment of FSW. The chuck and optical interrupters that had been used the Kistler dynamometer would be reused on this device. The optical interrupters are necessary for resolving the traversing and side forces will be discussed further in a latter section of this thesis. Reusing the chuck allows for the FSW tool design to remain the same at VUWAL, and the machining of many new tools would not be required. All of this would be mounted on an NMTB 50 taper to be custom machined for this device.

This chapter discusses in great detail the design, construction, and implementation of this custom force measurement system. The focus throughout will be on the torque measurement as a first stage of development and a platform upon which other measurements of force or temperature may be made.

Electronics Design

Selection of Data Transmission System

The first step in designing the electronics of the force transducer was to determine what type of system would be used for the wireless transmission of signals from the spindle. Several systems were considered when research into this topic began. There are

many commercially available options for transmitting data wirelessly, most of which use radio frequencies (RF) at 2.4 GHz which is license free worldwide. Omega has developed a system that converts any RS232 device into a wireless device with a USB transceiver. This system is pictured in Figure 35.



Figure 35, Universal Wireless RS232 to USB Transceiver (Universal, 2010)

This device is affordable at only \$159.00, but one of the drawbacks is its bulky size at nearly three inches long by two inches wide. For a slightly smaller option, MicroStrain has developed a system designed specifically for transmitting strain measurements wirelessly. This device is pictured in Figure 36.



Figure 36, MicroStrain SG-Link Wireless Strain Node (SG-Link, 2010)

This device, known as the SG-Link, features internal bridge completion for a 350 ohm strain gage or higher and an internal, rechargeable 250 mAh lithium ion battery. It can stream data at rates up to 4 kHz and can handle accelerations up to 500 g. The drawback of this device is that it has only one data channel, and the starter kit, which includes the strain node, a base station, and the software, costs approximately \$2,145.00.

The system chosen for use in the custom force transducer was the XBee XB24-DKS development kit manufactured by Digi International. This is a module-based RF platform that can support single data access points or much larger meshed networks consisting of multiple transmitters. Figure 37 displays two XBee modules with different antennae options.



Figure 37, XBee Modules (Xbee, 2008)

The XBee modules also operate at 2.4 GHz and can support RF data rates up to 250 kbps. Additionally, they utilize IEEE 802.15.4 open communication architecture. Within the confines of a building or other urban environment, the range of the device is 30 m, or outdoors (line-of-sight) the range is 100 m. A single module features six 10-bit ADC

inputs and 8 digital inputs. It requires a 2.8 to 3.4 Vdc power supply, and the transmitting current draw is 45 mA. The full data sheet on this device can be found in Appendix C.

One of primary reasons the XBee platform was selected was its impressive capability coupled with such a low cost. An XBee starter kit was purchased for only \$129.00. However, it was found that along with a wide range of capabilities can come difficulty in customizing the XBee system to perform very basic tasks, such as the transmission of only one or two analog signals.

Implementing Wireless Data Transmission

Upon receiving the XBee starter kit, the system was assembled and tested using the provided X-CTU software. The XBee transmitter was fed signals from a dummy modem that was also provided by Digi, and the receiver was connected to a PC via USB port. The range tests were successful, however it was immediately determined that the circuit board upon which the transmitter was mounted would be too large for the force transducer application. It also was not readily customizable for different power sources. A much smaller, alternative circuit board configuration was found through *ladyada.net*, a free open source electronics tutorial website, and its sister company, Adafruit Industries. Using the “Tweet-a-Watt” tutorial, which is a project that uses Xbee modules to monitor in-home power consumption, the smaller XBee transmitter board was constructed and then ports were activated using the X-CTU software. Figure 38 displays one of these smaller boards. This setup also allows for a standard 5 V power source to be connected

directly to the board. The pin diagram for this board and the XBee module can be found in Appendix D.



Figure 38, XBee Adapter Board (Tweet, 2010)

The standard receiver board that came with the XBee starter kit was still utilized and was mounted in a custom box. This is pictured in Figure 39.



Figure 39, XBee Receiver with USB Connector

The Tweet-a-Watt tutorial was also used to learn about simple tasks such as transmitting single analog signals and the code necessary for communicating with the USB receiver. The tutorial helped develop code that was meant to run on a Windows XP

machine. The code was modified and written in Python so it could run on a stand-alone MacBook for data recording purposes. The XBee communication code written for this application can be found in Appendix E. The system was initially tested by simultaneously sending two known voltage signals wirelessly to the data recording computer. The system performed well, which allowed for the development of the remaining electronics, including the power source and the sensing circuits, to proceed.

Power and Sensing

As with the axial force measurement system, the custom force transducer was designed to sense force using strain gages. The gages selected for measuring torque were the Vishay Micro-Measurements CEA-06-187UV-350 general purpose torsion gages. These have a grid resistance of 350 ohms and a gage factor of $2.065 \pm 0.5\%$. The gages selected for measuring traversing and side forces were the Vishay Micro-Measurements WK-06-250PD-10C general purpose bending gages. These gages have a grid resistance of 1000 ohms and a gage factor of $2.05 \pm 1.0\%$. If axial force is also sensed with the transducer, the same C2A-06-250LW-350 gage will be used as in the axial force measurement system. The type and number of strain gages used in the application is important because it determines, along with the XBee module and any operational amplifiers, the power consumption of the device. With the selected gages, the current demand upon implementation of all force measurements was expected to be approximately 100 mA. This value was used to aid in the selection of batteries.

Batteries to power the force transducer were selected based on the following requirements:

- 1) *Lightweight*
- 2) *Compact*
- 3) *Rechargeable*
- 4) *Allow for a minimum of 2 hours continuous run time*

These requirements were met with the Thunder Power ProLite V2 rechargeable lithium polymer batteries. These are small (1.6" x 0.8" x 0.6") and lightweight (0.8 oz) batteries that are typically used in remote controlled helicopters or airplanes. They have a capacity of 250 mAh and can deliver up to a 5 amp continuous current or bursts up to 10 amps. Because these are 3-cell batteries that have to be carefully balanced during charging, the Thunder Power TP-610C charger was selected for use along with them. This charger can charge, balance, discharge, and cycle batteries and is pictured in Figure 40 along with a ProLite V2 battery.



Figure 40, ProLite V2 Battery and Thunder Power Charger

The charger also required a 12 V power supply that could deliver up to 10 amps. A Pyramid PS-12KX power supply was selected for this duty. The batteries take only approximately 20-30 minutes to charge on average and output approximately 12.6 volts when fully charged. The batteries can also be safely used down to 9.6 V, and if the pack voltage drops below this, the TP-610C charger has a recovery function that can safely and slowly recover the pack voltage to above 9.6 V.

With the strain gages and batteries selected for the force transducer, the circuit shown in Figure 41 could be designed. This circuit is housed within the electronics box.

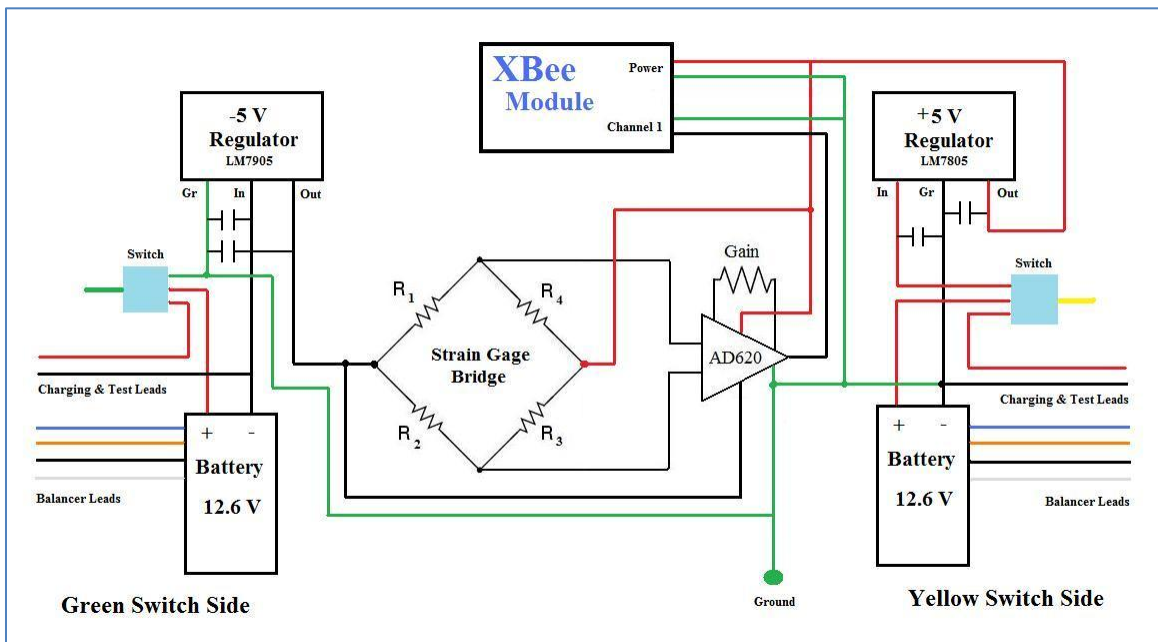


Figure 41, Wireless Force Transducer Circuit Diagram

The circuit shown features one strain gage bridge that is used for torque measurement currently, but is expandable to include the measurement of other forces. Two batteries

were used along with two voltage regulators to create a balanced ± 5 volt power source for both the strain gage bridge and the AD620 instrumentation amplifier. The XBee module is powered with +5 volts. The output of the strain gage bridge feeds into the AD620, which is a popular, low-cost, low-power operational amplifier. It can accept a wide power supply range, from ± 2.3 V to ± 18 V, and it requires only one external resistor to set gains from 1 to 1000. During the calibration stage, which will be discussed in a latter section, the gain was set to 970 with a 51 ohm resistor.

There is a switch on each side of the circuit that can switch its corresponding battery from OFF to RUN to CHARGE. Battery leads are made available through mini banana plug jacks at the sides of the custom electronics box. The design and construction of this box, along with the other mechanical components of the force transducer will be discussed in the following section.

Mechanical Design

Taper and Elastic Element

Several design concepts were considered for the taper and elastic element portions of the force transducer. Initially, the design plan involved purchasing a stock mill holder with a NMTB 50 taper and designing the elastic element to adapt to this holder, with either set screws or a collet. This would allow the force transducer to be quickly and easily removed from the machine if necessary. The disadvantage of this design however is twofold. The overall length of such a design would greatly restrict the working envelope of the FSW tool head, and there also exists the potential for problems with run-

out, as there would be an additional joint between the taper and the force transducer. It was decided therefore that the elastic element would be designed with an integral taper. This would reduce or eliminate the previously mentioned disadvantages.

The design of the elastic element itself also had to be considered. The job of the elastic element is to bear the FSW process loads and to be flexible enough for strain gages to measure the loads. Blignault et al. (2008) designed an elastic element with an annular, or hollow, cross-section. Their justification for this design was that it increased sensitivity, especially in the torsional measurement direction, while maintaining the level of strength of a solid member with a smaller diameter. Their design loads consisted of a 60,000 N axial force, an 8,000 N horizontal force, and a 400 Nm torque. They claim that for the final design, which was machined from a chromium-nickel-moly (BS 970 817 M40 – EN24) alloy steel, the elastic element is subjected to a stress that is 35% of the yield strength of the material (Blignault et al., 2008).

In the design of the elastic member for VUWAL’s force transducer, two cross sections were considered at the design loads listed in Table 8.

Table 8, Elastic Member Design Loads

Direction	Load
Axial Force, Fz	75,000 N
Torque, T	250 Nm
Traversing Force, Fx	7,500 N
Side Force, Fy	7,500 N

Instead of one horizontal load being applied as in the Blignault study, both a traversing force and a side force of 7,500 N are applied, which is equivalent to a 10,607 N resultant

load in the horizontal direction. It should be noted that these forces are much greater than what is typically experienced in the friction stir welding of aluminum. The cross sections considered were a solid, circular cross section and an annular, or hollow, cross section. These are pictured in Figure 42 below.

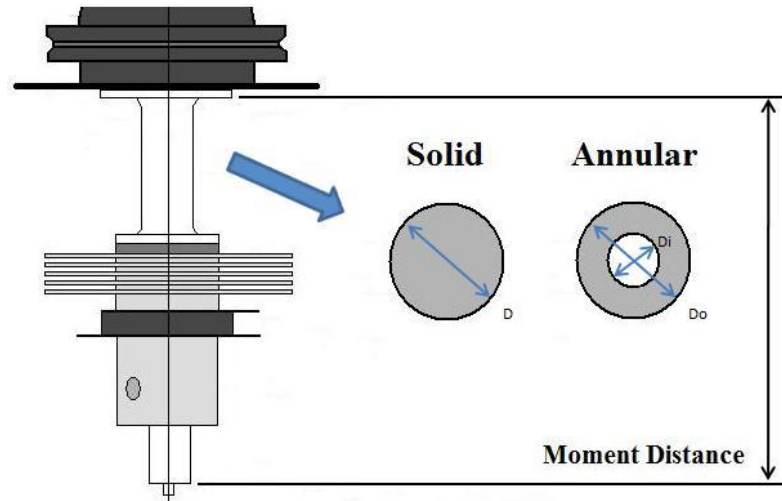


Figure 42, Elastic Element Cross Sections

Strength calculations were performed with the final material in mind. The elastic element and taper were to be made from 4140 steel hardened to 50 Rockwell C. Using standard hardness conversion charts, this is conservatively equivalent to a 475 Brinell Hardness Number (BHN), from which the approximate yield stress can be calculated using the following equation:

$$S_y(\text{psi}) = 525 * (\text{BHN}) - 30,000$$

This results in a predicted final yield stress of 219 ksi or 1510 MPa. Preliminary dimensions for the lengths of the elastic member and the heat sink were selected so that the maximum bending moment could be accurately calculated. Strength calculations

were performed assuming a compound loading of all forces on the shoulder of the tool, and then the dimensions of the outer diameter of the solid cross section and both the inner and outer diameters of the annular cross section were modified until a safety factor (SF) of approximately four was obtained for each. A SF of four was selected because for most general mechanical applications, the minimum acceptable SF is three (Juvinal, 2006). After calculating the principle stresses, two different theories were used to calculate the SF. The Von Mises Theory, or Distortion Energy Theory, is based on the energy required to change a material's shape. The Tresca Theory, or Maximum Shear Stress Theory, is slightly more conservative and uses a comparison of the maximum shear stress and the shear yield stress to predict material failure (Juvinal, 2006).

Strains in the compressive, shear, and bending directions were calculated, along with the resulting sensitivity based on a standard gage factor of 2.18 for each. The lateral deflection at the tool shoulder was also calculated, assuming all deflection arises from bending in the elastic element and not in the heat sink, chuck, or tool. A full tabulated version of the elastic element strength calculations can be found in Appendix F. Several observations can be made from the results.

- 1) The solid cross section, with a diameter of 41.4 mm, and the annular cross section, with an outer diameter of 43.9 mm and an inner diameter of 25.4 mm, were deemed to have equal strength based on a SF of 4.027 Von Mises and 4.022 Tresca for each.*
- 2) The Tresca formulation for SF is indeed more conservative than Von Mises*
- 3) The highest strain sensitivity is found in bending, followed by compression, and then shear. This confirms a finding of Blignault et al. (2008).*
- 4) The annular cross section has a slightly higher compressive sensitivity, while the solid cross section has a slightly higher sensitivity in both shear and bending.*

5) The annular cross section has a slightly lower lateral deflection than the solid cross section. Both are less than 0.5 mm.

Based on these results, the annular cross section was selected. An elastic element with this cross section was deemed to result in less lateral deflection at the tool shoulder yet have nearly equal to or greater sensitivity for measurement. The outer diameter and inner diameter were specified to be 43.94 mm (1.73 in) and 25.4 mm (1 in) respectively. This results in a wall thickness of 9.27 mm (0.36 in). The length of the elastic element was specified to be 63.5 mm (2.5 in) and is based largely on the required space for mounting strain gages.

With the specifications for the elastic element determined, a 3D Pro E model was developed for its design, including an integral NMTB 50 taper and provisions for mounting the heat sink and the electronics box. Figures 43 and 44 display screenshots of this model.



Figure 43, Screenshot of Force Transducer Model



Figure 44, Screenshot of Force Transducer Model

The model is displayed with the heat sink and the tool chuck attached. Complete engineering drawings were developed from this model for use during the machining process. These can be found in Appendix G.

Heat Sink

The purpose of the heat sink is to protect the strain gages from the harsh temperature environment of FSW. The challenge was to design a heat sink that would transfer heat away from the shaft of the force transducer and not increase the rate of heat transfer axially in the vertical direction towards the strain gages. A heat sink was designed that features a 4140 steel core, which is the same material from which the

elastic element and taper are machined, and copper fins that encourage increased heat transfer in the radial direction only. Additionally, a thermal barrier was designed that could be placed between the heat sink and the elastic element, to be machined from G7 Glass-Silicone.

The force transducer as a whole features a modular design, which allows the heat sink and the thermal barrier to be used together, separately, or not at all, depending on the thermal loads that are to be experienced during a particular FSW experiment. These thermal loads can vary greatly and depend on the selected FSW parameters and whether or not either the tool or the material is to be pre-heated. Engineering drawings for the heat sink and the thermal barrier can also be found in Appendix G.

Electronics Box

The electronics box was designed to be mounted at the top of the elastic element, at the bottom of the taper. With this configuration, strain gage lead wires are easily fed into the box and the box does not interfere with the deflection of the elastic element in any way. The design had to meet the following additional requirements:

- 1) Two exterior slots to house switches and banana plugs*
- 2) Two interior battery holders*
- 3) Internal slots to hold a minimum of four breadboards*
- 4) Space above and below breadboard mounts for wire routing*
- 5) Air vents for cooling electronics*
- 6) A lid that is removable and seals out lubricating oil*

Based on these requirements, a box was designed and a dimensionally accurate 3D model was developed in AutoDesk Inventor. The interior view of this model is displayed in Figure 45.

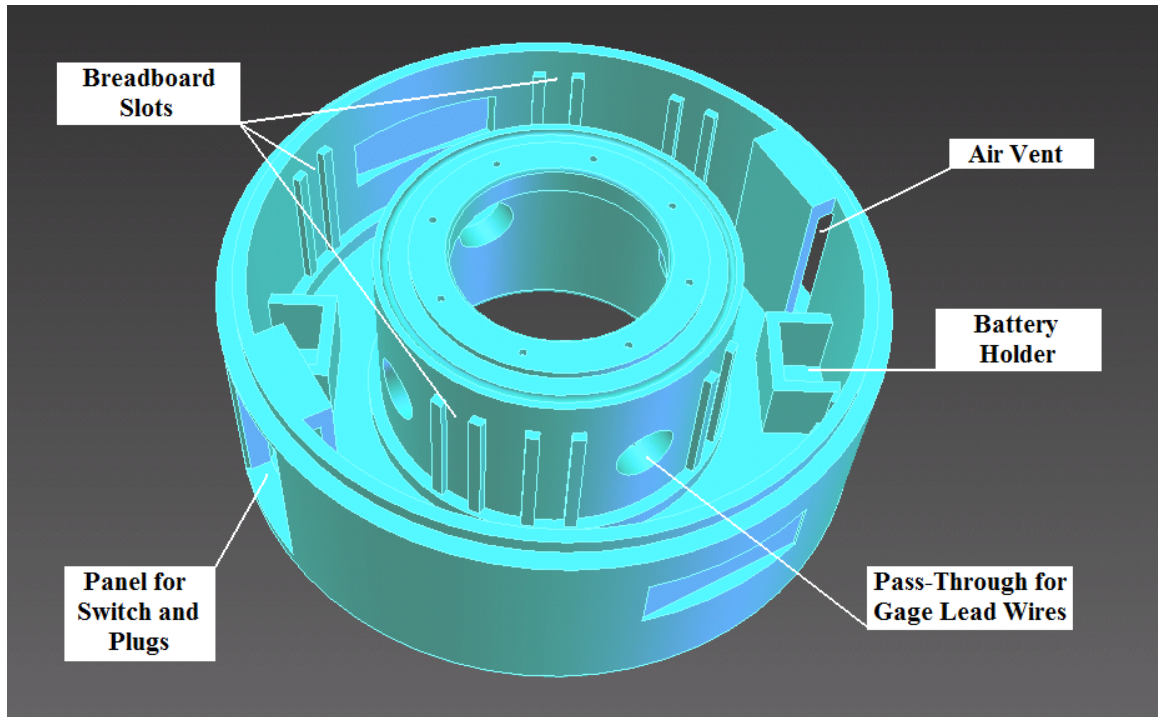


Figure 45, Interior View of Electronics Box Model

All of the interior features are arranged so that there is an identical feature 180° from it. This was done intentionally for balancing purposes. To seal out lubricating oil from the machine spindle, two design features were added. There is a cut-out designed to hold an o-ring at the top of the box where the lid makes contact, and at the outer edge of the box, the lid overlaps the walls so any oil will shed away without entering the joint line. A screenshot of the box with the lid attached is shown in Figure 46. The dimensions of the

lid were specified so that it would be held in place with a slight press fit. Additionally, the flange between the elastic member and the taper slightly overlaps the top of the lid so that it is securely held down.

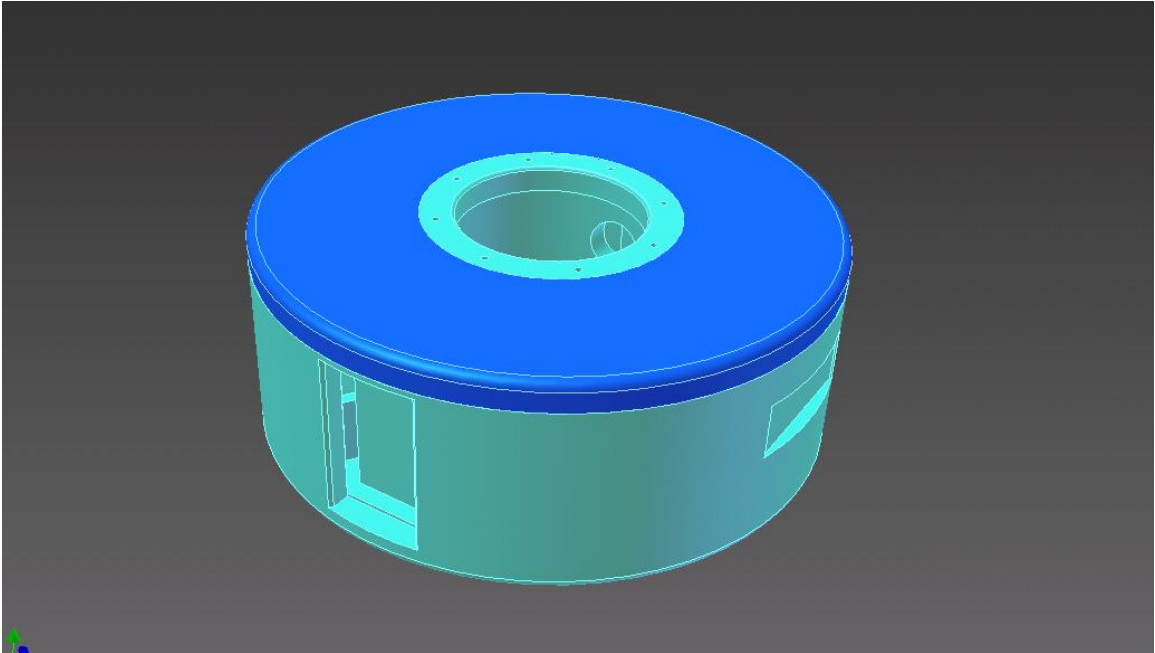


Figure 46, Electronics Box Model with Lid

The dimensional accuracy of this model was highly important because the box was to be made with a rapid prototyper using the Inventor .Stl files generated directly from the model. The rapid prototyping of this box, along with the machining of the other hardware components will be discussed further in the next section.

Implementation and Calibration

Construction

The elastic element and taper were machined by the Vanderbilt University Physics Machine Shop from 4140 steel and then hardened to 50 Rockwell C by Paulo Products of Nashville, TN. After hardening, the outer surface of the elastic element was polished to prepare it to accept strain gages. Figure 47 displays the elastic element and taper at this stage.



Figure 47, Elastic Element and Taper

A full bridge of torsional strain gages were then mounted to the surface in a back-to-back configuration for measuring torque. The heat sink and the thermal barrier were also machined by the VU Physics machine shop. They are both pictured in Figure 48. The

heat sink has 4 radial fins made from 1/8" copper sheet that are press fit to the steel core. Small rings of aluminum were also press fit to the core in order to set the proper spacing between the fins.



Figure 48, Heat Sink and Thermal Barrier

The electronics box was rapid prototyped at Vanderbilt University using a Dimension BST 1200 machine. This machine rapid prototypes parts by building up layers of ABS plastic, one at a time. The layer thickness is adjustable from 0.010" to 0.013", and the resolution in the x and y horizontal directions is ± 0.003 ". The working volume of the prototyper head is an 8" x 8" box that is 12" tall. The 3D Inventor model of the electronics box was used to generate a .Stl file, from which the prototyper generates its program for building the part. The finished electronics box is displayed in Figure 48. It took 47 hours of machine time to prototype. The lid was also prototyped using this machine, taking approximately 5 hours to build.



Figure 49, Electronics Box after Prototyping

Heat Sink Testing

In order to test the effectiveness of the heat sink at protecting the strain gages, an experiment was conducted in which the temperature of the elastic element was monitored over the course of a typical research welding sequence. There were also concerns over the strength of the thermal barrier, which was machined from G7 Glass-Silicone. This material has adequate compressive strength for the application, but it seemed as if it could be prone to brittle fracture. It was desired to see the temperature response if the thermal barrier was not used, so only the heat sink was installed for this set of experiments.

An infrared thermal camera was used to monitor the average temperature over a selected region of the elastic element. Thermal images and temperature data were

captured and recorded every minute over the course of the two hour experiment. Figure 50 displays the region of observation.

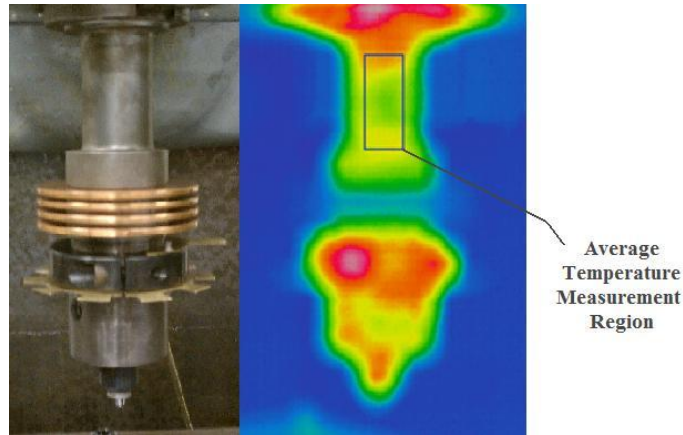


Figure 50, Temperature Measurement Region

Figure 51 displays the temperature data for this welding research sequence.

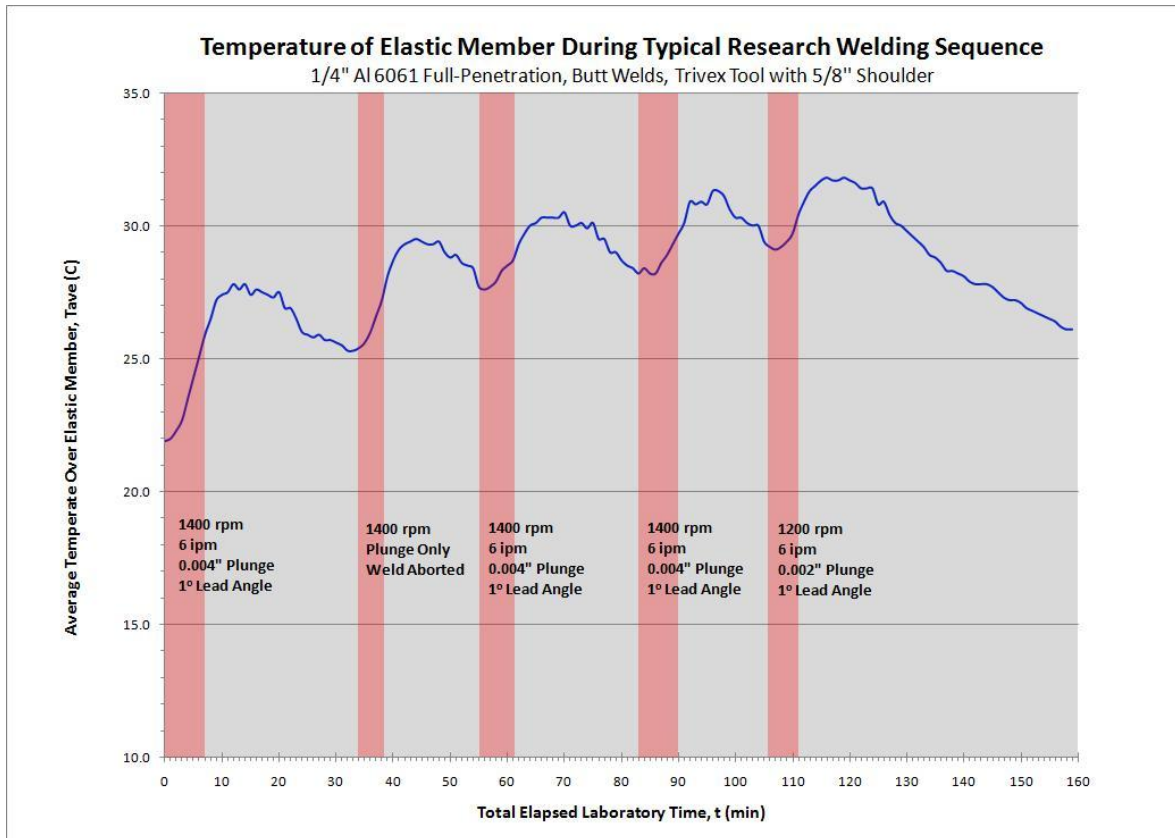


Figure 51, Temperature Data for Heat Sink Test

In the figure, the vertical bars indicate the periods in which the particular welds were performed. These were full-penetration aluminum butt welds done with a trivex tool. The welding parameters are indicated for each weld in Figure 51. It is interesting to observe that the temperature of the elastic element continues to increase after a weld is completed due to heat conducting up the shaft of the device.

At the end of the five weld sequence, the temperature of the elastic element had increased from 22° C to only 32° C. This result was encouraging because most strain gages can withstand up to at least 120° C. The torsional strain gages selected for measuring torque can withstand up to 175° C. Of course, it is desired to keep the temperature of the gages well below these limits due to the fact that temperature changes also lead to resistance changes and can affect force measurement data. The configuration of the torsional gages also happens to be temperature compensated however, so even the modest temperature increase experienced should not greatly affect torque measurement. Additionally, it was determined that the use of the thermal barrier would not be necessary for limiting heat transfer in most cases.

Circuit Building and Testing

The circuit displayed in Figure 41 was built within the electronics box using the breadboard slots and battery holders as intended. Figure 52 shows the interior of the box with the electronics completely installed, including the strain gages and lead wires, which run from the elastic element to the interior of the box. The circuit was tested using a dummy load cell that was built from a cantilever beam with a single strain gage installed

at the point of maximum bending stress. This testing confirmed that the circuit was operating as intended and the signal was being transmitted wirelessly to the receiver before the device was fully installed on the FSW milling machine.



Figure 52, Installation of Electronics

Balancing

The electronics box itself was designed to be balanced, but after the electronics, which are not completely symmetrical, were installed, the box had to be rebalanced before use on the FSW machine spindle. A balancing unit was designed and then built at the VU Physics Machine Shop. This device consists of a frame with two rails, upon which the force transducer can roll depending on its state of balance. The frame itself is first leveled using adjustable feet, and then two round adapter blocks are attached to the force transducer, one via the heat sink mounting holes and one via the draw bar mounting hole. Figures 53 and 54 display images of the balancing process using this device.

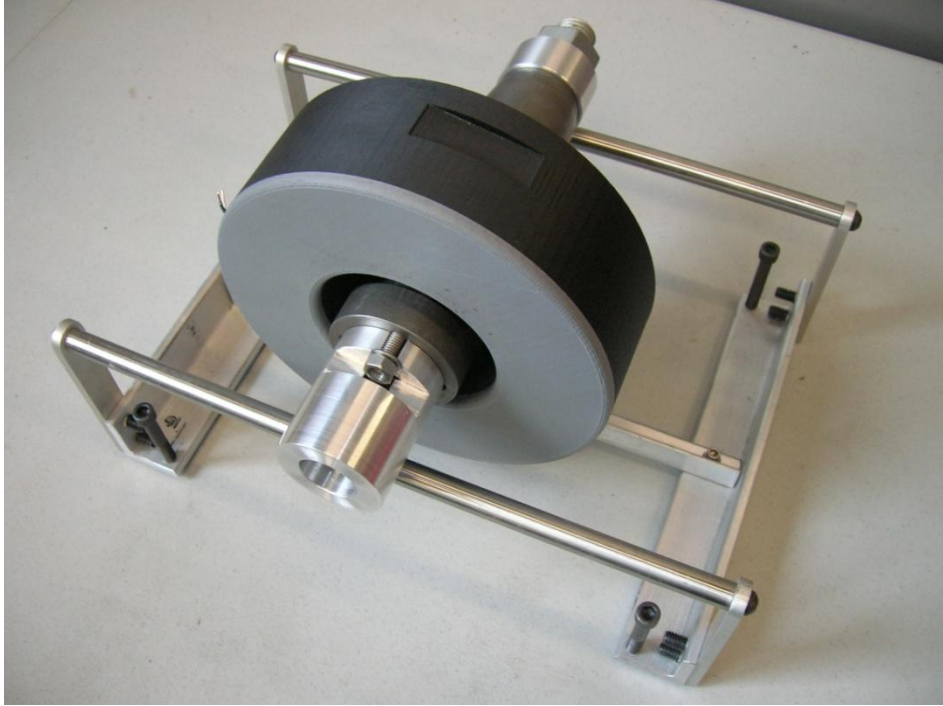


Figure 53, Force Transducer Balancing Process

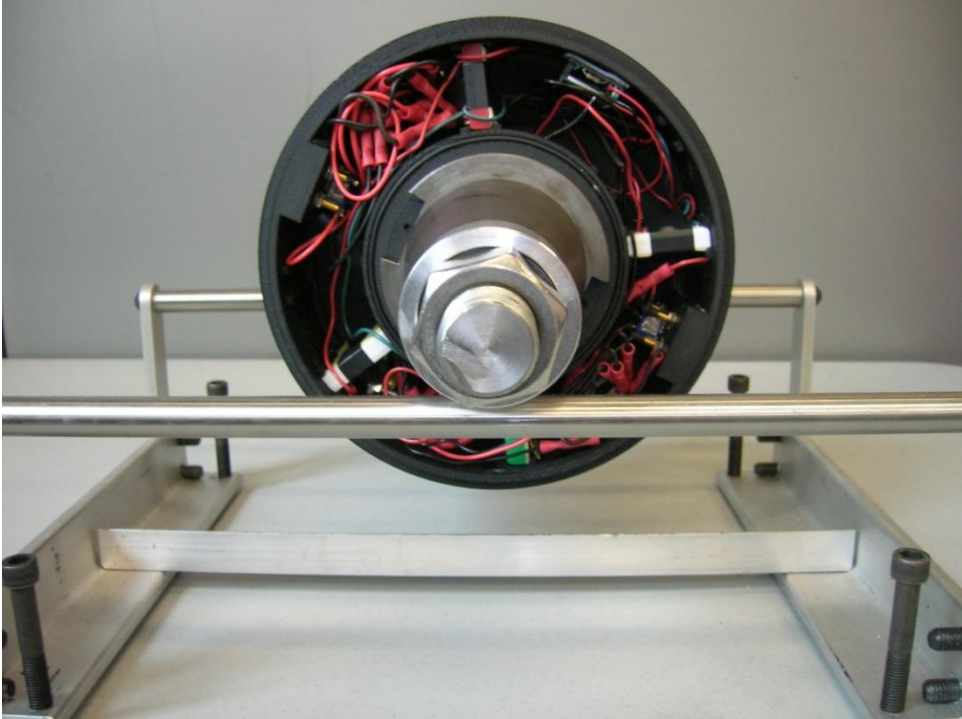


Figure 54, Force Transducer Balancing Process

The balancing process was performed with the lid uninstalled so that small weights could be installed on the interior of the electronics box until the force transducer reached a quasi-stable state or unstable equilibrium, meaning it would not roll on the rails unless disturbed. The assumption that the lid is balanced, which is valid, is inherent to this process.

Installation and Calibration

After balancing, the completed force transducer was installed on the FSW milling machine. Figures 55 and 56 display images of the force transducer just prior to installation.



Figure 55, Custom Force Transducer for FSW



Figure 56, Custom Force Transducer for FSW

In order to calibrate the device for torque measurement, an adapter tool into which a 3/8" hex-head bolt could be tightened was machined and installed into the chuck like a FSW tool. This allowed for a torque wrench to be used to put a known torque load on the spindle. The torque wrench used in the calibration was a Computorq 3 Model 2401C13, manufactured by CDI Torque Products. This is an electronic torque wrench that has a measurement range of 2.71 to 27.10 N-m. This measurement range closely matches the torques that are routinely seen in friction stir welds of aluminum at VUWAL. This is important because typically torque wrenches are less accurate below 20% of their measurement range, meaning that if a torque wrench of a larger, more common capacity was used, the calibration points would most likely fall in the less accurate range. This

particular torque wrench has an accuracy of $\pm 2\%$ from 20% to 100% of full scale, or 7.6 to 27.10 N-m. Below this range it has an accuracy of $\pm 3\%$. The torque wrench and adapter tool are shown in Figure 57.



Figure 57, Torque Wrench and Adapter Tool

The torque wrench also features audible tones and LEDs to inform the user when 90% of the desired torque is reached, when 100% of the desired torque is reached, and if the desired torque is exceeded. The wrench also displays the maximum torque experienced after any single load is applied. This was convenient for calibration purposes.

The torque calibration was performed by first establishing wireless communication and then applying torques of 5, 10, 15, 20, and 25 N-m in first the CW

and then the CCW directions. The actual, maximum torque reached at each interval was recorded, and these values were then matched to the corresponding peak voltages that were recorded. The raw voltage data along with the table of peak values can be found in Appendix H. Figure 58 displays the calibration curve resulting from the compiled torque and voltage data.

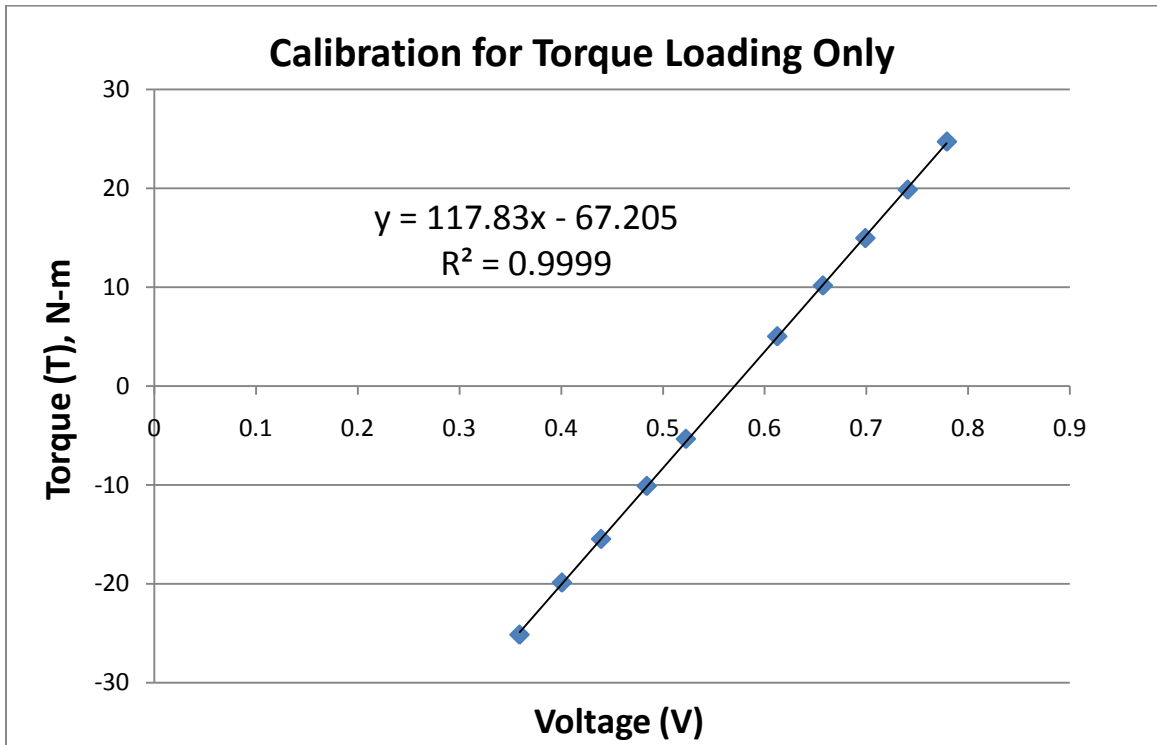


Figure 58, Torque Calibration Curve

The calibration was highly linear and the signal to noise ratio documented in the raw data file in Appendix H was also impressive. The calibration also marked the end of the first stage of development for the force transducer. The system is completely implemented for one force measurement and is readily upgradable to measure additional forces and temperature.

Cost

Although only one force measurement is implemented, the cost of the force transducer can be documented and discussed. Only minor costs will be incurred to upgrade the transducer to measure additional force and temperature. This will involve the purchase of relatively inexpensive components such as strain gages, op amps, or thermocouples. The total cost of the custom force transducer is outlined in Table 9.

Table 9, Cost of Custom Force Transducer

Item	Description	Qty	Cost
Materials			
Wireless Kit	Digi International, XBee, XB24-DKS	1	\$129.00
Adapter Kit	Adafruit XBee Adapter Kit, v1.1, 126	1	\$10.00
Batteries	Thunder Power ProLite V2, 250 mAh, TP250-3SJPL2	2	\$33.98
Charger	Thunder Power, TP-610C	1	\$99.95
Power Supply	Pyramid, PS-12KX, 13.8 Vdc, 10 Amp	1	\$49.65
Strain Gages	Vishay Micro Meas. CEA-06-187UV-350	2	\$31.36
Materials	3.5" 4140 Steel Rod, 1/8" Copper Sheet		\$184.05
Miscellaneous	Switches, Plugs, Wire, Op Amps, Regulators		\$100.00
Total:			\$637.99
Labor and Services			
Machining	40 Hours, VU Physics Shop		\$1,600.00
Hardening	Paulo Products, Nashville, TN		\$68.00
Prototyping	Electronics Box, Acu-Cast Technologies Quote		\$1,270.02
Total:			\$2,938.02
Total Cost:			\$3,576.01

The data in this table is meant to reflect the entire cost of the project, as if it had to be completed again from start to finish, and not necessarily the actual direct cost to

VUWAL. For instance, the cost of rapid prototyping the electronics box was obtained via instant quotation from Acu-Cast Technologies, LLC for their stereolithography process. In reality, the rapid prototyping was completed in-house and the cost was covered by VU Mechanical Engineering departmental funds. The total direct cost to VUWAL for the project was \$2,305.99. A large majority of this was from the machining process, which totaled approximately \$1,600.00. The total cost of materials was only \$637.99.

Even considering the total overall cost of the project at \$3,576.01, this is still over 40% less than the lowest priced multi-axial load cell listed in Table 2. It is only 15% of the cost of a LowStir FSW system.

Demonstration of Measurement

The force transducer has been in use at VUWAL now for approximately one month. Multiple test welds were completed upon installation and calibration. Figure 59 displays torque data from one of these tests. This particular test was a 1/4" full penetration aluminum butt weld performed with a trivex tool with a 0.625" shoulder. The welding parameters were selected as 800 rpm, 3 ipm, 0.004" plunge, and a 1° lead angle. Torque was recorded successfully for this test, as expected. There were some concerns about cross-talk from the traversing and side forces in the torque reading. This would appear as an oscillating signal that is added to the torque reading. There may be some signs of this in Figure 59. There are no concerns however over axial force cross talk in the torque reading because this was tested extensively during the torque calibration. A

series of increasing axial loads were put on the spindle while the torque signal voltage was being recorded.

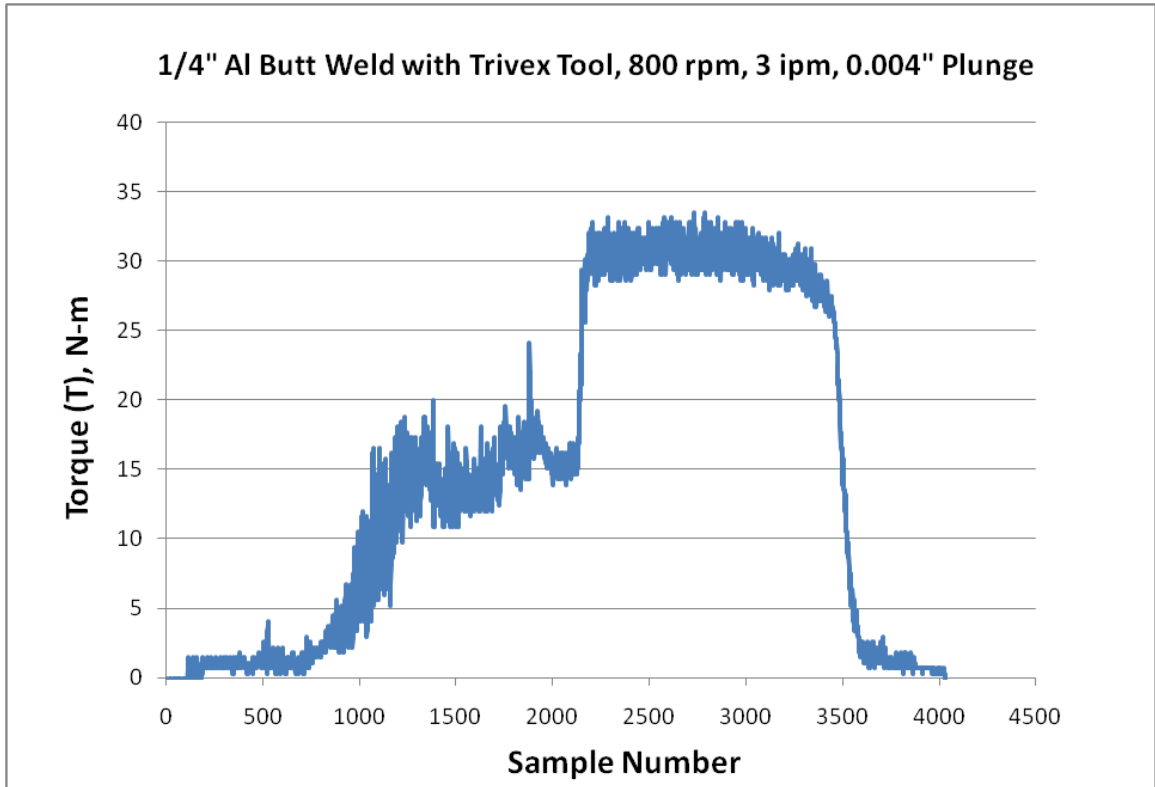


Figure 59, Torque Measurement Test Weld

No measurable trends were detected in the torque reading during this experiment. This was expected however because for an axial loading, all of the torsional strain gages experience the same strain and therefore no differential voltage would be created in the bridge. Quantifying and correcting for any crosstalk from the traversing and side forces will be addressed when these forces can be measured in real time.

CHAPTER IV

FUTURE WORK

Measurement of Traversing and Side Forces

The capabilities of the custom force transducer will be expanded to include the measurement of traversing and side forces. This will be accomplished by measuring the bending load created by these forces and then resolving the oscillating signal into fixed directions by using position encoders on the rotating spindle. This method was used successfully by Mitchell (2002), utilizing a stationary Hall effect sensor and two magnets set 90° apart that rotated with the spindle.

A similar method was also used with the Kistler dynamometer that had previously been in operation at VUWAL. This dynamometer measured x and y forces relative to its rotating chassis. These forces had to be resolved into traversing and side forces that were relative to the fixed machine anvil. This was accomplished using a custom incremental encoder consisting of a reference sensor and an angle sensor, both Omron EE-SX672A optical sensors. This setup is pictured in Figure 60. The digital output of the sensors was read by the NI USB-6008 data acquisition device, and the forces were resolved in real time using custom C# code operating on the dynamometer computer. Both the interrupter ring on the tool chuck and the optical sensor mounting bracket have been preserved and will be reused with the new custom force transducer. Once the capabilities of the force transducer are upgraded, the force resolving code will be adapted so that this task can be performed in real time on the welding control computer.

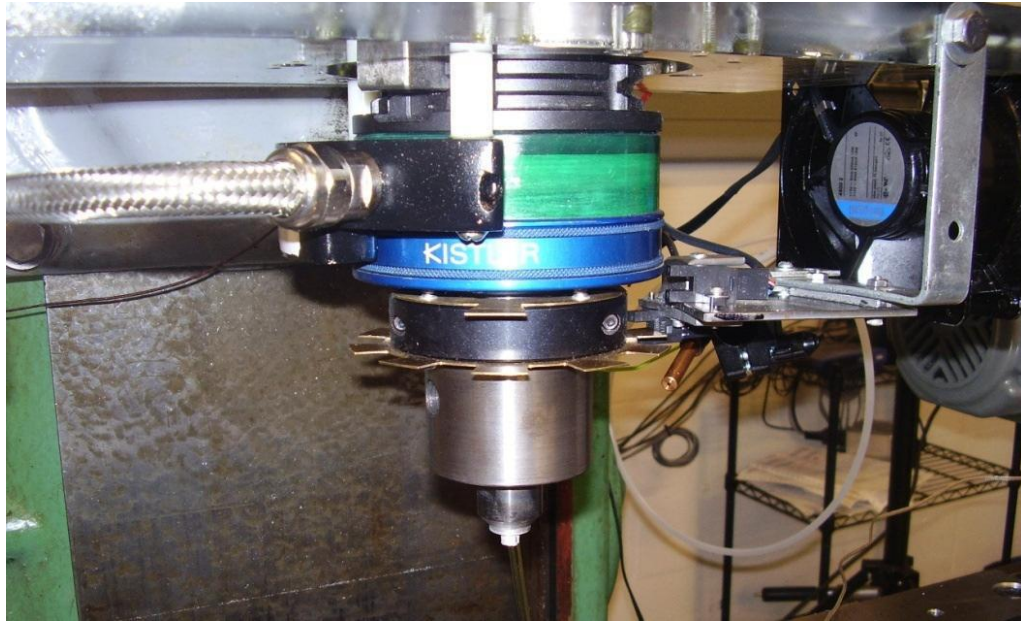


Figure 60, Encoder Setup for Resolving X and Y Forces

With the measurement of traversing and side forces comes the ability to quantify and compensate for any cross talk resulting from these forces in real time. There were concerns over this in both the axial force measurement of Chapter II and the torque measurement in Chapter III. These cross talk relationships will most likely be nonlinear, as pictured in Figure 61. Blignault et al. (2008) addressed these relationships in two ways, first by using third order compensation equations where possible, and then using a novel compensation algorithm where necessary.

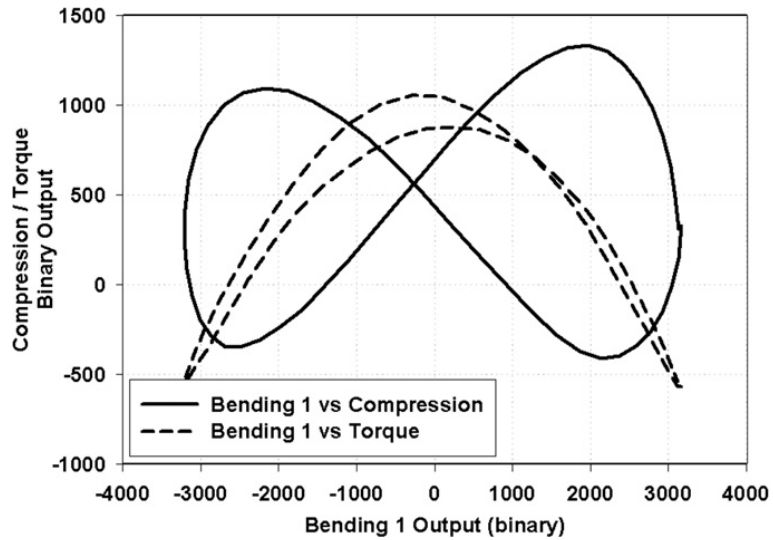


Figure 61, Nonlinear Crosstalk Relationships (Blignault et al., 2008)

Temperature Measurement

The capabilities of the force transducer will also be upgraded so that tool temperature as well as the temperature of the elastic element can be measured in real time. The temperature of the elastic element will be measured in order to monitor the thermal environment around the strain gages and possibly even compensate for temperature induced voltage changes in the force measurement bridges. Measuring tool temperature will involve designing a special tool that has a thermocouple imbedded in the shoulder or probe and has a means for routing wire upwards through the tool shank, through the chuck, and into the electronics box. This will allow for real time temperature measurement along the weld seam, which will open up the possibility for temperature control research to be conducted.

CHAPTER V

CONCLUSIONS

Measuring, modeling, and controlling FSW process forces are important aspects of both research and industrial applications in this field. Forces can lend insight into weld quality, resulting mechanical properties, and even tool wear. When force control is implemented, the applicability of FSW is greatly increased and weld characteristics can even be controlled. Through-the-tool tracking techniques have also been implemented using force feedback signals.

There are four main forces that are of interest in FSW. These are the axial force (F_z), the traversing force (F_x), the side force (F_y), and the torque (M_z or T), although typically the forces of highest interest are the axial force and the torque. There are a variety of commercially available load cells that can be used in FSW or are designed specifically for use in FSW. These were summarized in Table 2. The multi-axial load cells range in price from approximately \$6,000 to \$39,000. It was desired to build a custom, low-cost force measurement system for use at VUWAL that would replace a Kistler 9123CQ01 rotating cutting-force dynamometer.

Axial force measurement was implemented by instrumenting the FSW milling machine head with strain gages. A proof-of-concept experiment was first conducted to determine the feasibility of this method, and a FEA analysis was also conducted to confirm the proof-of-concept measurements, to determine if traversing and side forces could be measured in this way, and to examine the cross talk among the forces. It was

found that axial cross talk interference was relatively low at approximately 4%, but that axial force dominates the deflections of the head and therefore it was the only measurement that could easily be attained in this way. A custom data acquisition system was designed and constructed, and the axial force data was made available to the weld controller PC via NI USB-6008 device. Both auto-zero and force data logging were demonstrated with this system. The cost to VUWAL for the newly implemented axial force measurement system was \$343.94. This is lower than even the least expensive load cell in Table 2. This method of measuring robot link deflections with a low-cost, custom system may be an attractive alternative for many in both academia and industry.

The other FSW process forces were to be measured using a custom, low-cost wireless force transducer, specifically designed to be used on FSW milling machine at VUWAL. An XBee wireless communication package that uses radio transmitter modules operating at 2.4 GHz was purchased and modified to meet the needs of this project. An elastic element with integral taper was designed and machined in-house, then instrumented with strain gages after hardening. A heat sink and thermal barrier were also designed and machined for use with this system, which works together in a modular fashion along with the tool chuck. An electronics box was designed and rapid prototyped from ABS plastic in-house as well. This resulted in a savings of approximately \$1,270 for VUWAL. The electronics box, which holds components such as the XBee transmitter, batteries, and op amps, sends the force data from the rotating machine spindle to a stationary monitoring computer with a USB interfaced XBee receiver. The system was assembled, calibrated, and used to demonstrate the measurement of torque in FSW which completed the first stage of development for this project. The system is readily

upgradable to measure additional forces and temperature. The total cost of this custom wireless force transducer was \$3,576.01, including the \$1,270.02 estimate for having the electronics box rapid prototyped by an outside vendor. The total direct cost to VUWAL was \$2,305.99. The majority of this cost resulted from machining, which was done at the VU Physics Machine Shop and totaled approximately \$1,600.00. The total cost of parts was only \$637.99.

The total cost considered however, this force transducer was built at a cost that is over 40% less than the lowest priced multi-axial load cell listed in Table 2. The cost to build this force transducer was also only 15% the price of the LowStir FSW system, which is advertised as a low cost alternative itself. It is also a system that was designed to be used regularly in the research setting and has proven to withstand the mechanical and thermal loads of FSW.

Future work will involve expanding the capabilities of the force transducer to include measurement of traversing and side forces as well as measurement of tool temperature, and this will also be completed at minimal cost. This will allow the issue of force crosstalk interference to be addressed further and expand the current research capabilities of VUWAL to include temperature control.

REFERENCES

- Blignault, C., Hattingh, D.G., Kruger, G.H., Van Niekerk, T.I., James, M.N. (2008), "Friction stir weld process evaluation by multi-axial transducer", *Measurement*, Vol. 41, pp. 32-43.
- Burton, K.A., Matlack, M.P., Bommer, H.L. (2009), "Friction stir welding load confirmation system", U.S. Patent No. US 7,571,654 B2.
- Cook, G.E., Crawford, R., Clark, D.E., Strauss, A.M. (2002), "Robotic friction stir welding", *Industrial Robot: An International Journal*, Vol. 31 No 1, pp. 55-63.
- Crawford, R., Cook, G.E., Strauss, A.M., Hartman, D.A., Stremler, M.A. (2006a), "Experimental defect analysis and force prediction simulation of high weld pitch friction stir welding", *Science and Technology of Welding and Joining*, Vol. 11, No. 6, pp. 657-665.
- Crawford, R., Cook, G.E., Strauss, A.M., Hartman, D.A. (2006b), "Modeling of friction stir welding for robotic implementation", *International Journal of Modeling, Identification, and Control*. Vol. 1, No. 2, pp. 101-106.
- Deyuan, Z., Yuntai, H., Dingchang, C. (1995), "On-line detection of tool breakages using telemetering of cutting forces in milling", *International Journal of Machine Tools Manufacturing*, Vol. 35, No. 1, pp. 19-27.
- Elangovan, K., Balasubramanian, V. (2008), "Influences of tool pin profile and welding speed on the formation of friction stir processing zone in AA2219 aluminum alloy", *Journal of Materials Processing Technology*, Vol. 200, pp. 163-75.
- Fleming, P.A., Hendricks, C.E., Wilkes, D.M., Cook, G.E., Strauss, A.M. (2009), "Automatic seam-tracking of friction stir welded T-joints", *International Journal of Advanced Manufacturing Technology*, Vol. 45, pp. 490-495.
- Fleming, P.A., Lammlein, D.H., Cook, G.E., Wilkes, D.M., Strauss, A.M., DeLapp, D., Hartman, D.A. (2008a), "Through the tool tracking for friction stir welding", US Patent filed May 30, 2008, Serial No. 12/130, 622.

- Fleming, P.A., Lammlein, D.H., Wilkes, D.M., Cook, G.E., Strauss, A.M., DeLapp, D.R., Hartman, D.A. (2008b), "Misalignment detection and enabling of seam tracking for friction stir welding", *Science and Technology of Welding and Joining*, Vol. 14, No. 1, pp. 93-96.
- Gere, J.M. (2004), *Mechanics of Materials*, 6th ed. Brooks/Cole – Thomson Learning, Belmont, California, USA, pp. 911-915.
- Hosein, A., Lin, D., Kovacevic, R. (2009), "Numerical and experimental investigations on the loads carried by the tool during friction stir welding", *Journal of Materials Engineering and Performance*. Vol. 18, No. 4, pp 339-350.
- Johnson, D. (2010), "Creating an affordable option for friction stir welding", *National Instruments Website*, <<http://sine.ni.com/cs/app/doc/p/id/cs-11860>>.
- Juvinall, R.C., Marshek, K.M. (2006), *Fundamentals of Machine Component Design*, 4th Ed. John Wiley & Sons, Hoboken, New Jersey, USA.
- Lammlein, D.H. (2010), "Friction stir welding of spheres, cylinders, and T-joints: Design, experiment, modeling, and analysis", Ph. D. Dissertation, Vanderbilt University.
- Lammlein, D.H., DeLapp, D.R., Fleming, P.A., Strauss, A.M., Cook, G.E. (2009), "The application of shoulderless conical tools in friction stir welding: An experimental and theoretical study", *Materials and Design*, Vol. 30, pp. 4012-4022.
- Longhurst, W.R. (2009), "Force Control of Friction Stir Welding", Ph. D. Dissertation, Vanderbilt University.
- Longhurst, W.R., Strauss, A.M., Cook, G.E., Cox, C.D., Hendricks, C.E., Gibson, B.T., Dawant, Y.S. (2010a), "Investigation of force controlled friction stir welding for manufacturing and automation", *Proceedings of the Institution of Mechanical Engineers, Part B: Journal of Engineering Manufacture*. Vol. 224, pp. 1-13.
- Longhurst, W.R., Strauss, A.M., Cook, G.E., Fleming, P.A. (2010b), "Torque control of friction stir welding for manufacturing and automation", *International Journal of Advanced Manufacturing Technology*, Vol. 51, pp. 905-913.

- Mishra, R.S., Ma, Z.Y. (2005), "Friction stir welding and processing", *Materials Science and Engineering*, Rep. No. 50, pp. 1-78.
- Mitchell, J.E. (2002), "The experimental thermo-mechanics of friction stir welding", M.S. Thesis, Vanderbilt University.
- Nandan, R., DebRoy, T., Bhadeshia, H.K.D.H. (2008), "Recent advancing in friction-stir-welding – Process, weldment structure and properties", *Progress in Materials Science*, Vol. 53, pp. 980-1023.
- Nunes, A.C., Bernstein, E.L., McClure, J.C. (2000), "A rotating plug model for friction stir welding", *81st American Welding Society Annual Convention*.
- Schneider, J., Beshears, R., Nunes, A.C. (2006), "Interfacial sticking and slipping in the friction stir welding process", *Materials Science and Engineering*, Vol. 435-436, pp. 297-304.
- Scialpi, A., De Filippis, L.A.C., Cavaliere, P. (2007), "Influence of shoulder geometry on microstructure and mechanical properties of friction stir welded 6082 aluminum alloy", *Materials and Design*, Vol. 28, pp. 1124-1129.
- SG-Link –mXRS Wireless Strain Node Datasheet (2010), *MicroStrain Website*, <http://www.microstrain.com/sg-link.aspx>.
- Smith, C. (2000), "Robotic friction stir welding using a standard industrial robot", *2nd Friction Stir Welding International Symposium*. Gothenburg, Sweden.
- Thomas, W.M., Nicholas, E.D., Needham, J.C., Church, M.G., Templesmith, P. and Dawes, C.J. (1991), International Patent Application no. PCT/GB92/02203 and GB Patent Application no. 9125978.9.
- Thomas, W.M., Johnson, K.I., Wiesner, C.S. (2003), "Friction stir welding – Recent developments in tool and process technologies", *Advanced Engineering Materials*, Vol. 5 No. 7, pp. 485-90.

Threadgill, P.L. (2007), "Terminology in friction stir welding", *Science and Technology of Welding and Joining*, Vol. 12 No 4, pp. 357-360.

Tweet-a-Watt Tutorial (2010), *Ladyada Website*, <<http://www.ladyada.net/make/tweetawatt/>>.

Ulysse, P. (2002), "Three-dimensional modeling of the friction stir-welding process", *International Journal of Machine Tools and Manufacture*, Vol. 42, pp. 1549-1557.

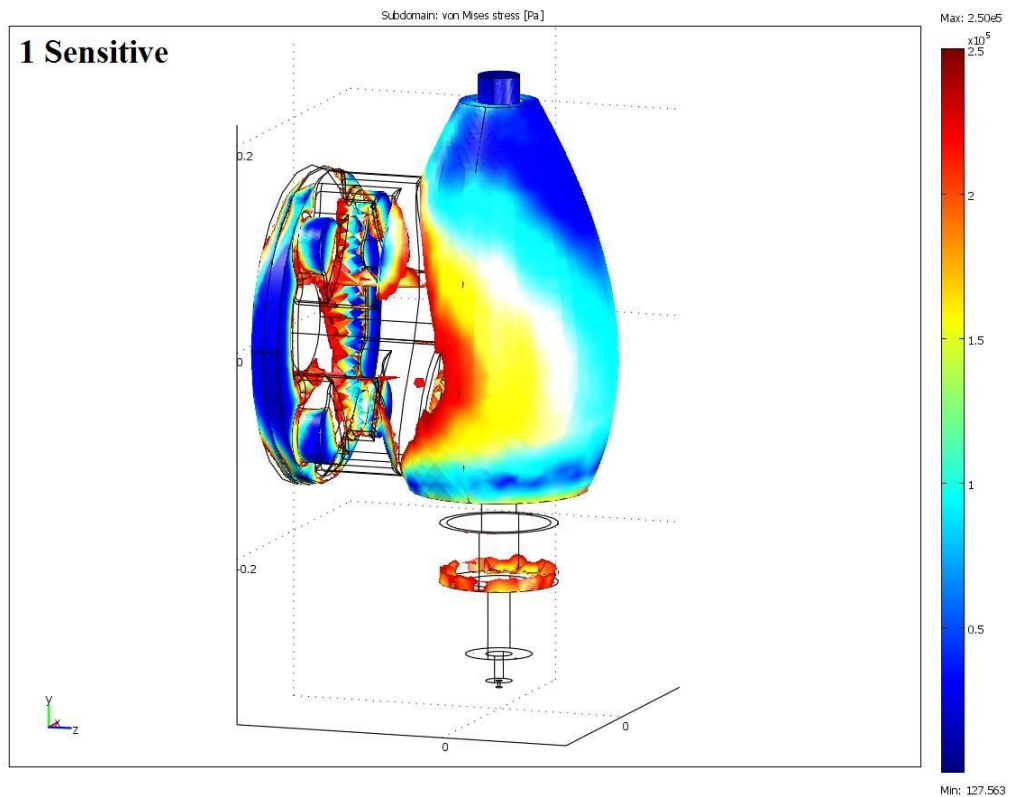
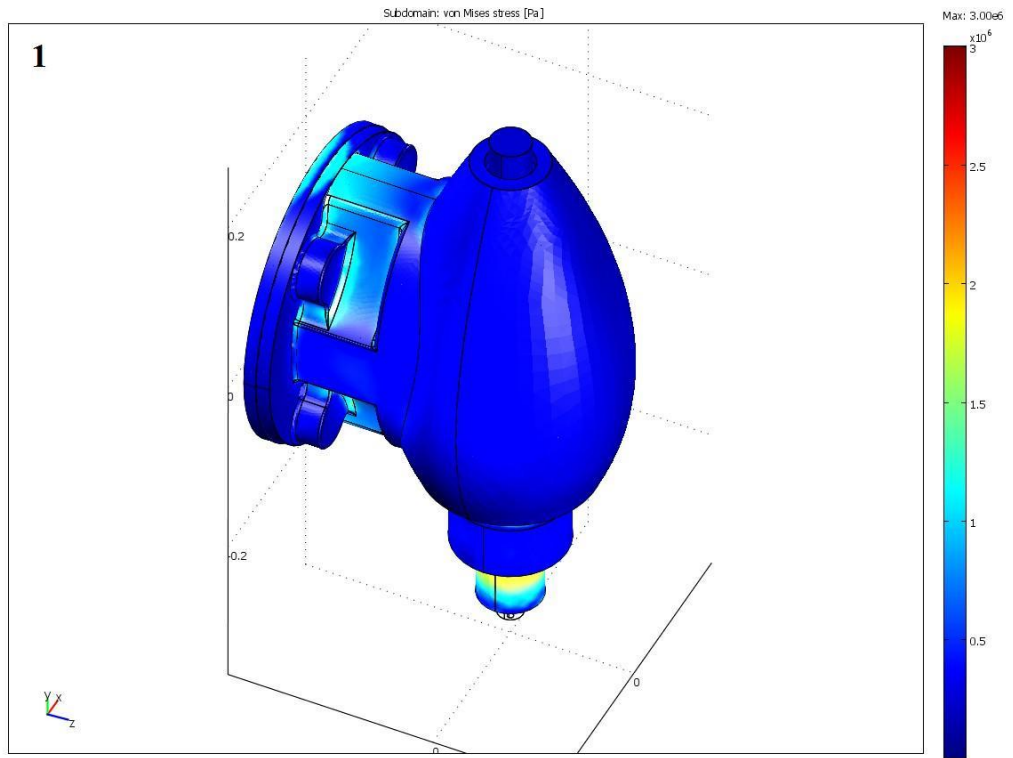
Universal Wireless RS232 to USB Transceiver Datasheet (2010), *Omega Website*, <<http://www.omega.com/DAS/pdf/WRS232.pdf>>.

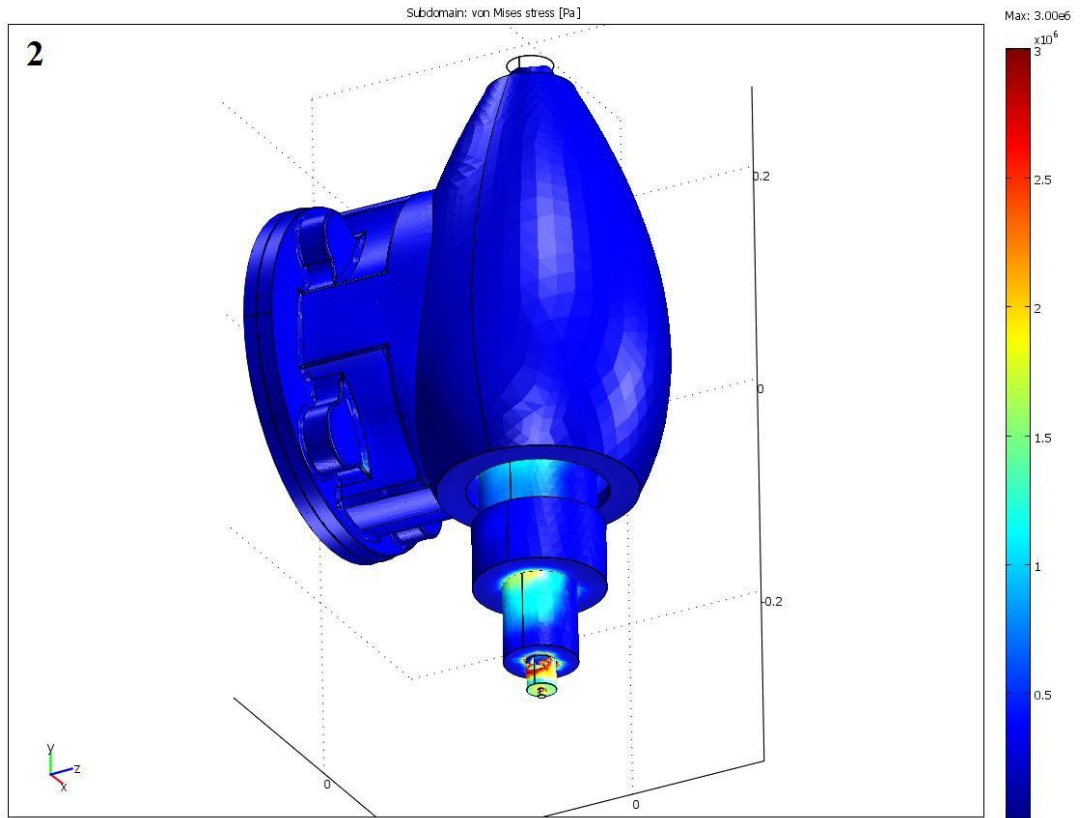
XBee Multipoint RF Modules Product Datasheet (2008), *Digi International, Inc.*, <http://www.digi.com/pdf/ds_xbeemultipointmodules.pdf>.

Zhao, Y.H., Lin, S.B., Qu, F.X., Wu, L. (2006), "Influence of pin geometry on material flow in friction stir welding process", *Materials Science and Technology*, Vol. 22 No. 5, pp. 45-50.

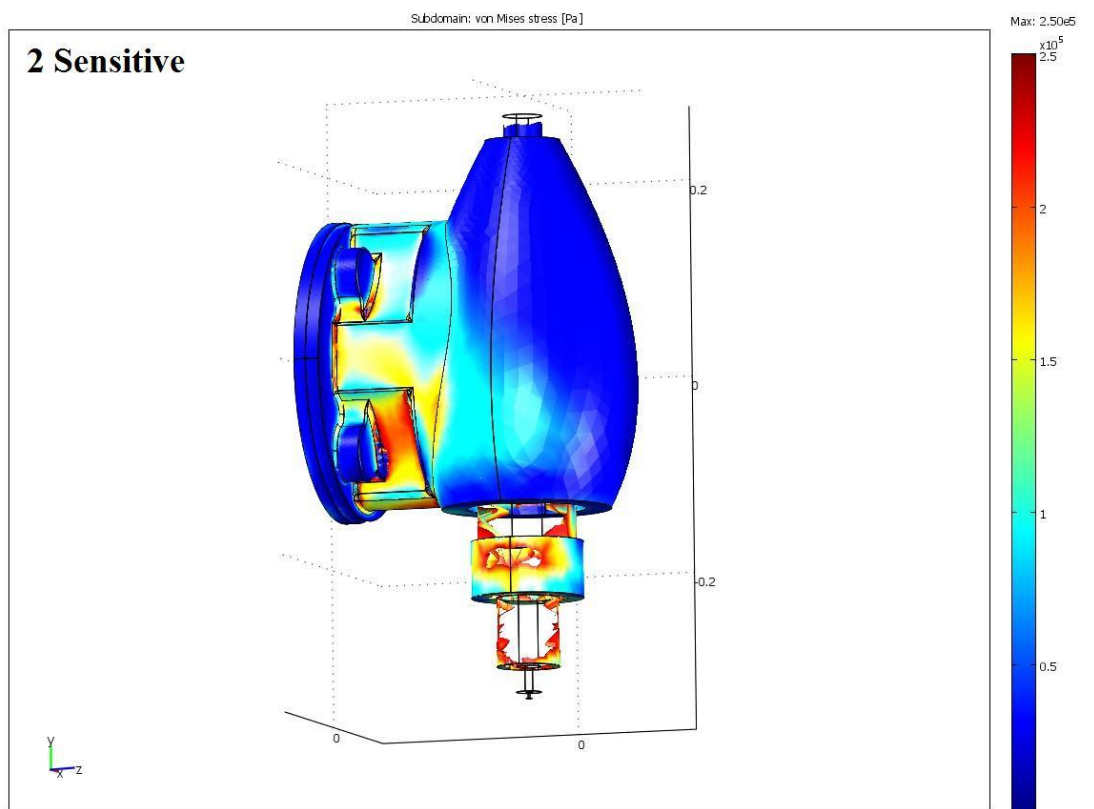
APPENDICES

APPENDIX A: FEA Simulation Results

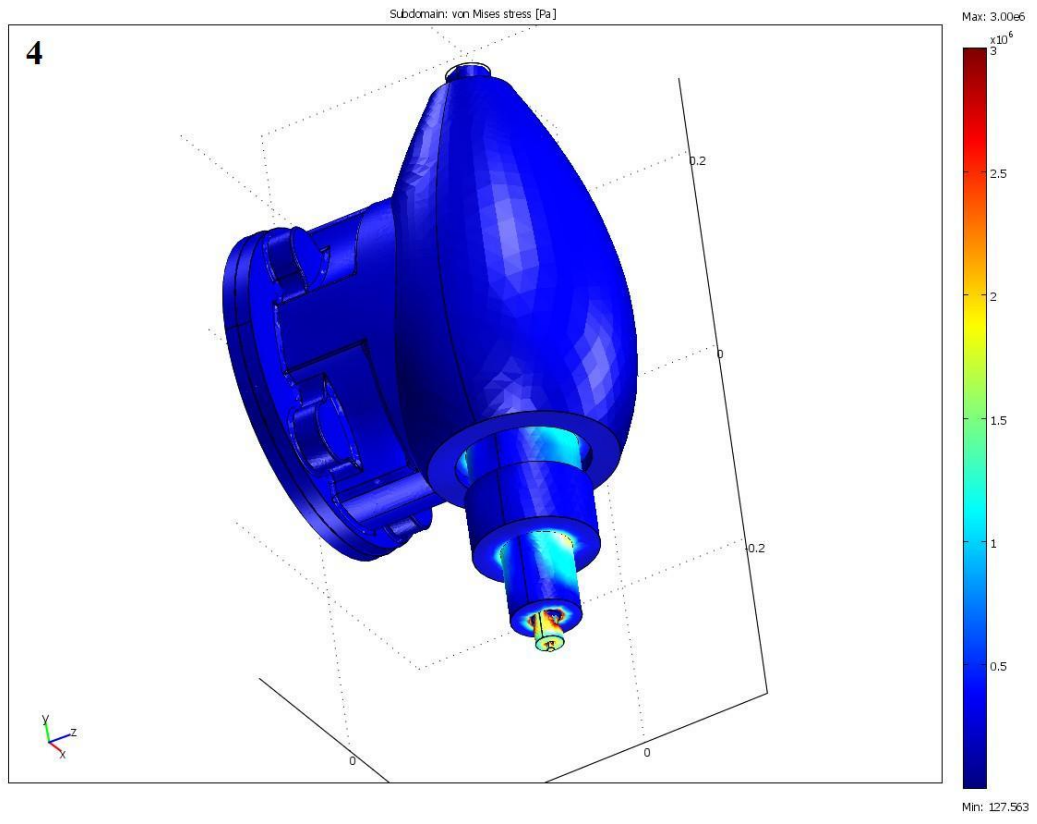
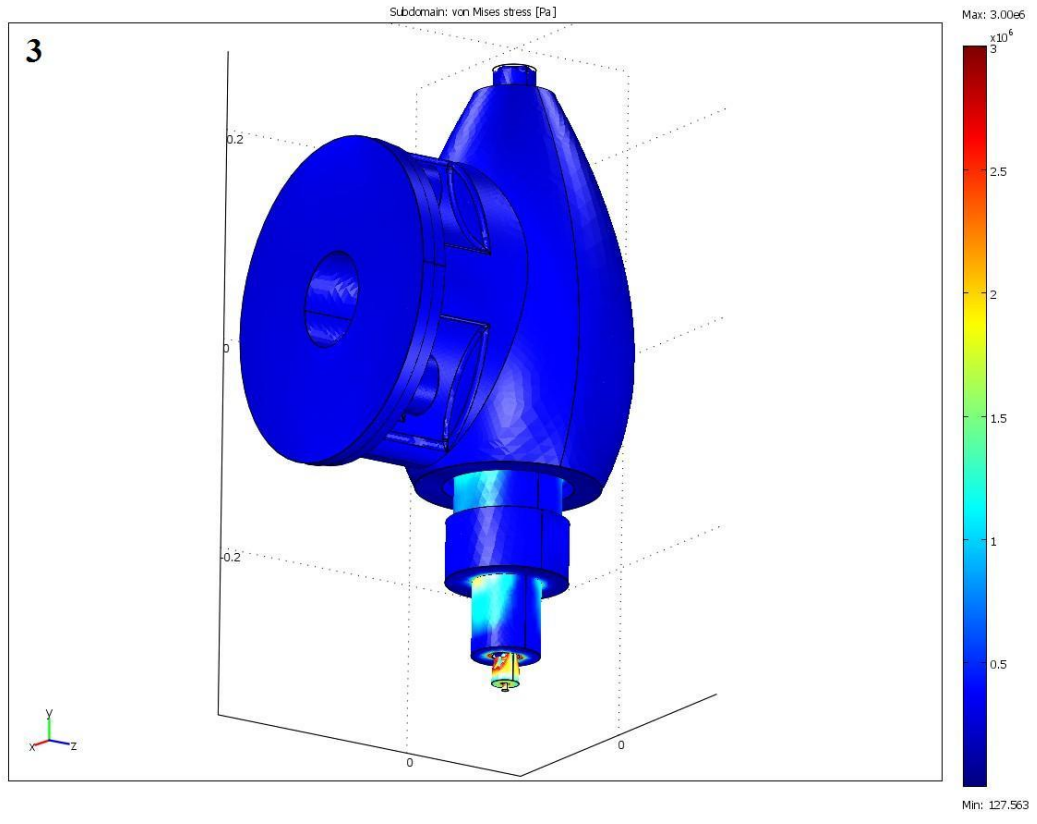


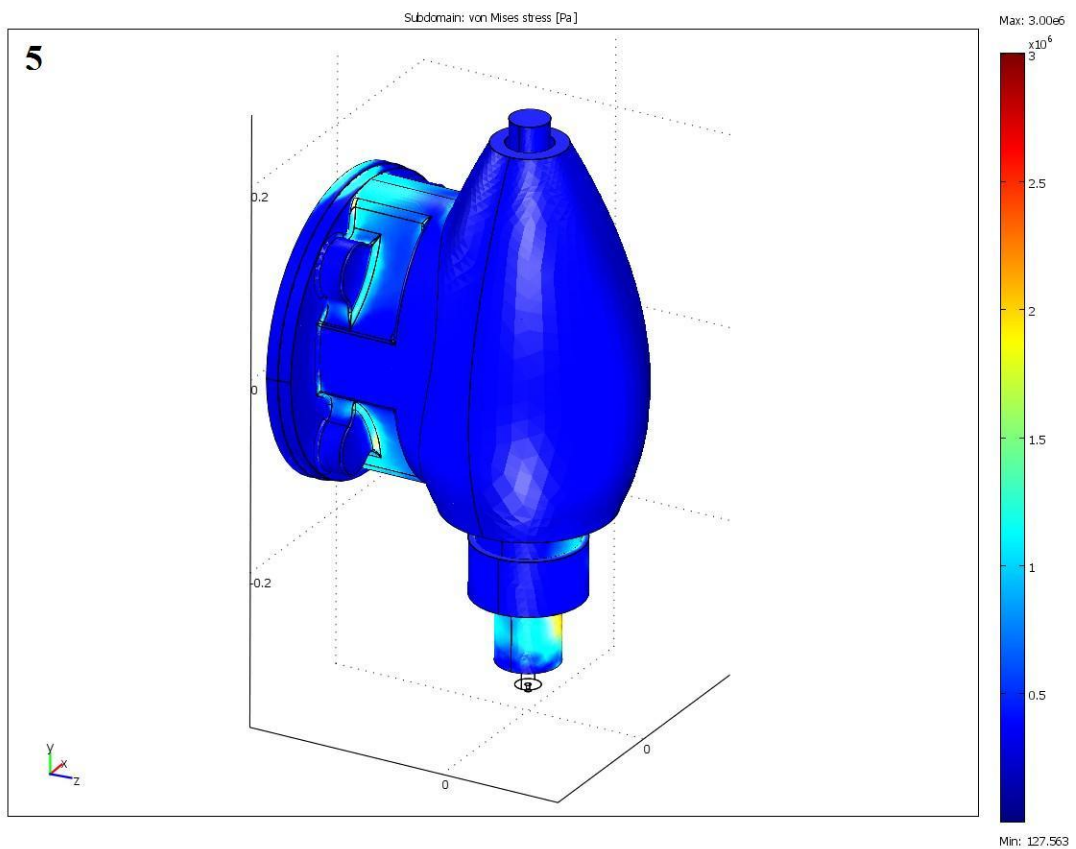
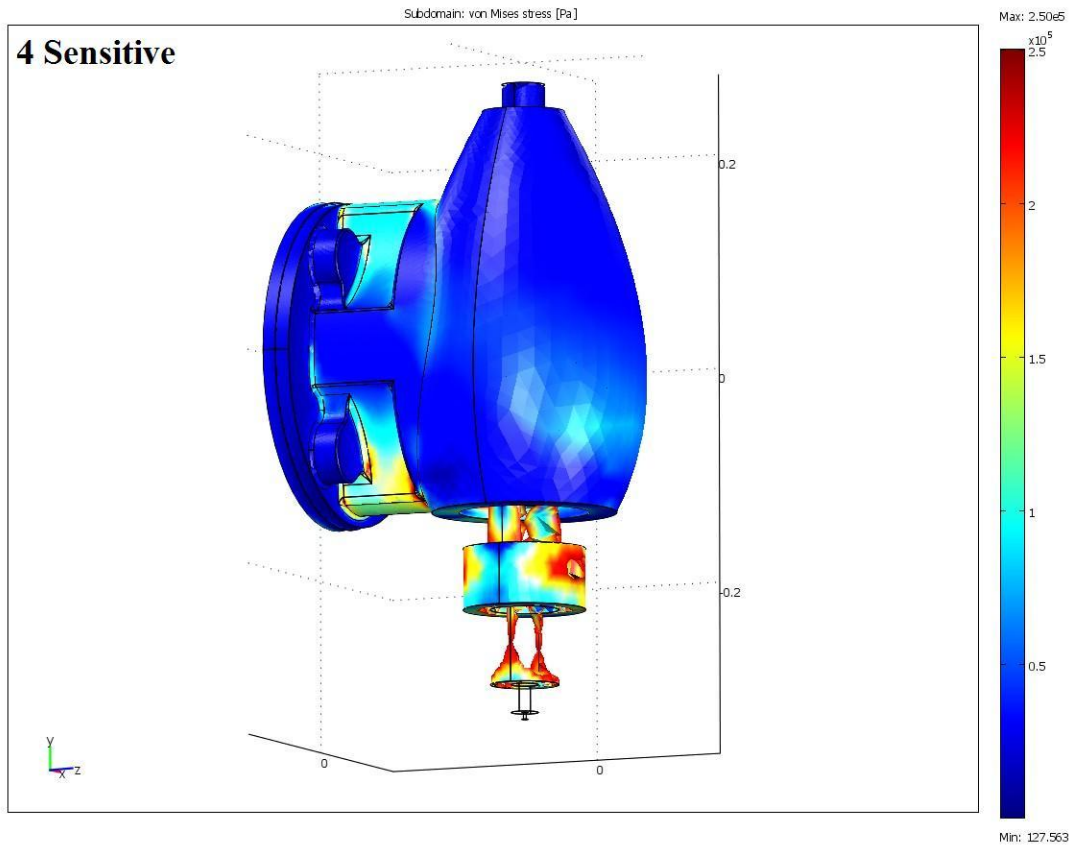


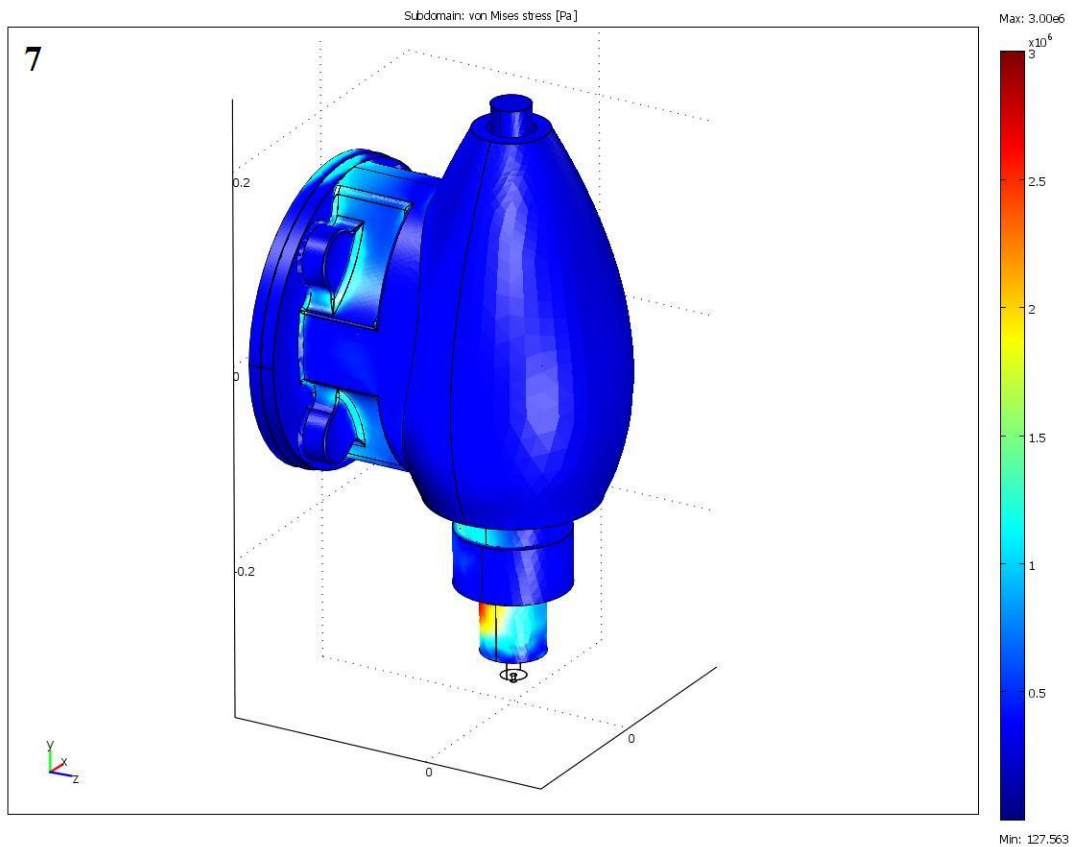
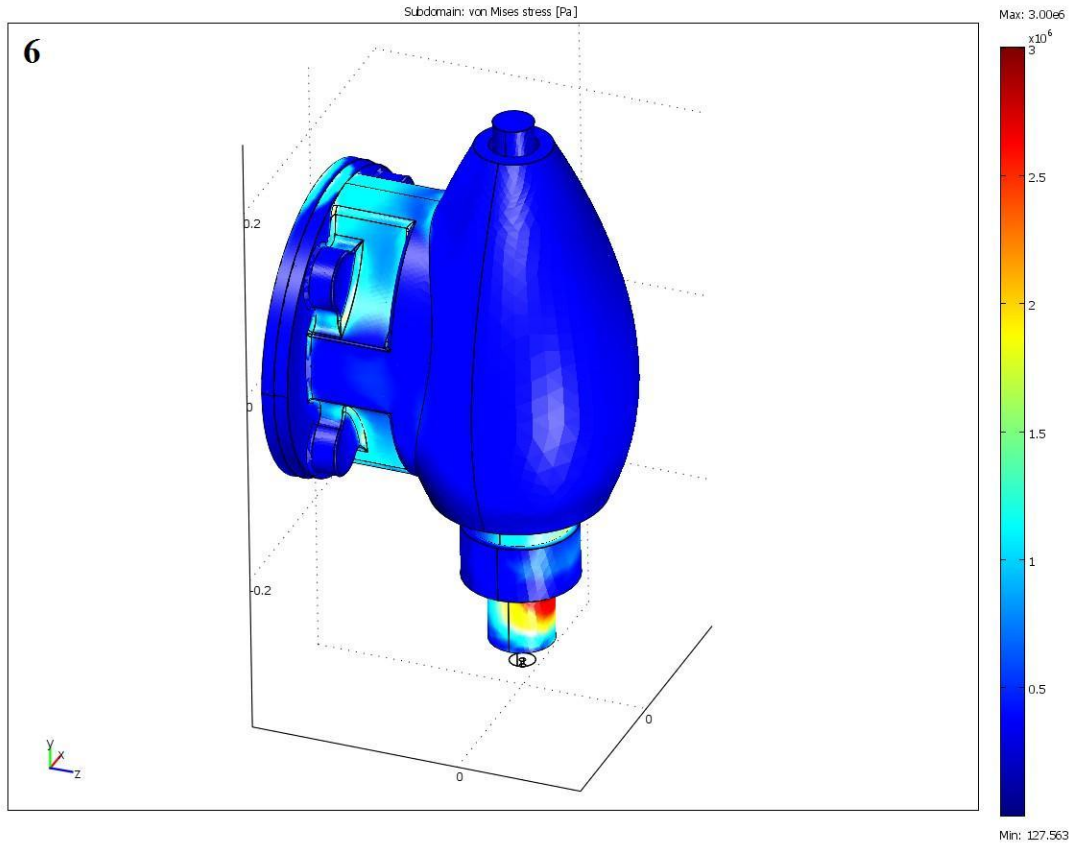
Min: 127.563

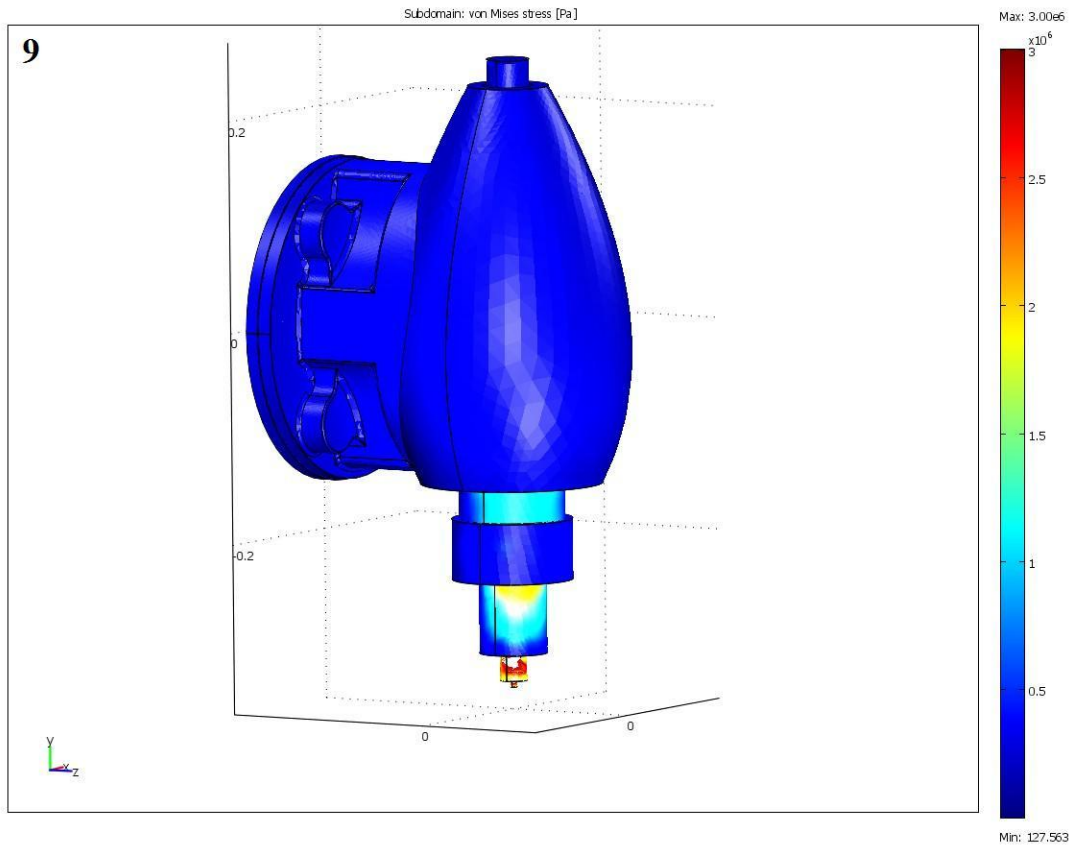
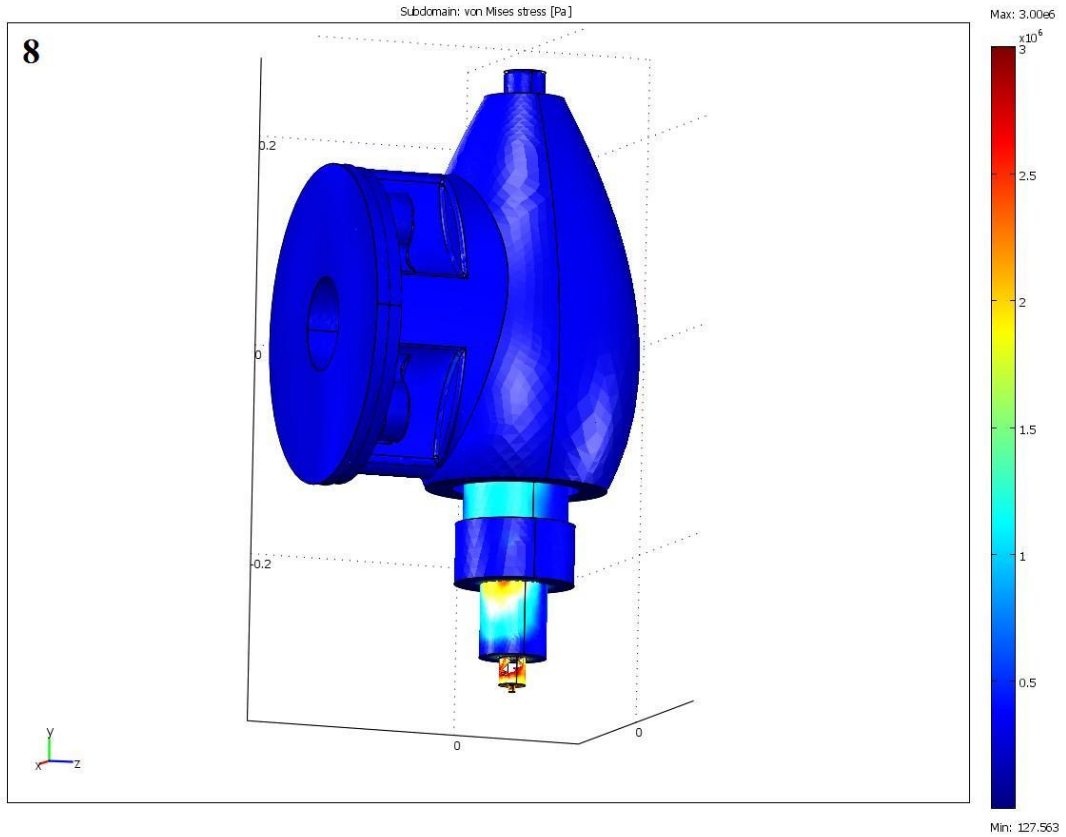


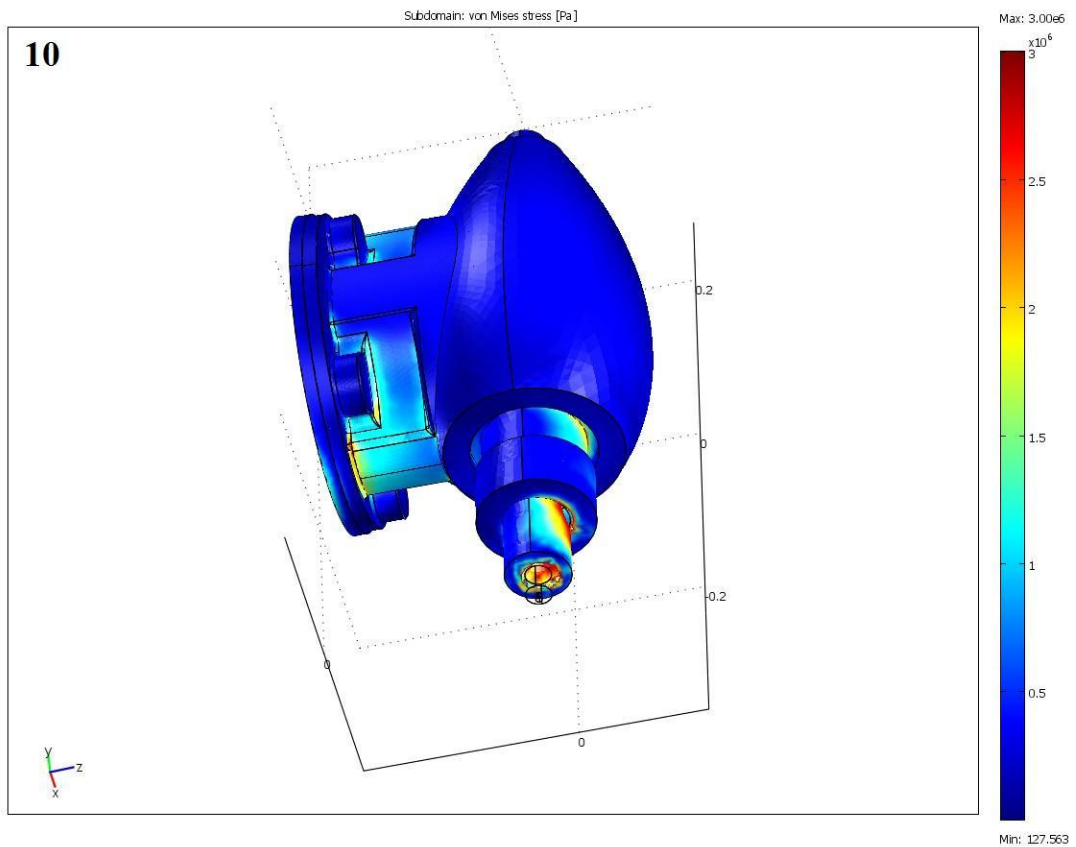
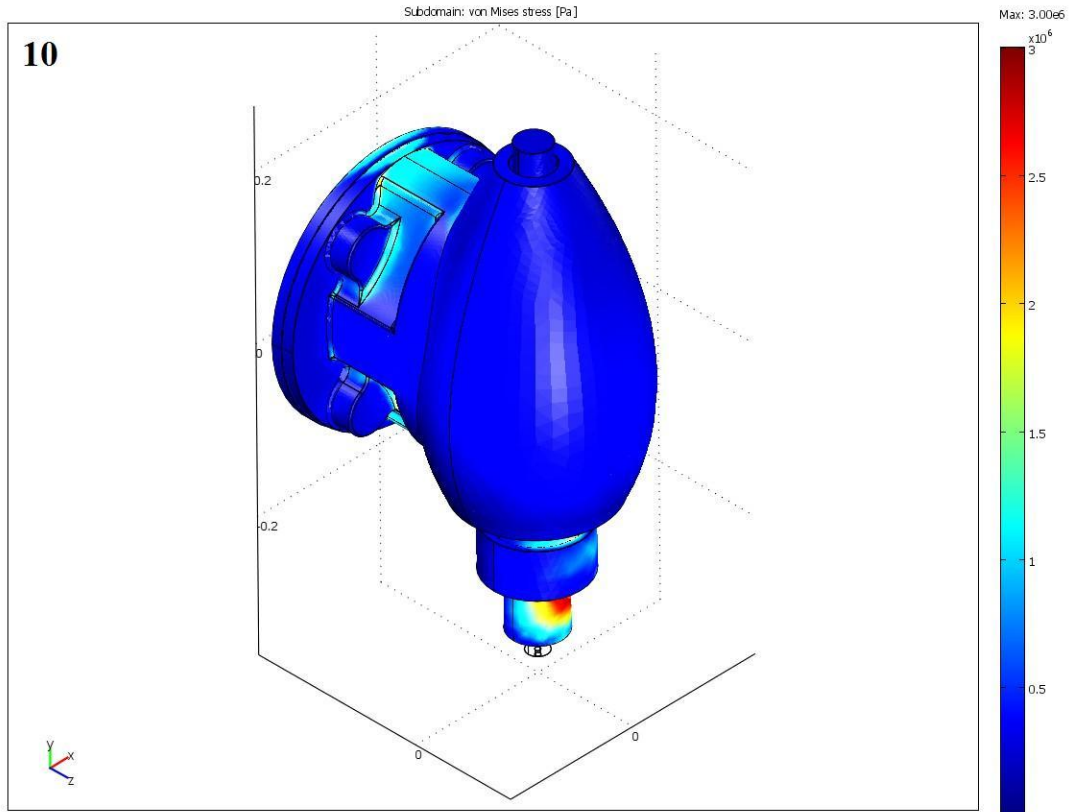
Min: 127.563

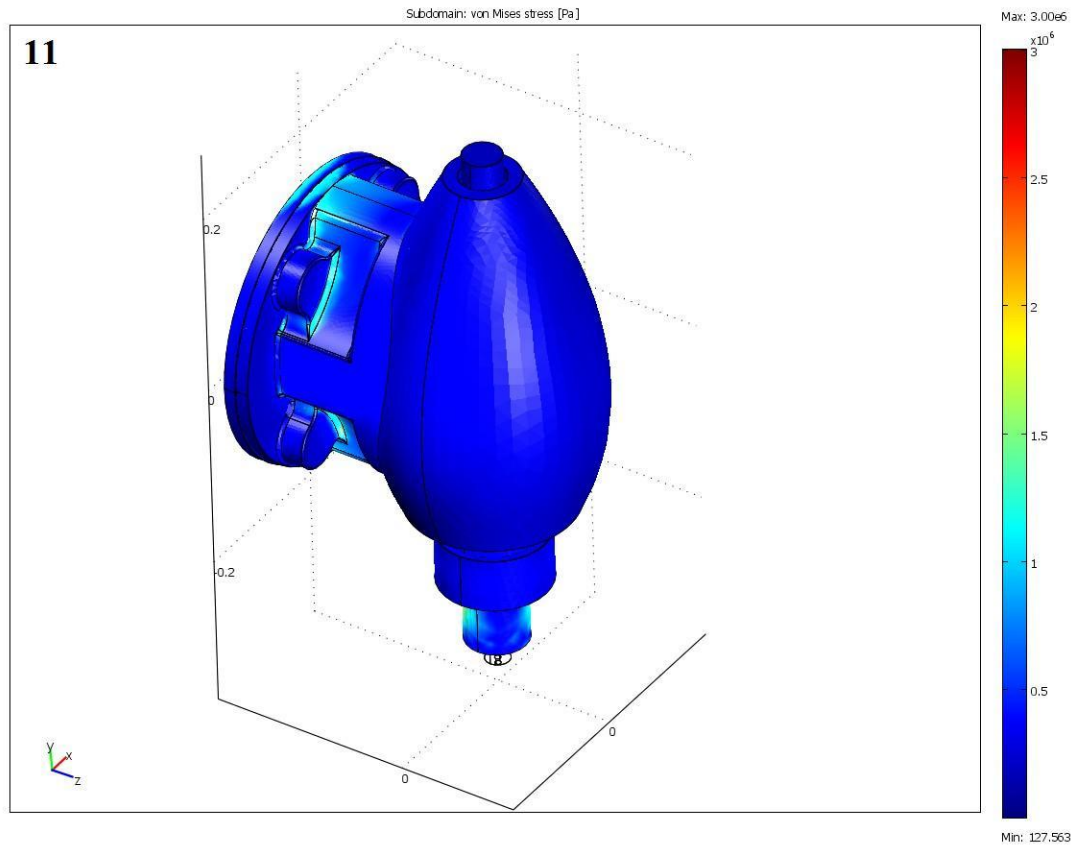
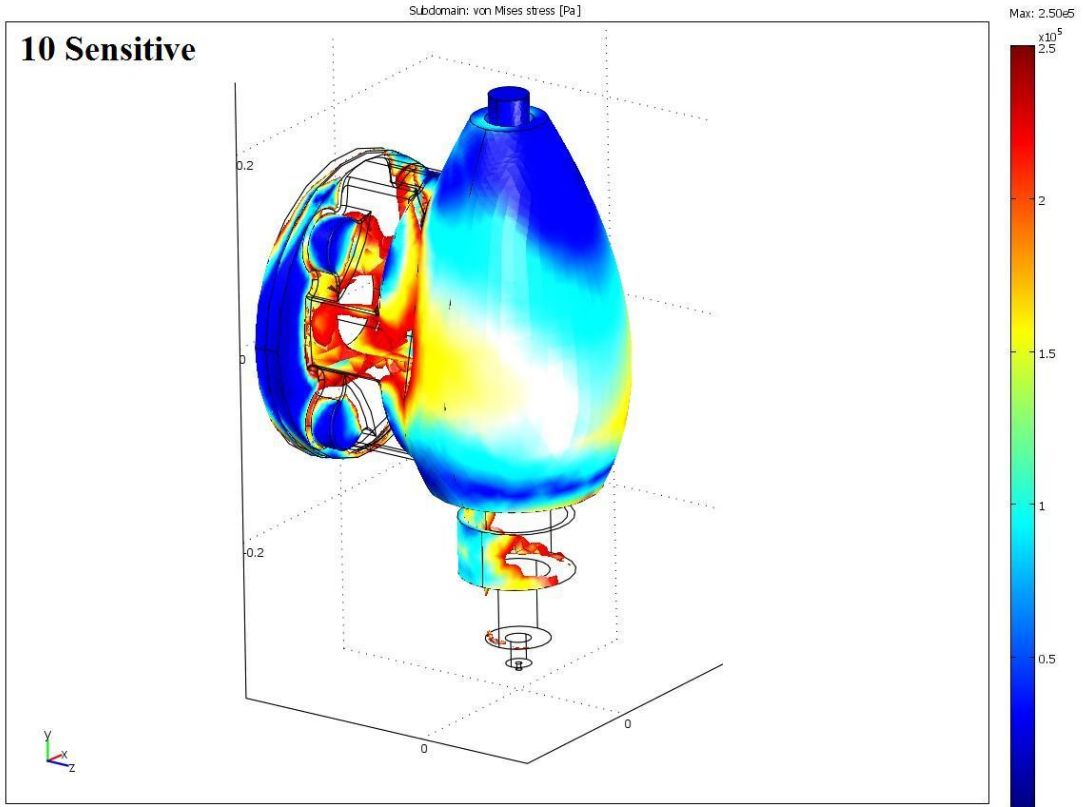


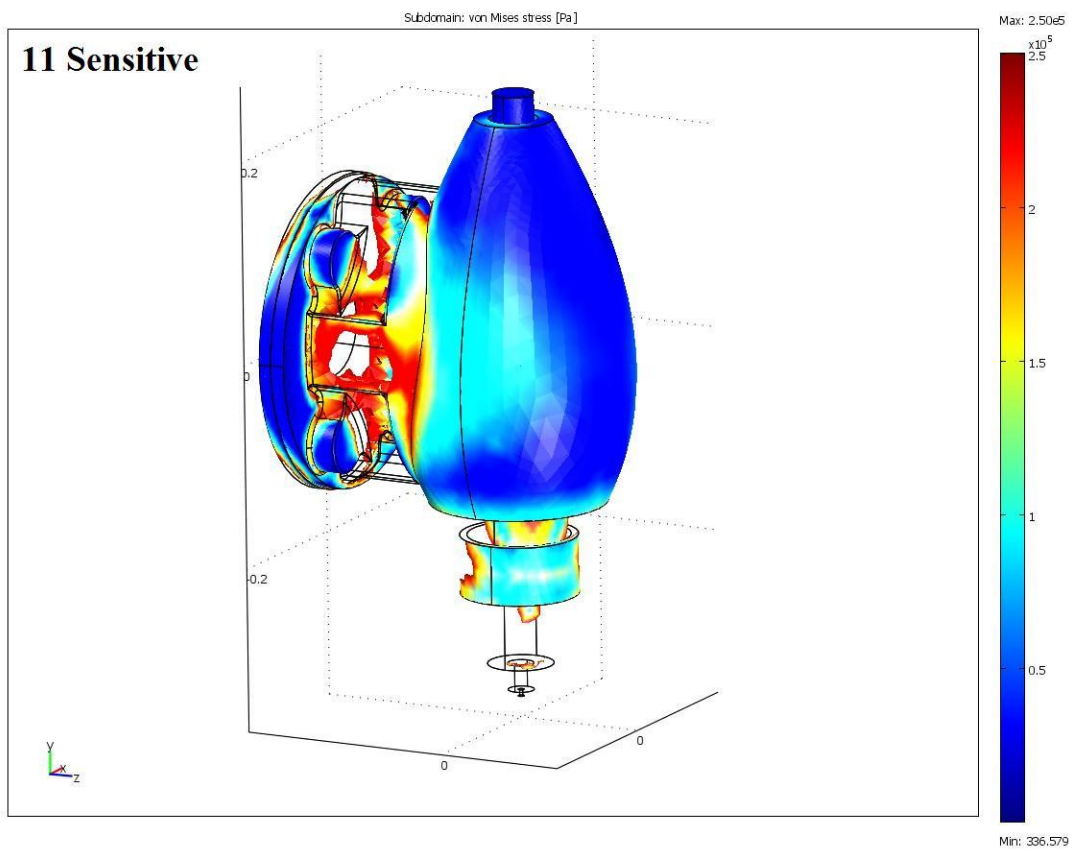
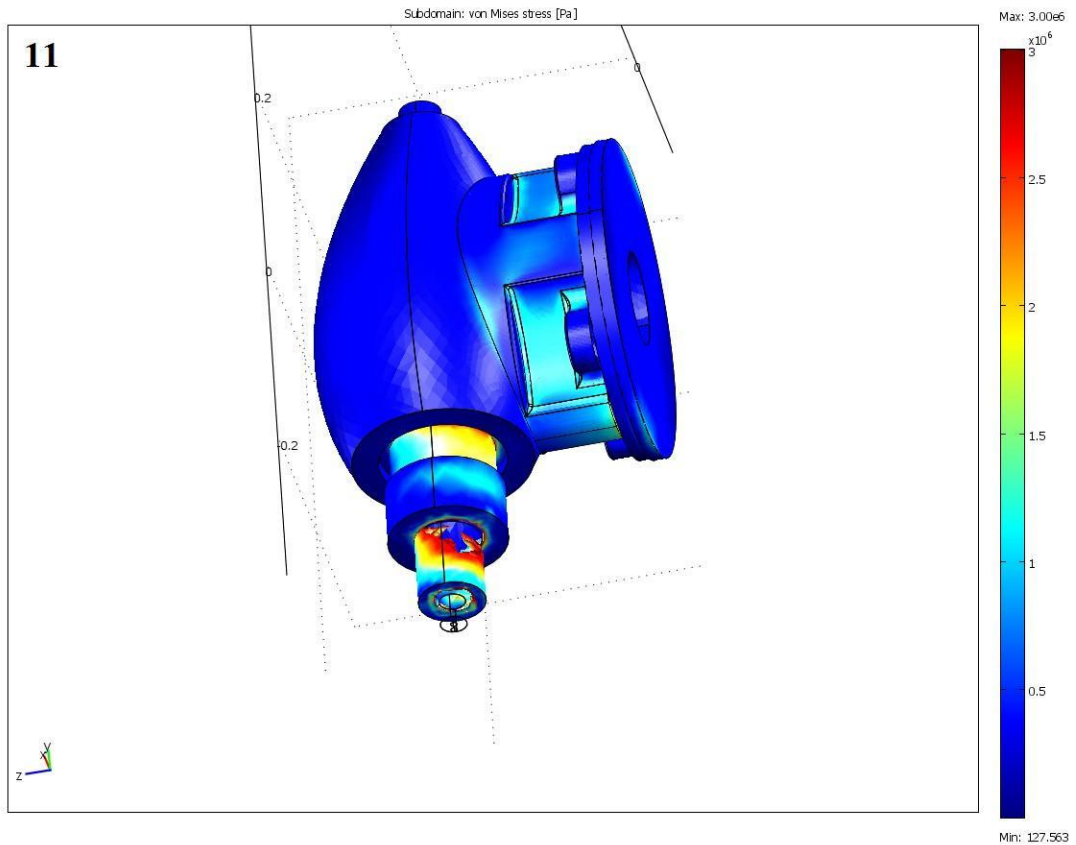








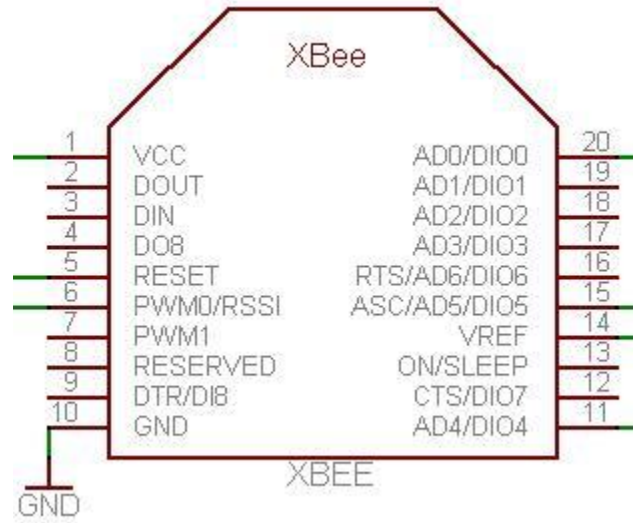




APPENDIX C: XBee Data Sheet

Platform	XBee® 802.15.4 (Series 1)	XBee-PRO® 802.15.4 (Series 1)
Performance		
RF Data Rate	250 kbps	250 kbps
Indoor/Urban Range	100 ft (30 m)	300 ft (100 m)
Outdoor/RF Line-of-Sight Range	300 ft (100 m)	1 mi (1.6 km)
Transmit Power	1 mW (+0 dBm)	60 mW (+18 dBm)*
Receiver Sensitivity (1% PER)	-92 dBm	-100 dBm
Features		
Serial Data Interface	3.3V CMOS UART	3.3V CMOS UART
Configuration Method	API or AT Commands, local or over-the-air	API or AT Commands, local or over-the-air
Frequency Band	2.4 GHz	2.4 GHz
Interference Immunity	DSSS (Direct Sequence Spread Spectrum)	DSSS (Direct Sequence Spread Spectrum)
Serial Data Rate	1200 bps - 250 kbps	1200 bps - 250 kbps
ADC Inputs	(6) 10-bit ADC inputs	(6) 10-bit ADC inputs
Digital I/O	8	8
Antenna Options	Chip, Wire Whip, U.FL, & RPSMA	Chip, Wire Whip, U.FL, & RPSMA
Networking & Security		
Encryption	128-bit AES	128-bit AES
Reliable Packet Delivery	Retries/Acknowledgments	Retries/Acknowledgments
IDs and Channels	PAN ID, 64-bit IEEE MAC, 16 Channels	PAN ID, 64-bit IEEE MAC, 12 Channels
Power Requirements		
Supply Voltage	2.8 - 3.4VDC	2.8 - 3.4VDC
Transmit Current	45 mA @ 3.3VDC	215 mA @ 3.3VDC
Receive Current	50 mA @ 3.3VDC	55 mA @ 3.3VDC
Power-Down Current	<10 uA @ 25° C	<10 uA @ 25° C
Regulatory Approvals		
FCC (USA)	OUR-XBEE	OUR-XBEEPRO
IC (Canada)	4214A-XBEE	4214A-XBEEPRO
ETSI (Europe)	Yes	Yes* Max TX 10 mW
C-TICK Australia	Yes	Yes
Telec (Japan)	Yes	Yes*

APPENDIX D: XBee Pin Diagram



**Source: Adafruit Industries via ladyada.net*

APPENDIX E: XBee Communication Code

```
#!/usr/bin/env python
import serial, time, datetime, sys
from xbee import xbee
import twitter
import sensorhistory

LOGFILENAME = "check.csv"
SERIALPORT = "/dev/cu.usbserial-0000201A" # the com/serial port the XBee is
connected to
BAUDRATE = 9600 # the baud rate we talk to the xbee
VOLTSENSE = 0 # which XBee ADC has mains voltage data

# open up the FTDI serial port to get data transmitted to xbee
ser = serial.Serial(SERIALPORT, BAUDRATE)
ser.open()

logfile = None
try:
    logfile = open(LOGFILENAME, 'r+')
except IOError:
    # didn't exist yet
    logfile = open(LOGFILENAME, 'w+')
    logfile.write("#Date, time, actual_voltage, raw_signal");
    logfile.flush()

# the 'main loop' runs once a second or so
def update_graph(idleevent):

    # grab one packet from the xbee, or timeout
    packet = xbee.find_packet(ser)
    if not packet:
        return # we timedout

    xb = xbee(packet) # parse the packet

    # we'll only store n-1 samples
    voltagedata = [-1] * (len(xb.analog_samples) - 1)
    #This was REMOVED#ampdata = [-1] * (len(xb.analog_samples ) - 1)
```

```

# grab 1 thru n of the ADC readings, referencing the ADC constants
# and store them in nice little arrays
for i in range(len(voltagedata)):
    voltagedata[i] = xb.analog_samples[i+1][VOLTSENSE]

sum_v = 0

for j in range(len(voltagedata)):
    sum_v = sum_v + voltagedata[j]

avg_v_2 = sum_v / len(voltagedata)
actualvoltage = avg_v_2 / 311.94539

#print "AVG (V): ", avgv
print "AVG signal: ", avg_v_2
print "Actual Voltage (V):", actualvoltage

if logfile:
    logfile.seek(0, 2) # 2 == SEEK_END. ie, go to the end of the file
    logfile.write(time.strftime("%Y %m %d, %M:%S")+", "+
                  str(actualvoltage)+", "+
                  str(avg_v_2)+"\n")
    logfile.flush()

while True:
    update_graph(None)

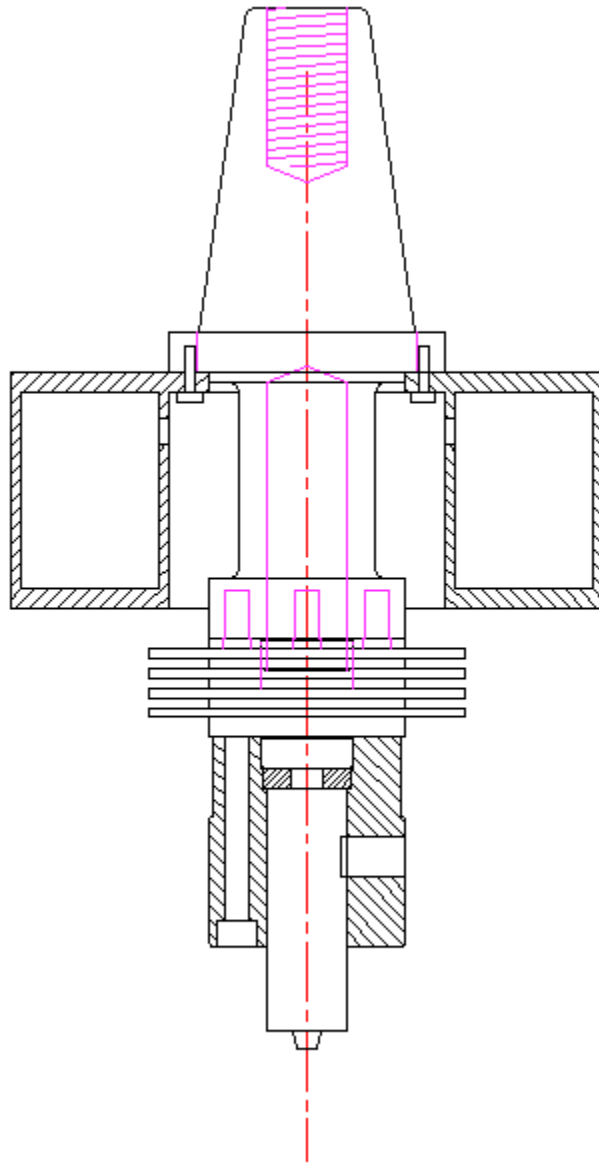
```

APPENDIX F: Elastic Member Strength Calculations

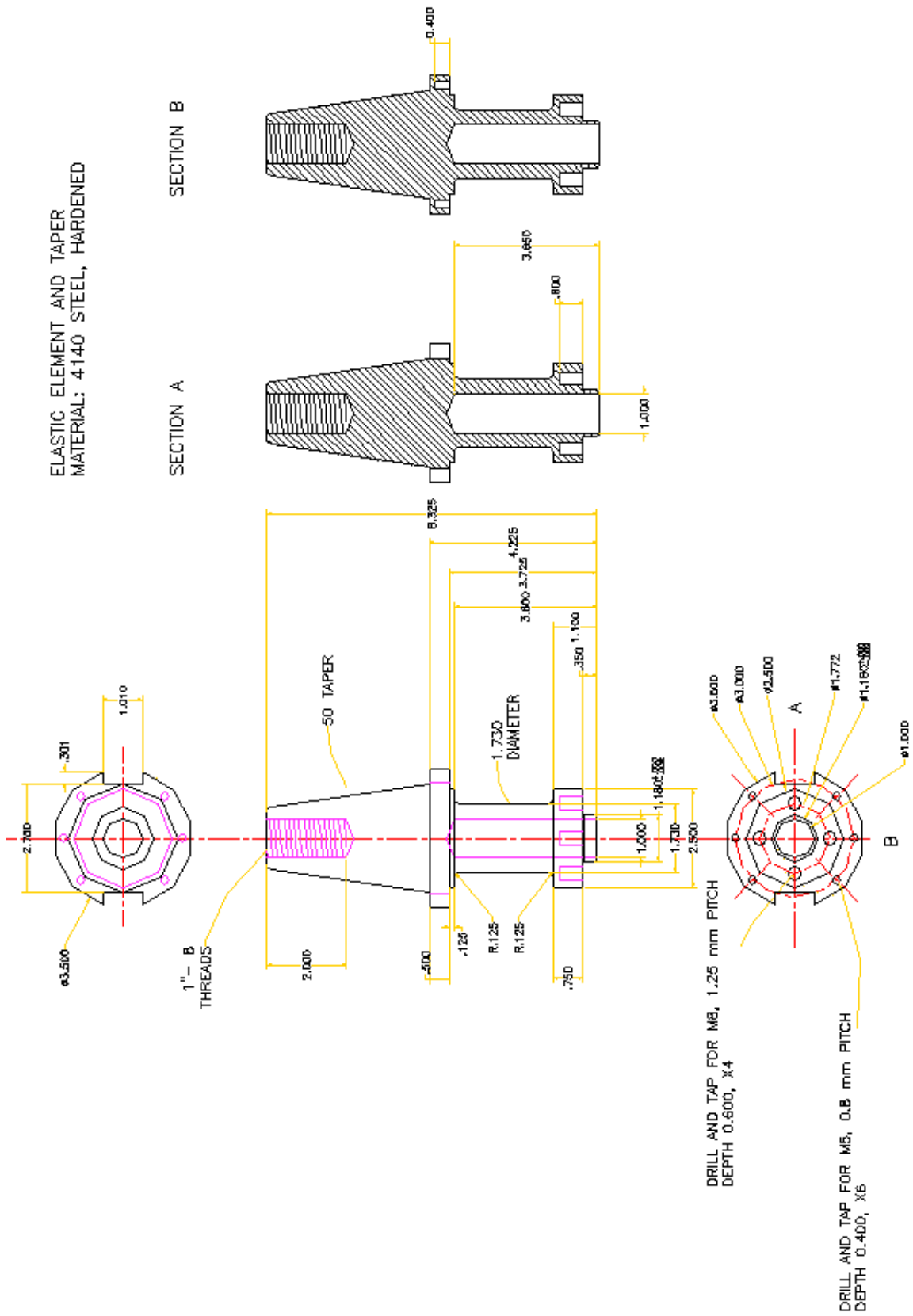
Loads					Material				
Axial Force, Fz	75000	N			Young's Modulus, E	205	GPa		
Torque, T	250	N-m	250000	N-mm	Yield Strength	1510	MPa		
Traversing Force, Fx	7500	N			Shear Yield Strength	755	MPa		
Side Force, Fy	7500	N							
Fxy Resultant	10606.60172	N							
Solid Member					Hollow Member				
Moment Distance, D	209	mm	0.209	m	Moment Distance, D	209	mm	0.209	m
Elastic Member Length, L	63.5	mm			Elastic Member Length, L	63.5	mm		
Diameter, d	41.41	mm	0.04141	m	Outer Diameter, Do	43.942	mm	0.043942	m
Area, A	1346.791424	mm ²			Inner Diameter, Di	25.4	mm	0.0254	m
					Resulting Wall Thickness, t	9.271	mm	0.009271	m
					Area, A	1009.817335	mm ²		
Bending Moment, M	2216779.759	N-mm			Bending Moment, M	2216779.759	N-mm		
C	20.705	mm			C	21.971	mm		
Moment of Inertia, I	144341.3692	mm ⁴			Moment of Inertia, I	162584.3376	mm ⁴		
Polar Moment of Inertia, Ip	288682.7385	mm ⁴			Polar Moment of Inertia, Ip	325168.6752	mm ⁴		
Normal Compressive Stress	55.68791028	MPa			Normal Compressive Stress	74.2708581	MPa		
Bending Stress	317.9852398	MPa			Bending Stress	299.5667897	MPa		
Max Compressive Stress	373.6731501	MPa			Max Compressive Stress	373.8376478	MPa		
Shear Stress	17.93058368	MPa			Shear Stress	16.89200227	MPa		
Principle Stresses					Principle Stresses				
Sigma 1	374.5315713	MPa			Sigma 1	374.5993676	MPa		
Sigma 2	0	MPa			Sigma 2	0	MPa		
Sigma 3	-0.858421174	MPa			Sigma 3	-0.761719761	MPa		
Max Shear	187.6949962	MPa			Max Shear	187.6805437	MPa		
SF Determination					SF Determination				
Von Mises LHS	281192.2812				Von Mises LHS	281221.2123			
Von Mises RHS	4560200				Von Mises RHS	4560200			
Von Mises Factor of Safety	4.027				Von Mises Factor of Safety	4.027			
Tresca Factor of Safety	4.022				Tresca Factor of Safety	4.023			

Sensor Output					Sensor Output				
Compressive Strain	271.6483428	micro-mm/mm			Compressive Strain	362.2968688	micro-mm/mm		
Shear Strain	87.46626187	micro-mm/mm			Shear Strain	82.40001107	micro-mm/mm		
Bending Strain	1551.147511	micro-mm/mm			Bending Strain	1461.301413	micro-mm/mm		
Compressive GF	2.18				Compressive GF	2.18			
Shear GF	2.18				Shear GF	2.18			
Bending GF	2.18				Bending GF	2.18			
Compressive Sensitivity	0.124609332	mV/V			Compressive Sensitivity	0.166191224	mV/V		
Shear Sensitivity	0.040122138	mV/V			Shear Sensitivity	0.03779817	mV/V		
Bending Sensitivity	0.711535556	mV/V			Bending Sensitivity	0.670321749	mV/V		
Deflection					Deflection				
Equivalent Force, F	34909.91746	N			Equivalent Force, F	34909.91746	N		
Theta	0.002378601	rad	0.136	deg	Theta	0.002111707	rad	0.121	deg
Ymax	0.100694109	mm			Ymax	0.089395607	mm		
Deflection from Angle	0.346086118	mm			Deflection from Angle	0.307253176	mm		
Total Lateral at Shoulder	0.447	mm			Total Lateral at Shoulder	0.397	mm		
*Moment Distance is from location of forces (shoulder) to top of elastic member. This ensures the maximum bending stress is represented in the calculations.									

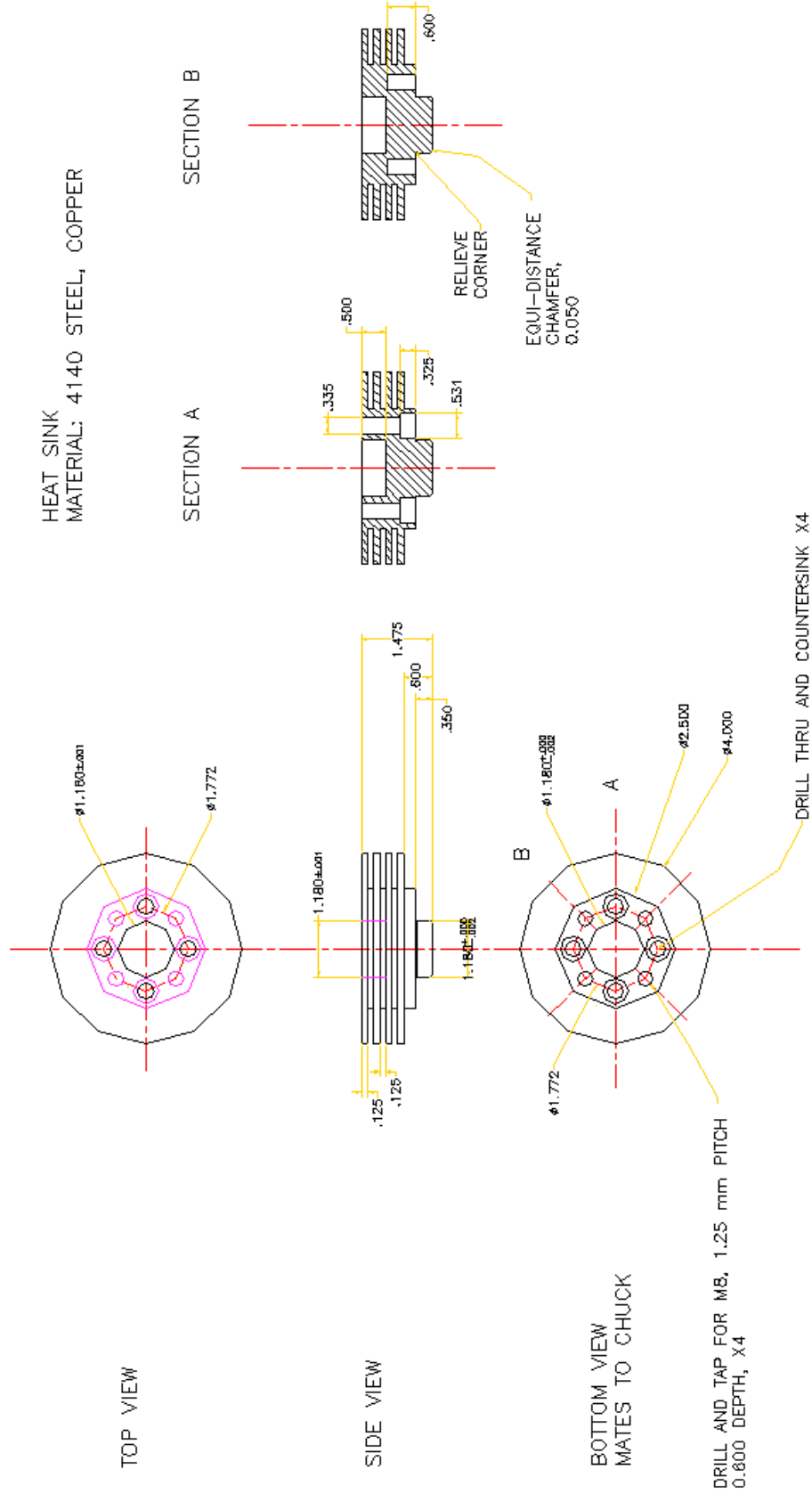
APPENDIX G: Force Transducer Design Drawings



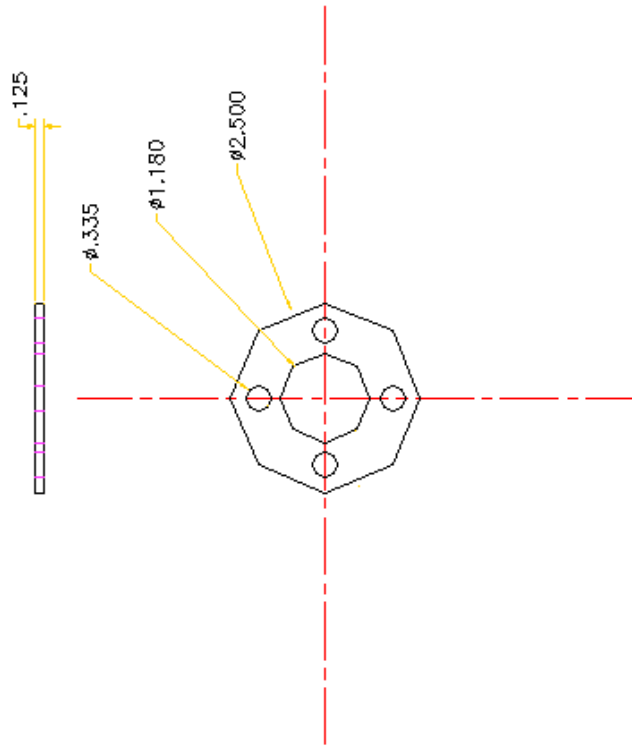
ELASTIC ELEMENT AND TAPER
 MATERIAL: 4140 STEEL, HARDENED



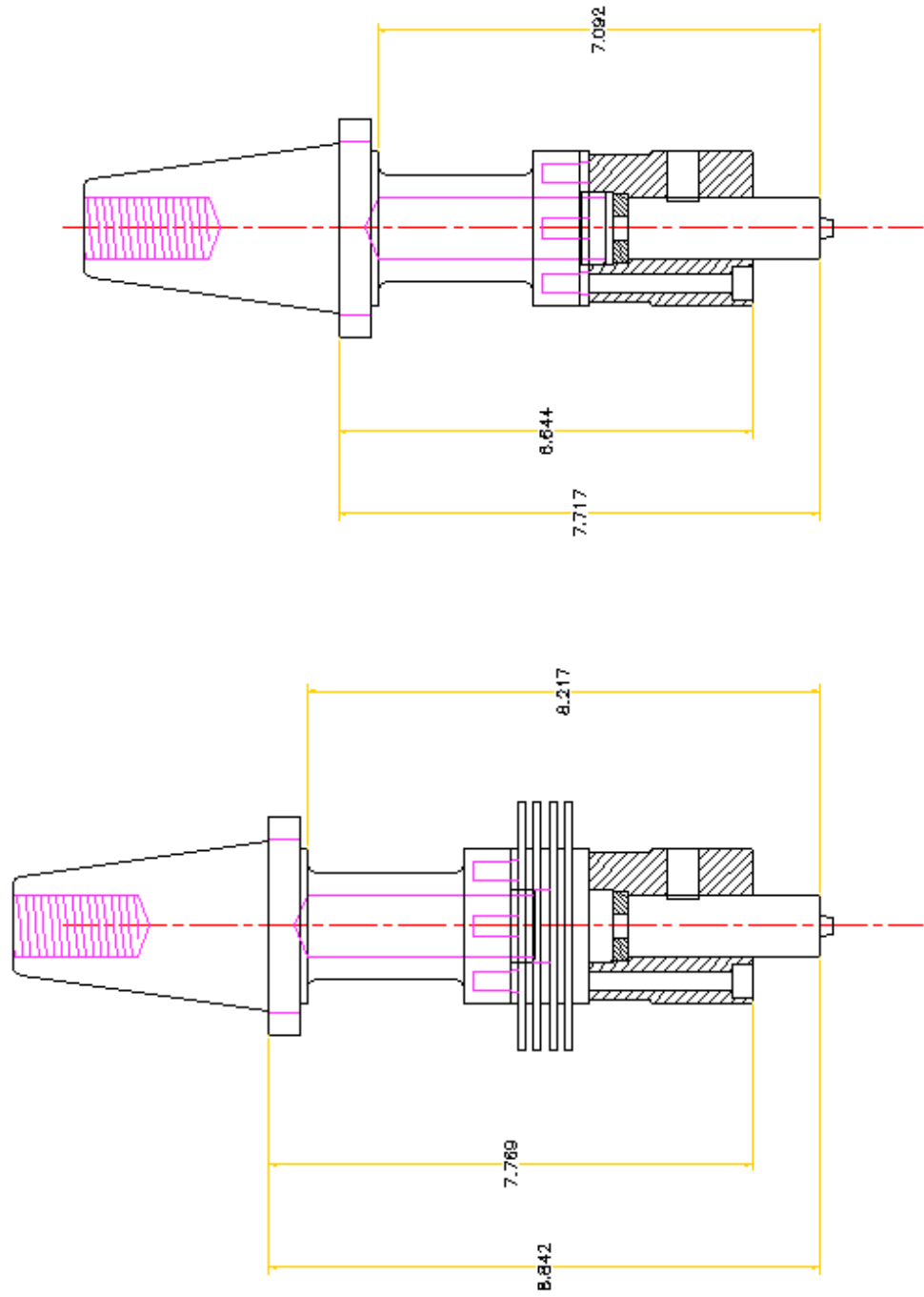
HEAT SINK
 MATERIAL: 4140 STEEL, COPPER



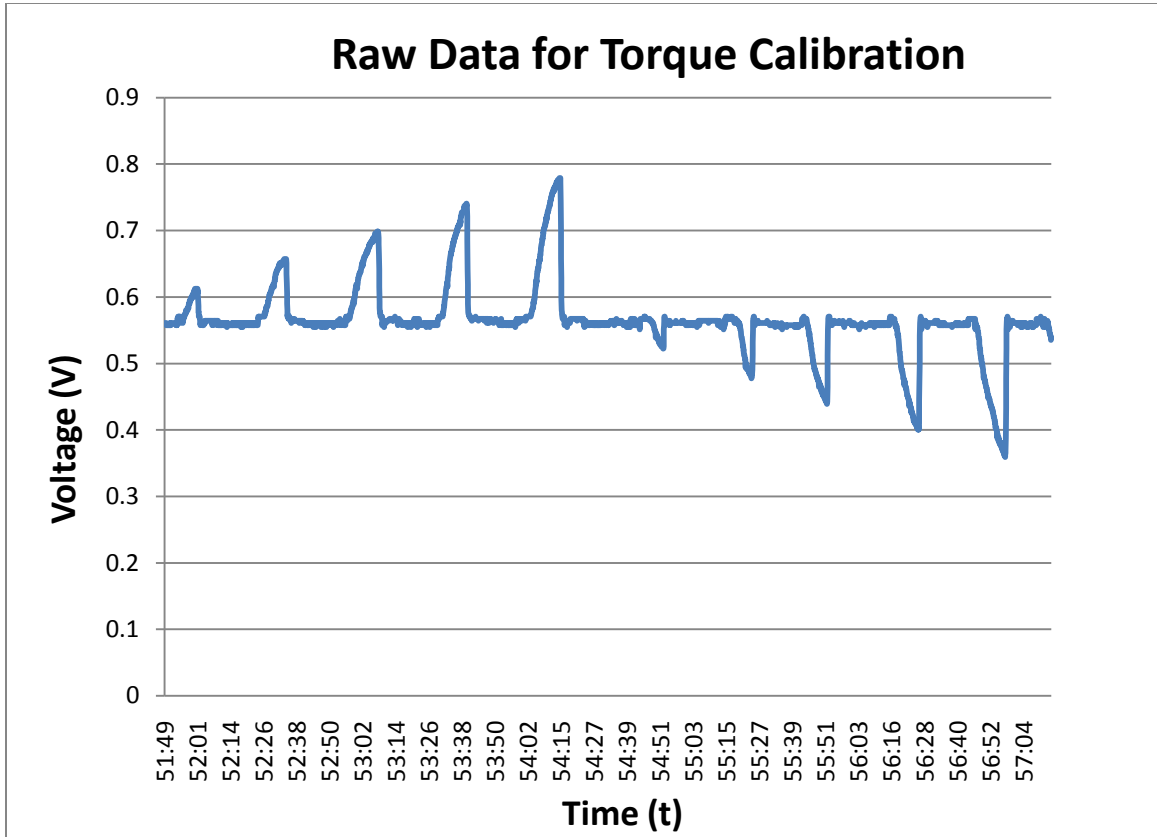
THERMAL BARRIER
MATERIAL: G7 GLASS-SILICONE, 345 MPa CYS, 220 C MELTING TEMP
MCMASTER:



ASSEMBLY
REQUIRES 4 M8, 1.25 mm PITCH BOLTS, 35 mm THREADED LENGTH
MCMASTER: 91290A438



APPENDIX H: Torque Calibration Data



Load, Nm	Voltage
-25.16	0.359037
-19.89	0.400711
-15.48	0.439179
-10.11	0.484059
-5.35	0.522527
5.03	0.612287
10.17	0.657166
14.97	0.69884
19.87	0.740514
24.73	0.778983